TWO DIMENSIONAL ANALYSIS OF

INCOMPLETE PARAMETERISED ARCHIVAL DATA

FROM THE WHIPPLE 10 METRE IMAGING ATMOSPHERIC CHERENKOV TELESCOPE

CENTERED ON AE AQUARII

by

Michael Connolly H.Dip., B.D., B.Ph., B.Sc.

A dissertation submitted to the

Centre for Astronomy, School of Physics,

National University of Ireland, Galway

in fulfilment of the requirements for the

degree of Master of Science

Supervisor

Dr Mark Lang

February 2010

Galway, Ireland

Dedicated to the memory of

Martin Connolly (1940-1985)

Hard work and belief can accomplish,

With God's help

Contents

Chapter 3:

The Imaging Atmospheric Cherenkov Technique

LIST OF ILLUSTRATIONS AND GRAPHS

LIST OF TABLES

Acknowledgements

I would like to thank my supervisor Mark Lang for the constant encouragement and dedication shown to me; it has been an example in helpfulness that I can only hope to emulate myself. This work would not have reached completion without his experience and generosity and I will always be grateful to him for that. Additionally the Centre for Astronomy of the National University of Ireland, Galway, deserve special mention for their willingness to welcome a mature student who returned to the study of Astronomy after almost 20 years absence. Gary Gilanders, Gary Kenny, Tess Mahoney and all staff and fellow post-graduate students were most helpful when I often disturbed their own work. I hope I did not annoy too many during the course of this thesis.

I have heard it said, by many scientists among others, that we can see so far towards the horizon of understanding the cosmos because we stand on the shoulders of giants. This I do not doubt. Yet who put me on those big shoulders? I want to thank most sincerely my own family and in particular my mother, Rita, who has dedicated her life to her children, I being the oldest. From my earliest years I was formed in the school of hard work and integrity in all things; this has born great fruit in all areas of my life. Above all I remember my father, Martin, who died 25 years ago this year, a life cut short at 44 years by Leukaemia. I will always remember your dedication shown to your work and your lessons in leadership. They have left an indelible make on me.

I re-discovered my hunger for truth and understanding thanks in no small part to the former bishop of Galway, +James McLoughlin (rip). For some mysterious reason he sent me to study in the Gregorian University, Rome, through Italian. After completing bachelors degrees in both Philosophy and Theology I knew I could never return to my former intellectual laziness. Special mention I pay to Fr Martin Downey pp., for his encouragement and willingness to allow me some space to study in a busy pastoral situation.

I only hope I can give as generously as I have received.

ABSTRACT

I report on an original analysis made in the TeV energy band of an area of sky extending 2^o x 2^o centred on the cataclysmic binary variable Ae Aquarii using parameterised archival data taken from the Whipple 10m Imaging Atmospheric Cherenkov Telescope during the 1991-1992 observational epoch. During this epoch, only the Centre of Field of View was examined for putative gamma-ray sources. The instrument and observational techniques are not modified but the data is subjected to a 2 dimensional analysis, where individual 'bins' of sky area 0.1^o x 0.1^o are examined incrementally for possible point source gamma-ray emitters. The subsequent analysis is validated by another archival data set from the standard candle for gamma-ray astronomy, the Crab Nebula, which has been offset from the Centre of Field of View by 1^o.

The results of the analysis did not yield any TeV gamma-ray point source from data set in question, though the validation run has proven this methods ability to examine incomplete parameterised data.

Chapter 1

Introduction

1.1: Introduction to thesis

Very High Energy (VHE) gamma radiation may be detected from astrophysical sources using atmospheric Cherenkov telescopes. This is due to the VHE photons ability to interact with the upper atmosphere to produce detectable amounts of visible to ultraviolet light. This light, called Cherenkov light, is caused by VHE photons creating an optical shockwave by pair production. This clever technique which rejects unwanted Cherenkov light from other sources allows observations by ground based telescopes. In the 1990's the technique was used to search for TeV emissions from single points in the sky, although the telescope typically had a wide field of view of $\approx 3.5^{o}$. Currently sky maps of the entire field of view are obtained from instruments such as VERITAS (Weekes et al., 2002). TeV2032 is given as an example of a source detected in the field of view of reanalysed archival data; refer to Fig 1.1. This thesis is based on a wide angle technique called 2 dimensional analysis. It is a wide angle analysis of incomplete parameterised (i.e. partly processed) archival data, where the original Cherenkov light received at the telescope was not recorded in full but in a more condensed form.

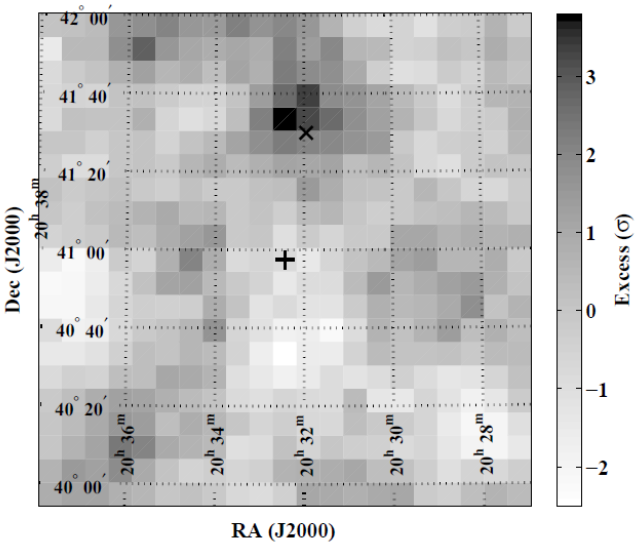

Fig 1.1: TeV Sky map of the Cygnus X-3 region of sky showing the peak in significance at darker position (marked with an x) of TeV J2032+4130. Cygnus is at the centre of the sky map and is marked with a +. Taken from Lang et al. (2004)

The genesis of the idea for this thesis came from (Lang et al. 2004). Reports were made of TeV emissions in the same sky region as a well known X-ray source, Cygnus X-3, as is seen in Fig 1.1. On reexamining some archival data centered on Cygnus X-3 using 2 dimensional analysis evidence of an apparently steady source of TeV emissions was reported at the approximate location reported by some other Imaging Atmospheric Cherenkov Telescope's (Lang et al., 2004). Note here that there is no indication of an excess of events from the centre of the field of view, *i.e.*, the position of Cygnus X-3.

The instrument used to observe the gamma ray object from the surface of the Earth was the 10m Whipple Imaging Atmospheric Cherenkov Telescope at Mt. Hopkins, Arizona during the period of the early 1990's.

The 2 dimensional analysis technique showed itself capable of detecting putative sources offaxis, i.e. not at the centre of field of view. Central to this present analysis of archival data is software tailored to the parameter files under question, which were incomplete. AE Aquarii, a cataclysmic variable binary star system, was observed from 1991-1995 and all that remains are the parameters thought at the time to be the most useful to keep for future analysis. The missing information had to be calculated and estimated which is what made the work undertaken original. Remembering that the archival period under question was before the large scale availability of cheap computer memory, it was the time of the intel 386x and associated architecture, most observations examined the centre of field alone. Unlike most software development for Whipple, the Microsoft windows environment was chosen above Linux for personal reasons alone.

1.2: Thesis overview

The objective of the research carried out in the present thesis is reexamination of archival data from the Whipple telescope centred on AE Aquarii and taken in the 1990-1991 and 1991-1992 observation seasons. This data was stored parameterised with the loss of the original raw data direct from the 109 PMT's which constituted the camera. This already incomplete parameterised data was what made this analysis original in that

critical parameters had to be approximated by calculation and then the 2 dimensional analysis could be undertaken.

Though the archival data is centred on this well documented binary system, it is not the principle objects of concern. The archive data was subjected to the above mentioned 2 dimensional analysis covering an area of sky 2^o by 2^o in a search for further gamma ray sources whose Cherenkov 'fingerprint' may have been captured by the Whipple Imaging Atmospheric Cherenkov Telescope during the observing seasons mentioned above. At the time of the original observations these non thermal VHE sources were thought to be so rare with respect to the predominant thermal universe that no thought was given to offaxis searches.

Of principal importance was the validation criterion specifically developed for this analysis. Use was made of archival data from the Crab Nebula contemporaneous with the archival data under examination which had the source offset from the centre of field of view by 1^o. As the Whipple's telescope mounting meant that the field of view could not be derotated during observation mathematical derotation had to be carried out. The Crab offset data was to ensure derotation of image centroids was properly carried out using parallactic correction, i.e. mathematical derotation. The results are presented in chapter 4.

1.3: Personal contribution

As no suitable software existed for the particular 2 dimensional analysis under question it was the principle task of this thesis to write the code in C++. This would read the data and subject it to the required process that would unveil any overlooked VHE gamma ray source offset from the centre of field of view. Such software has to be validated and this was made possible by the archival data of the Crab nebula mentioned above. As only 5 ½ hrs of offset Crab observations was retrievable from the digital audio tape on which it was recorded the image intensity of the point source measured with respect to the background (known as the Statistical Significance, measured in standard deviations (N_σ)) was weak. It was considerably weaker than that present in the Crab centre of field of

view data set comprising of 38 pairs of observations of 28 minute duration each which was also examined in this present thesis. Provided the Crab point source offset 1^{o} yielded a statistical significance > 5 standard deviations (5σ) we would be able to confidently continue with the validation. Smaller values of standard deviation may in fact be due to naturally occurring fluctuations in the ever present gamma ray background radiation. Statistically we can expect to see a statistical significance ≈ 3σ in one to two points on our 2 dimensional Cartesian grid. This will be explained in much greater detail in chapter 3 and chapter 4.

The archival data set from AE Aquarii subjected to 2 dimensional analysis consisting of approximately 29 hrs of observation or 14.5 hrs onaxis (refer to Table 4.4), has never been subjected to a 2 dimensional analysis before. Should this process prove successful it may make possible the further analysis of other archival data from the Whipple Imaging Atmospheric Cherenkov Telescope. This history is mentioned briefly in chapter 3. This would entail transferring the existing archival data onto a HDD and converting the data into ASCII so simple text editors may be used to hold the data. It would then have to be verified as accurate by reconstructing the original preliminary results for the centre of field of view. That is possibly the future. The present analysis would suffice to unveil any TeV sources hidden in the digital mass of data from the archival set.

The present thesis will it is hoped add a further avenue of exploration to the VERITAS Collaboration. This is to reexamine archival data from the most consistently sensitive Imaging Atmospheric Cherenkov Telescope to date. The programming language will ensure that code segments will be integratable with the wider collaboration and code already tried and tested by the Collaboration could in future be incorporated into this archival examination should this be deemed feasible. As telescope time becomes ever more in demand, an archival search may produce more likely candidates to focus the telescopes attention on.

Chapter 2

Very High Energy Gamma Ray Astronomy

2.1: Introduction

The gamma ray spectrum covers an energy range from 1Mev to > 100TeV. This range is loosely sub divided into 5 energy bands whose demarcation is governed by the detection methods used for the energy range. The following table (2.1) displays these 5 ranges in order of increasing energy; it should be noted that the energy ranges overlap.

Energy Band	Energy Range	Detection Technique	
LOW	0.1 MeV – 10 MeV	Scintillator	Satellite
MEDIUM	1.0 Mev – 30 MeV	Compton Telescope	Satellite
HIGH	30 MeV – 10 GeV	Spark Chamber	Satellite
VERY HIGH	10 GeV – 100 TeV	Atmospheric Cherenkov	Ground
ULTRA HIGH	> 100 TeV	Air Shower Array	Ground

Table 2.1: Gamma ray Astronomy bands.

When the energies of the incoming photons are between 1 MeV and < 30 GeV, we are not able to detect them with ground based telescopes as the energies are too small to initiate the required sequence of interactions with the atmosphere which in turn produce detectable visible to ultraviolet light pulses. The upper limit is presently challenged (Merck et al., 2003). Detection of these medium to high energy photons is achieved by space based telescopes, refer to Fig 2.1 below. When the energies are greater than 100 TeV, ground based air shower arrays detect the resulting particle and photon cascade directly. These two techniques are only mentioned in passing; our main focus is on detection of light emanating from interactions between VHE photons and the atmosphere detectable with specially developed telescopes.

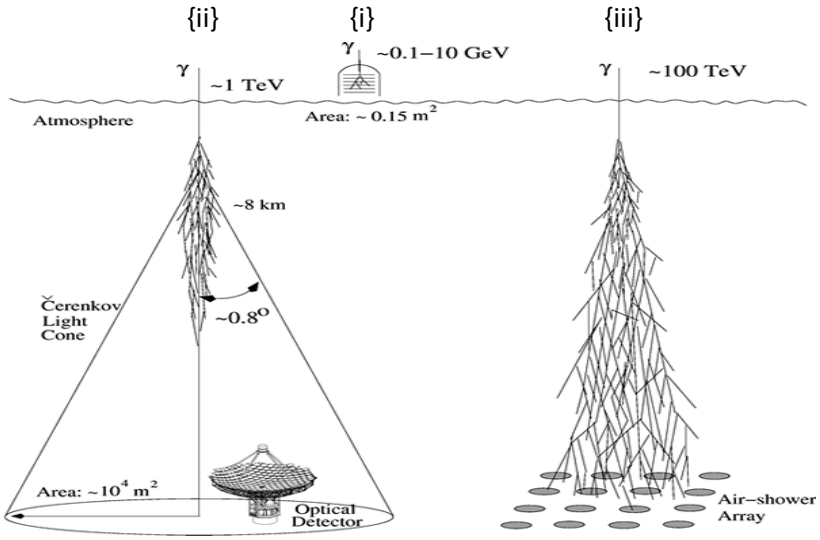

Fig 2.1: Schematic of detection of gamma rays for{i} Eγ < 10 GeV, {ii} 30 GeV < Eγ < 1 TeV,{iii} Eγ > 100 TeV. Adopted from Quinn (1997).

On the arrival of a VHE gamma ray (or cosmic ray with sufficient energy) at the Earth's upper atmosphere, cascades of relativistic electrons and positrons are produced by pair production. These cascades are called Extensive Air Showers. The electrons travel faster than the speed of light in the medium of the atmosphere; as a result a light pulse optically analogous to a 'sonic' boom is produced. This optical shockwave is called Cherenkov light and this light is emitted in the blue to ultraviolet region of the electromagnetic spectrum and though of only 3-5 ns in duration it can be detected by Photomultiplier tubes. The basic elements needed to detect this light are shown in Fig 2.2.

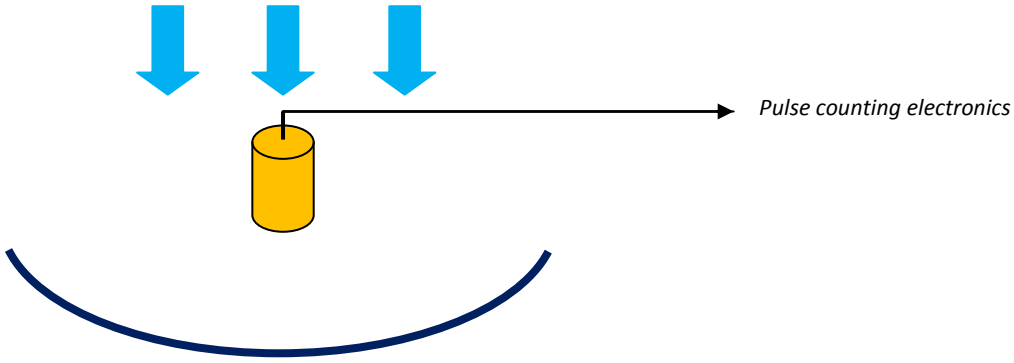

Fig 2.2: The basics elements needed to detect Cherenkov light. The blue arrows are the light incident on a gathering mirror with a PMT at the focus. The resulting signal is sent to fast pulse counting electronics.

The use of VHE gamma rays for observational astronomy has developed greatly during the last 20 years principally this is due to improved techniques used to reject the far greater hadron or cosmic ray background present in the night sky which also initiate extensive air showers. A prominent motivation in the development of this field is an attempt to discover the origin of highly charged cosmic rays which remained a mystery for almost a century. These highly charged particles arrive at the Earth's atmosphere and some at the Earth's surface in a non negligible flux. Their origin is worthy of investigation for cosmic rays contribute to the ambient radiation all people receive. They have an effect on electronics and have a significance to bear in space travel. Additionally they play a role in lightning and it is believed that they play a role in climate change too. The VHE gamma rays from M82 observed from 2007-2009 by the successor of Whipple, the VERITAS telescopes, may indeed carry the required information needed to unlock this longstanding mystery (Acciari et al., 2009).

Cosmic gamma rays (not cosmic rays or particles per se) have overall three characteristics that make them most informative about non thermal relativistic processes. Firstly their production en mass in many galactic and extragalactic settings. The effective acceleration of charged particles and their subsequent interaction with the ambient gas, low frequency radiation, and magnetic fields implies the possibility that the internal processes may reveal themselves by the photons emitted. Secondly free propagation of the photons in space without deflection in the interstellar and intergalactic magnetic fields means the source position can accurately be determined (however there is a question of infrared absorption). Finally there is an effective and evolving detection by space borne and/or ground based instruments (Aharonian and Akerlof, 1997).

These photons are thus probes and also messengers of a side of our universe that we are only now growing in understanding of. Having just celebrated the 400th anniversary of the invention of the telescope by Galileo Galilei, let us remember the title of his seminal work, "The Starry Messenger". Perhaps these innocuous photons are messengers speaking a language that we may now, perhaps, be able to translate.

2.2: Gamma ray production in the Earth's atmosphere

Gamma rays may be produced when charged particles such as electrons are accelerated by deflection from another charged particle or particles, usually an atomic nucleus.

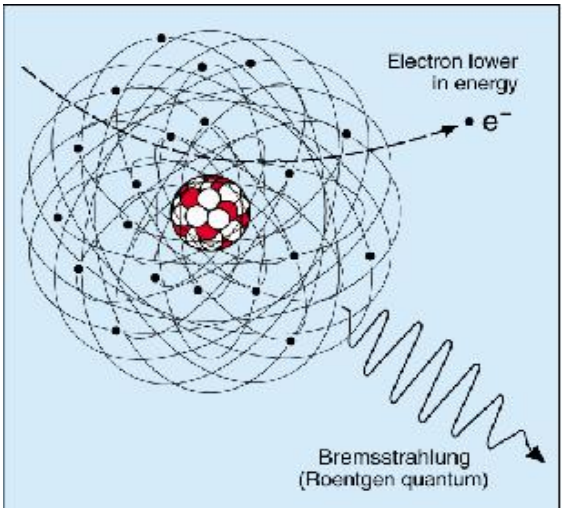

Fig 2.3: Production of *Bremsstrahlung*, courtesy of European Nuclear Society.

As we can see in Fig 2.3 when an electron or positron (indicated by a dotted line) is deflected by an atomic nucleus it emits a single photon (represented by a waveform line). *Bremsstrahlung*, the braking radiation produced when a charged particle is deflected by an atomic nucleus, has a continuous spectrum. This phenomenon was discovered by Nikola Tesla during high frequency research he conducted between 1888 and 1897 and may also be referred to as free-free radiation. This is the radiation that arises as a result of a charged particle that is free both before and after the deflection (acceleration) that causes the emission.

2.3: Extensive Air Showers

Before the telescopes used to observe gamma rays from the ground are explained and their historical development looked at time needs to be given to understanding the production of Cherenkov light from the incident particles and photons. Firstly consideration is given to the production of charged particles from the incoming photon then how these charged particles produce the light in question.

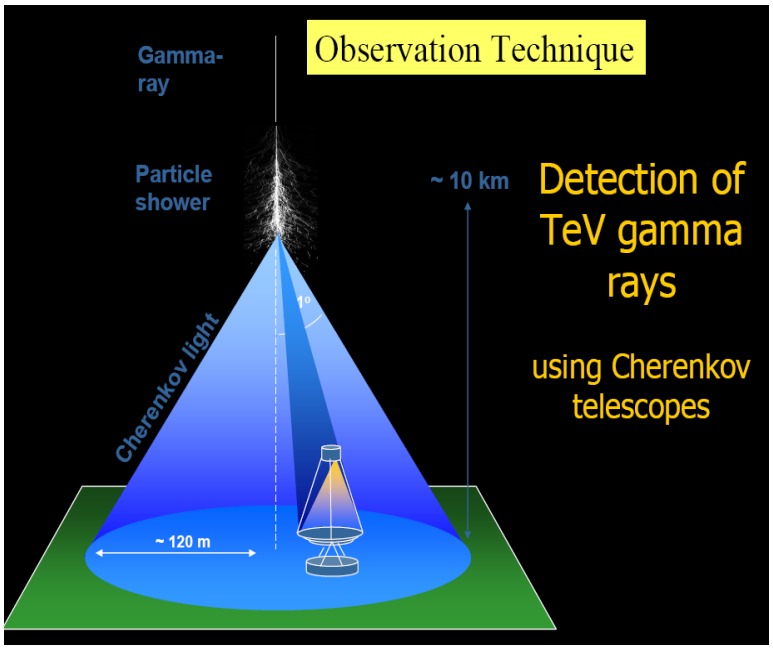

Fig 2.4: Illustration of extensive air shower, adopted from Martinez.

2.3.1: Pair Production

Pair production refers to the creation of an elementary particle and its antiparticle, usually from a photon (or another neutral boson). This is allowed provided there is enough energy available to create the pair (at least the total rest mass energy of the two particles) and that the situation allows both energy and momentum to be conserved. All other conserved quantum numbers (angular momentum, electric charge, etc.) of the produced particles must sum to zero.

Examining the case of electron-positron pairs, when the energy of the incoming photon has an energy $E_\gamma > 2 \times m_e c^2$ (twice the rest mass energy of the electron = 1.022 MeV) then pair production is possible in the field of the nucleus. Although this is the threshold energy the cross-section available for interaction remains quite small until the energies reach higher ($\approx 10^2$) MeV. Pair production can only take place in the field of the nucleus and not free space for the conservation of energy and momentum require a third mass to absorb some of the energy or momentum (Longair, 2004). If E_γ is much more energetic heavier particles may also be produced. These interactions were first observed in Patrick Blackett's Counter Controlled Bubble Chamber, leading to the 1948 Nobel Prize in Physics. Pair production is bound to occur when there are significant

fluxes of high energy gamma rays. There is evidence for the production of positrons by pair production via the detection of the 511 keV electron-positron annihilation spectral line in our Galaxy.

2.3.2: Electron-photon cascades or electromagnetic showers

Refer to Fig 2.5. A high energy photon entering the atmosphere produces an electron-positron pair. Each in turn generates high energy photons by bremsstrahlung. Each of these generates an electron-positron pair and thus the process continues.

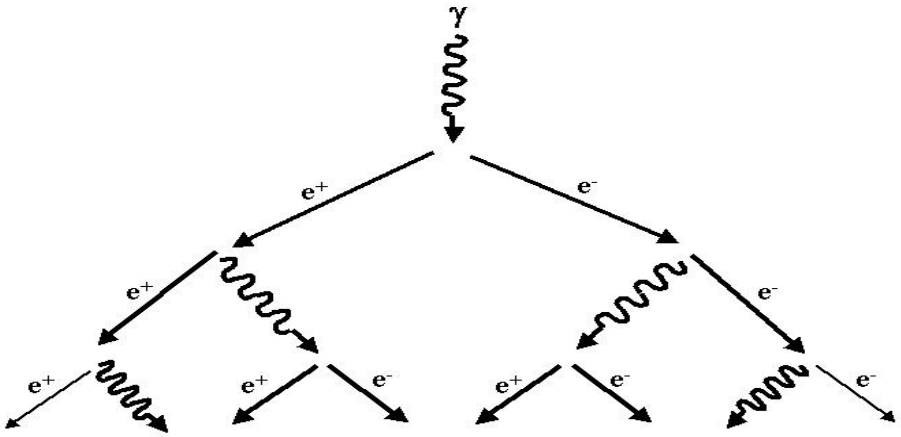

Fig 2.5: A simple schematic of electron-positron pair production initiated by an incoming gamma ray with an energy $E_\gamma > E_c$. secondary gamma rays are produced by bremsstrahlung.

Building a simple model for electron-photon cascades, we note that at ultrarelativistic energies the radiation lengths, R, for pair production and bremsstrahlung are roughly the same. This is demonstrated in Fig 2.5 where the waveform line, γ, represents the radiation length. If a cascade is initiated by a gamma ray of energy E_γ then after a distance of R on average an electron-positron pair is produced, each particle having energy of $E'_\gamma = \frac{E_\gamma}{2}$. In the next radiation length R the electron and positron loose about ½ their energy as they radiate a gamma ray by bremsstrahlung. We now have 2 photons and two particles each with energy $E'_\gamma = \frac{E_\gamma}{4}$, after travelling a distance of 2R. Therefore after a distance of nR the number of electrons, positrons and photons combined is 2^n and their average energy is $E'_\gamma = \frac{E_\gamma}{2^n}$.

The cascade eventually stops when the average energy drops below a critical energy E_c. When $E'_\gamma = E_c$, we have the *shower maximum*. This critical value E_c has been estimated at 83 MeV (Longair, 1992). Below this limit the major losses are due to ionisation in the case of the electrons and not bremsstrahlung. The shower intensity drops off very rapidly as the number of radiation length for subsequent interactions increases; electron-ion pairs are produced in great quantity but are of low energy. Additionally, the cross section for pair production decreases until it is of the same order as that for Compton scattering and photoelectric absorption. When $E_\gamma < 10$ MeV the photons interact with the air particles mainly through Compton Scattering (Gaisser, 1990).

We can thus summarise the following for electron-photon cascades,
(i)The initial growth is exponential (ii) the maximum number of particles is proportional to E_γ , the energy of the original photon (iii) beyond the maximum when the average energy < E_c the electron flux decreases rapidly (iv) it is further important to note that the shower consists only of electrons, positrons and photons (gamma rays) as is seen in Fig 2.5. There are no muons, pions or other particles present making the cascade a 'clean' and hence readily identifiable event that can make it distinguishable from cosmic ray interactions which also produce Cherenkov radiation (Longair, 2004). Refer to Fig 2.6.

2.4: Extensive air showers from two different progenitors

It is essential to point out at this time that extensive air showers are caused by two different initiators; the least common being VHE photons while by far the most common cause of extensive air showers are hadrons. These are principally atomic nuclei.

2.4.1: Properties of gamma ray induced showers

The telescopes developed for this field are particularly suited for gamma ray astronomy for three reasons. Firstly the forward momentum of the shower is large and the Cherenkov angle of emission in the atmosphere is $\approx 1^o$ so that the Cherenkov light retains the original direction of the primary photon. Thus the angular resolution inherent in the technique is high. Secondly the light from the extensive air shower does

spread out appreciably so that the circular light pool that reaches ground level has dimensions of several hundreds of meters; hence even a small optical detector has a collection area of > $3x10^8$ cm^2. Finally the amount of light radiated is proportional to the total number of particles in the shower and is not strongly absorbed by the atmosphere; hence the Cherenkov light is a calorimetric component of the shower and can be used as a good estimator of the primary energy with about 30% uncertainty for an individual event (Weekes, 1995).

Because of the smaller transverse momentum in electromagnetic interactions mentioned above the electromagnetic cascade is much more compact than its hadronic equivalent. Not only does the extensive air shower develop earlier it is laterally more regular from 10 to 15 km above sea level to ground level.

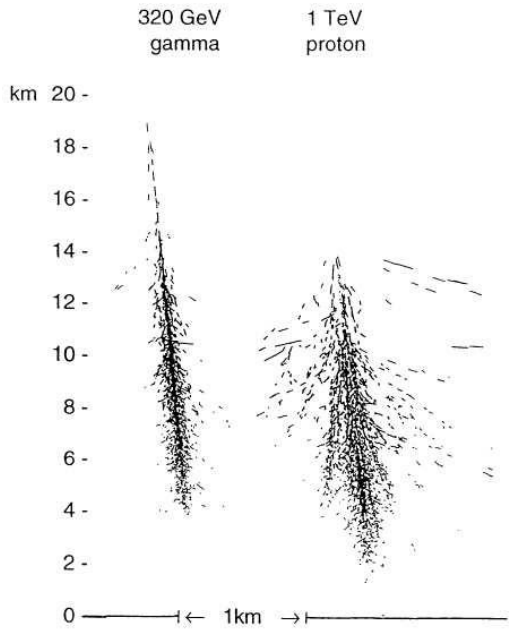

Fig 2.6: Simulation of the two principle means of creating Extensive Air Showers (Hillas, 1996).

2.4.2: Properties of cosmic ray induced showers

Monte Carlo simulations of extensive shower formations have shown that although the images of gamma ray and hadronic induced showers are similar it is possible to differentiate between them, at least in a general way (Weekes, 1995). On entering the Earth's atmosphere the great majority of cosmic rays collide with atomic nuclei in the atmosphere, producing secondary cosmic rays (consisting mainly of elementary particles). The air shower produced is complex but well defined; the initial products are

usually charged and neutral pions though a large component of the initial energy of the incoming hadron may still be maintained thus producing perhaps several extensive air showers from the original progenitor; refer to Fig 2.7. Neutral pions decay to gamma rays and the resulting gamma rays create electron-positron pairs and more photons by *bremsstrahlung*. The charged pions decay into muons, some of which decay into neutrinos and electrons while many more penetrate to ground level.

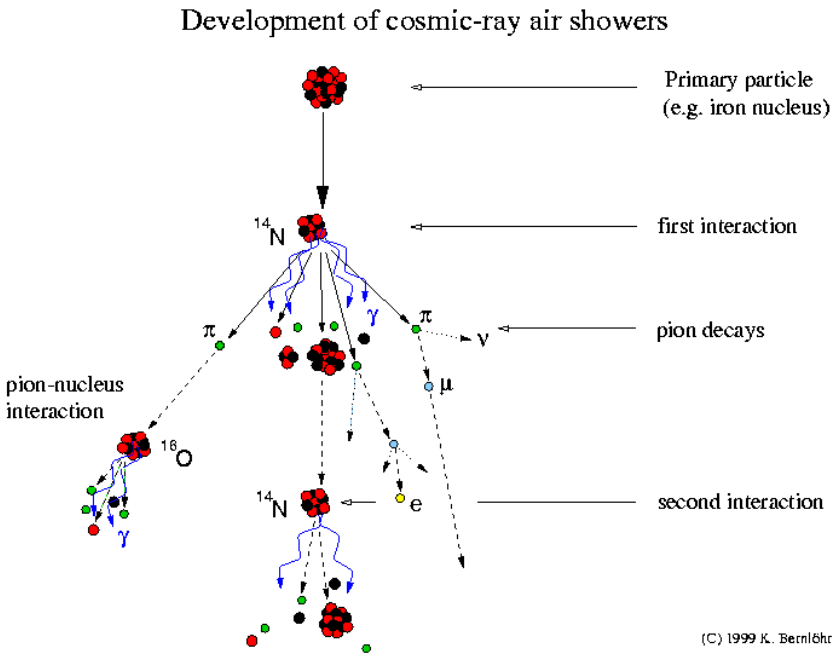

Fig 2.7: Cosmic ray production of extensive air showers. Courtesy of Konrad Bernlöhr, Max Planck institute.

2.5: What is Cherenkov light?

A young PhD student by the name Cherenkov (Pavel Alekseyevich, born in the Voronezh Region of Russia on July 28, 1904) found that whenever high energy charged particles pass through a transparent gas, liquid, or other medium at velocities greater than the speed of light for that substance secondary light is created. We remember that Special Relativity states that nothing can travel faster than the speed of light 'in a vacuum'. However the speed of light in a medium may be considerably less. In air the refractive index, $n = \frac{c}{v} = 1.00029$ where c is the speed of light and v is the velocity of the particle (Jackson, 1975). The refractive index will vary with density so altitude is a factor in

estimating accurately the refractive index. In water the speed of light is only 0.75c. As the charged particle travels through the medium it disrupts the local electromagnetic field. Electrons in the atoms of the medium will be displaced and the atoms become polarized by the passing electromagnetic field of a charged particle. Photons are emitted as the insulator's electrons restore themselves to equilibrium after the disruption. In normal circumstances these photons destructively interfere with each other and no radiation is detected. However when the charged particle generates a photonic shock wave as it travels through the insulator faster than the speed of light through the medium, the photons constructively interfere and intensify the observed radiation, refer to Fig 2.8.

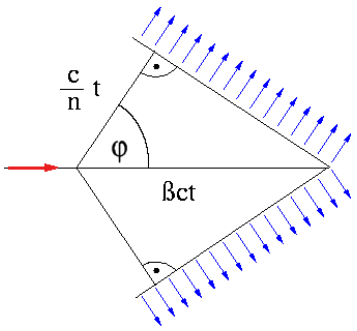

Fig 2.8 the arrow represents the charged particle, while the multiple arrows represent the Cherenkov radiation.

As mentioned a local and transient polarisation is set up in atoms near the particle, emitting coherent radiation at an angle θ where

$$\text{Cos}\ \theta = {}^{c}/_{vn} = {}^{1}/_{\beta n} \qquad (2.1)$$

Where $\beta = v/c$. $\theta \cong 1.3^{o}$ for air when $\beta \rightarrow 1$.

If we set θ to 0^{o} then the threshold velocity v_t defines the minimum particle velocity that will produce Cherenkov light given by,

$$v_t = c\ /\ n \qquad (2.2)$$

The radiation output in air is peaked in the ultraviolet region, decreasing with an inverse dependence of λ^2, where λ is the wavelength of the emitted light.

In terms of the Earth's atmosphere such showers typically occur as gamma rays approach within 10 km of sea level and the resulting Cherenkov light projects a light cone (or "light pool") roughly 250m in diameter at ground level. This can be visualized taking $\theta \cong 1.3^{o}$ and examining Fig 2.6 which illustrated the pair production that gives rise to the charged particles in comparison to hadronic showers. In the case of the telescope used for this analysis the Earth's atmosphere is used as the detection medium implying a collection area of many thousands of square meters.

In order to detect a flash of Cherenkov light a telescope has to have photomultiplier tubes and ultra fast electronics to allow for triggering and for short exposure times of a few nanoseconds, which is the duration of the Cherenkov light flash. Longer exposure times would lead to drowning out of the images because of the night sky background, mostly from scattered starlight.

The energy threshold, E_t, for Cherenkov radiation production is given by the following formula,

$$E_t = \frac{m_o c^2}{\sqrt{1-\left(\frac{v_t}{c}\right)^2}} \qquad (2.3)$$

Where m_o is the mass of the particle and v_t is its threshold velocity. The threshold energy for the production of Cherenkov light in air is 39 GeV for protons, 22 MeV for electrons and 4.4GeV for muons (Allen, 1977).

There is still a goal to aim for in telescope development as extensive air showers originating from primary gamma rays of a few GeV still produce enough Cherenkov light to be detectable by sufficiently sensitive telescopes according to Merck et al., (2003). Though the successor to the Whipple telescope is only fully operational for 2 ½ years there are plans for the next generation of ground based telescope that will be sensitive to the production of Cherenkov light from ever smaller fluxes (R. Wagner et al., 2010).

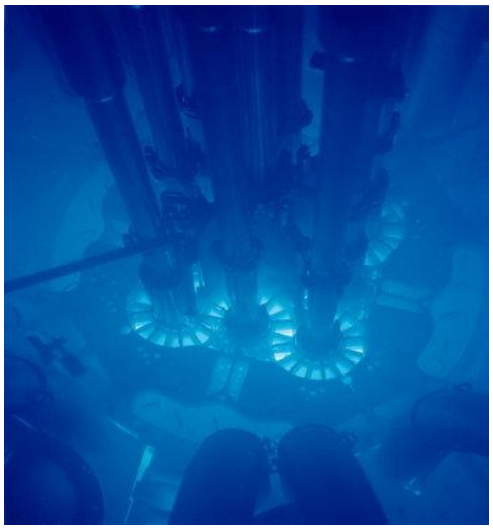

Fig 2.9: A photograph of a 'hot' core of a nuclear reactor where relativistic particles in the water emit Cherenkov light. Courtesy of Idaho National Laboratory.

2.6: Relative incidence of high energy electromagnetic photons

Only a tiny fraction of the light reaching us from the universe is in the visible range which covers about one octave from red to blue. The full electromagnetic spectrum observed today ranges over 30 decades in frequency, from radio to gamma rays.

In 1912 the Austrian physicist and Nobel Prize winner Victor Francis Hess discovered cosmic rays. These particles (>99.9%) and photons (<0.1%) arrive at the Earth's upper atmosphere with a flux roughly $\propto {}^{1}/_{log_{energy}}$ as is clearly illustrated in Fig 2.10. The purple region representing cosmic rays of extra galactic origin (the most energetic) were until the time of this publication, of unknown origin. The VERITAS collaboration has made a major leap in understanding their origin with studies of M82 (Acciari et al. 2009). Cosmic rays enter the Earth's atmosphere with energies extending beyond 10^{20} eV and a flux decreasing by $\cong$ 28 orders of magnitude over the energy range 10^{9} to 10^{20} eV, as seen in Fig 2.10. Between 10^{12} eV and 10^{15} eV about 89% of cosmic rays are protons, about 10% are Helium and roughly 1% are heavier nuclei, while a very small percentage are gamma rays. The Spectral Index (the slope of log energy vs. log flux plot) is approximately - 3 for cosmic rays, while for gamma ray sources the spectral index is from -3 to -2.

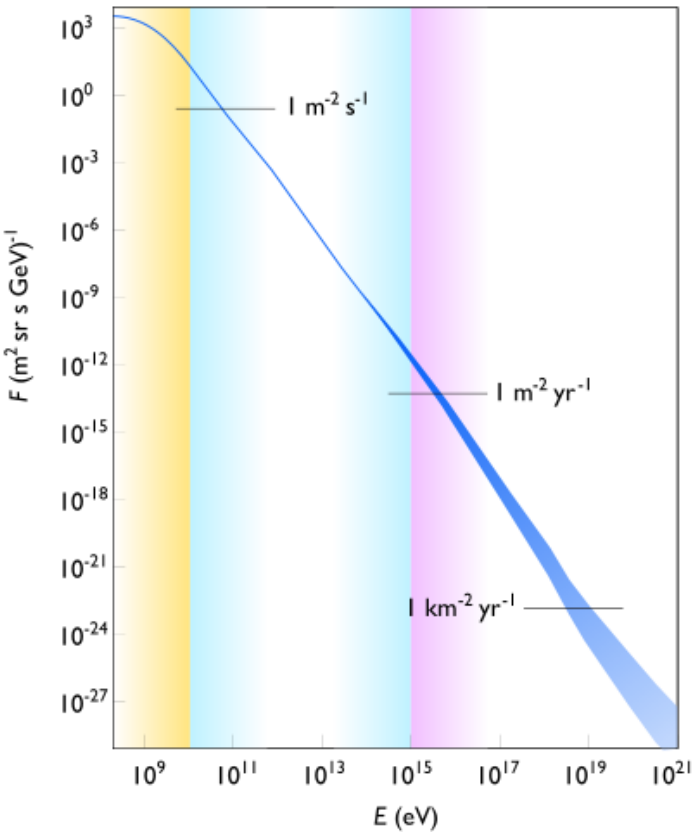

Fig 2.10: The flux of cosmic ray particles as a function of their energy. The flux for the lowest energies (yellow zone) are mainly attributed to solar cosmic rays, intermediate energies (blue) to galactic cosmic rays, and highest energies (purple) to extragalactic cosmic rays (Swordy, 2001)

From the above information it is becoming clear that having a large detection area will be essential for VHE gamma ray observations. The fluxes involved are small. Ground based detection is irreplaceable, for the limits on detection area which satellites are subject to do not hold. Ground based Imaging Atmospheric Cherenkov Telescopes need only be placed in the light pool of 100m in diameter (refer to Fig 2.1) for detection to be possible while the space based platform must detect the photon directly; there being no detection medium in the vacuum of space. Of course should an array of telescopes be used a greater ground area would be covered; in fact if the mirrors are separated by ≈ 100m this would ensure they effectively overlap due to the large light pool area. Fortunately the very low flux of gamma rays of $E_\gamma > 100$ GeV is overcome thanks to this large detection area. Thus the future of ground based gamma ray observation is very much open to new developments such as CTA (Cherenkov Telescope Array) where increased sensitivity due to large scale stereoscopicity (20+ mirrors) will greatly further research of low flux sources (R. Wagner et al., 2010).

2.7: History

Having briefly introduced the fact that gamma rays can be observed from ground based instruments then giving the mechanisms by which gamma rays make themselves detectable and finally illustrating the relative abundance of these photons in relation to cosmic rays, it is now time to examine the history of the Imaging Atmospheric Cherenkov Telescope. In 1948 the English experimental physicist, Patrick Blackett, considering all the different sources of light which contribute in some measure to the light of the night sky predicted that there should be Cherenkov light emission from relativistic cosmic particles impinging on the Earth's atmosphere and estimated that these should give some small contribution (0.01%) into the total intensity of the light of the night sky (Blackett, 1948).

Confirmation of that prediction and the beginning of the atmospheric air Cherenkov technique came about with the discovery of Galbraith and Jelley (1953). They used a single 5cm diameter PMT in the focal plane of a simple parabolic mirror of 25cm diameter all housed in a new garbage can! The output of the PMT was coupled to an amplifier with a state of the art 5 MHz amplifier whose output was displayed on an oscilloscope. They observed oscilloscope triggers from light pulses that exceeded the average noise level of the night-sky background every two minutes.

At the outset of this novel observation method just a single PMT placed in the focus of a small mirror was used to build the instrument (the so called 1^{st} generation telescopes, refer to fig 2.2). These were followed by an increase in scale using larger reflectors for individual telescopes and employing more than one telescope and by setting them in time coincidence. Typically the early telescopes consisted of a searchlight mirror of 1m to 2m diameter and a field of view of approximately 0.5^{o} again with just a single PMT at their foci as can be seen in Fig 2.11. The early ingenuity of the gamma ray pioneers is evident in this joint Irish-British collaboration, where a WWII gun turret was given a more peaceful job to perform. May this be an example for future generations to follow.

Fig 2.11: The second ground-based gamma-ray telescope, the British-Irish experiment at Glencullen, Ireland (1964). The telescope consisted of two 90 cm searchlight mirrors on a Bofors gun mounting. The experiment was led by Jelley and Porter.

This remained essentially the astronomical technique from the late 50's to the 70's. Observations from the Crab Nebula taken from 1969-1972 using the 10m optical reflector at the Whipple observatory, again with a single PMT, yielded an excess of gamma rays (a statistical significance) at the 3 standard deviation level (3σ) (Fazio et al., 1972). This was below the now recognized threshold of 5σ required for the detection of a VHE source.

After the early improvements and successes there was little further development in ground based gamma ray telescopes for over a decade. Many physicists thought the field was a dead end. The question is why did the development receive new impetus in the 1980's? This question will be answered to some degree by the end of this brief thesis. In short the time had arrived to delve into the relativistic universe thanks to the development of imaging cameras and superior gamma ray/hadron separation techniques by means of the introduction of the second moment parameterization of images by Hillas (1985). This allowed the light from the far greater number of hadronic induced extensive air showers to be rejected so as to bring the gamma ray induced events to the fore.

The main camera developmental milestone arrived in the 1980's with the use of an array of PMT's arranged on a two dimensional plane (instead of a single PMT) placed at the focal plane of a large reflector. This allowed an image of the Cherenkov light to be

recorded. Though the difference between gamma ray and hadronic extensive air showers became clearer they still had to be differentiated accurately. The Cherenkov light from a gamma ray is considerably more compact than its cosmic ray counterpart. Hillas demonstrated that both the image shape and the orientation contribute to the efficient selection of gamma ray shower images from the much more numerous hadron showers. In spite of the originally crude pixelation of imaging cameras (the 1st imaging camera of the Whipple Imaging Atmospheric Cherenkov Telescope had just 37 pixels of 0.25^{o} each) application of Hillas parameterization to the Whipple data provided the first highly significant measurement of gamma rays from the Crab nebula in 1988 (Weekes et al., 1989). This apparatus provided the first statistically significant detection of the Crab Nebula. It is interesting to note that a model for the production of gamma rays from the Crab nebula by Weekes of the Whipple observatory (a pioneer of ground based VHE gamma ray astrophysics) preceded this experimental discovery by 20 years (Rieke and Weekes, 1969) and this was preceded by Philip Morrison 10 years previously (Morrison, 1958).

The Whipple collaboration is an international grouping of High Energy Astrophysicists from the United States, Ireland and England who have their base at the Harvard-Smithsonian centre for Astrophysics in Amado, Arizona. Here the atmospheric technique developed further. The next improvement to sensitivity was to incorporate more than one imaging telescope. The Whipple collaboration had used the only available space in the vicinity of their telescope on Mount Hopkins, located 140m from the 10m, in order to install a second 11m telescope which saw first light in late 1991 with a medium resolution camera of 37 photomultipliers (pixel size 0.25^{o}). During the first 18 months of operation of the 11 meter reflector several technical problems were encountered and solved. The stability and the absolute positioning of the telescope mount were significantly improved, though it was never stable enough for all zenith angles. A CCD camera was installed as a check on its pointing direction. Its medium resolution camera was replaced during the summer 1993 with a 109 pixel high resolution camera to match the 10m and the data acquisition electronics for both reflectors was significantly upgraded. The large distance between the telescopes and the inferior performance of the 11m provided a rather low coincident rate. The second

telescope was abandoned after a short lifetime owing to a heavy ice storm that caused the collection of so much frozen material on the superstructure that the telescope broke from its mounting under the weight and rolled several meters down the mountain. Stereoscopic observation would have to wait. The 10m telescope has undergone a number of upgrades to its camera during the 1990's. With a new camera upgrade the 10m Whipple could enter service alongside its successor for long term monitoring of Active Galactic Nuclei.

Fig 2.12: The Imaging Atmospheric Cherenkov Telescope layout of the VERITAS stereoscopic array.

The VERITAS array (Very Energetic Radiation Imaging Telescope Array System) saw first light in 2007. The VERITAS Collaboration is the successor to the Whipple Collaboration. The current generation of imaging atmospheric Cherenkov experiments consists of arrays of several reflectors and the VERITAS Collaboration is now operating an array of four twelve metre reflectors (Kieda, 2007; Weekes, 2006) as can be seen in Fig 2.12. Results from early observations were reported at the 30th International Cosmic Ray Conference. However the results presented at the 31st International Cosmic Ray Conference presented a more complete series of observations thanks to two full years of operational experience (Ong et al., 2009). The combined array of telescopes provides a maximum sensitivity, point source detection of 1% of Crab flux in < 50h, 10% of Crab flux in 45 min, in the energy range 50 GeV to 10 TeV The lower limit rarely breaks the 100GeV range at the time of writing. Recent highlights from VERITAS include observations of the following objects; *SNR IC 443* (Acciari et al., 2009); *3C 66A* (Acciari et al., 2009); *M87* (Acciari et al., 2008) in addition to Ong et al. (2009).

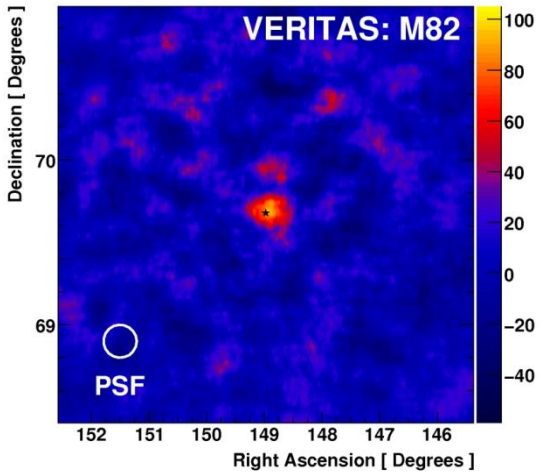

Fig 2.13: VERITAS image of the starburst region M82, published in Nature.

Of all the recent publications the most noteworthy would possibly be the observations of M82, (Acciari et al. 2009). In this prototype small starburst galaxy, the VERITAS collaboration reported on the detection of >700 GeV gamma rays. From these data it was determined that a cosmic ray density of 250 eV cm^{-3} is present in the starburst core, which is about 500 times the average Galactic density. This links cosmic ray acceleration to star formation activity and suggests that supernovae and massive star winds are the dominant accelerators. Refer to Fig 2.13 for the TeV sky map centered on M82 which was taken over 137 hrs.

VERITAS is by no means the only instrument to have made an impact in the VHE gamma ray field. H.E.S.S (High Energy Stereoscopic System, energy threshold of 100 GeV) is located in Namibia near the Gamsberg mountain. The H.E.S.S instrument allows scientists to explore gamma ray sources with intensities at a level of a few thousandths of the flux of the Crab nebula. The first of the four telescopes of Phase I of the H.E.S.S. project went into operation in summer 2002; all four were operational in December 2003. The following are publications of interest; HESS proceedings of ICRC 2001; (Tibolla et al. 2009); (Aharonian et al. 2009). In additions to ground based observations a new series of space based instruments has been making an impact too. The newest generations of space based instruments are housed on Fermi gamma ray Space Telescope (formerly called GLAST, Gamma ray Large Area Space Telescope) which is an international and multi agency space observatory that studies the cosmos in the photon

energy range from 8 keV to greater than 300 GeV. For recent work see; *GRB 080916C* (Abdo et al. 2009), *active galactic nuclei* (Abdo et al 2009).

2.8: VHE gamma ray sources and production

Having examined the physics and the instrumentation that makes ground based gamma ray astronomy possible attention is now turned to the sources themselves and the mechanisms that produce VHE gamma rays.

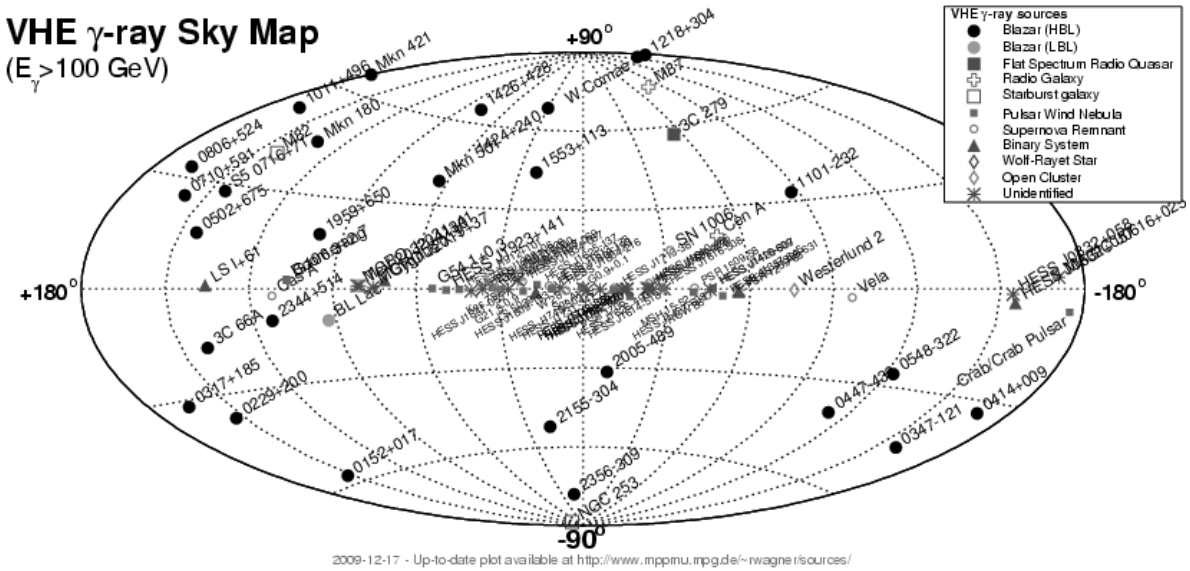

Fig 2.14: Up to date TeV catalogue containing over 80 known gamma ray sources. Courtesy of MAGIC.

Referring to Fig 2.14, this up to date TeV catalogue is courtesy of the MAGIC collaboration who operate two 17m Imaging Atmospheric Cherenkov Telescopes on the Roque de los Muchachos site, situated on the Canary island of La Palma. At present there are about 80 known TeV sources; refer to the Appendix A for a full listing. Of note is the concentration of sources along the galactic plane as is to be expected. Active Galactic Nuclei, being isotropically spread throughout the entire sky field of view, should now present the best hope of finding steady TeV emitters.

2.8.1: Physical processes involved in gamma ray production

Astrophysicists have a number of standard models for gamma ray production. In one, highly accelerated electrons collide into low energy photons, 'bumping' them up to gamma ray energies. This is called inverse Compton Scattering as the photons are scattered with increased energy. In another model, collisions between high speed protons and low energy protons or photons create neutral pions (π^0) that decay into gamma rays, average lifetime being 8.4 x10^{-15} sec. This is called neutral pion decay. A common scenario would be the collision between a cosmic ray proton and a stationary hydrogen atom, producing excited states that lead to emission of pions, as follows:

$$p + p \rightarrow N + N + \pi^+ + \pi^- + \pi^0$$

$$\text{after} \approx 10^{-16} \text{ sec}$$

$$\pi^0 \rightarrow 2\gamma$$

where p are protons and N is a proton or neutron and π^0 is the neutral pion.

Although both mechanisms can generate TeV gamma rays, two other mechanisms are operative when the energies of electrons are relativistic or the magnetic field is extremely strong, and usually a combination of both. One process involves the interaction of a fast moving electron with an extremely strong magnetic field. The magnetic field sweeps the electron into a curved trajectory. If the trajectory is of sufficiently small radius, the electron will lose energy by emitting high energy gamma rays, refer to Fig 2.15. Synchrotron radiation is the radiation emitted from charged particles when they are forced from their original trajectory by the incident magnetic field. Two of the characteristics of synchrotron emission include non-thermal power-law spectra and polarization. Synchrotron emission is important is the pulsar wind nebulas (or plerions) of which the Crab nebula and its associated pulsar are archetypal. Pulsed emission gamma ray radiation from the Crab has recently been observed up to ≥25 GeV (Aliu et al., 2008).

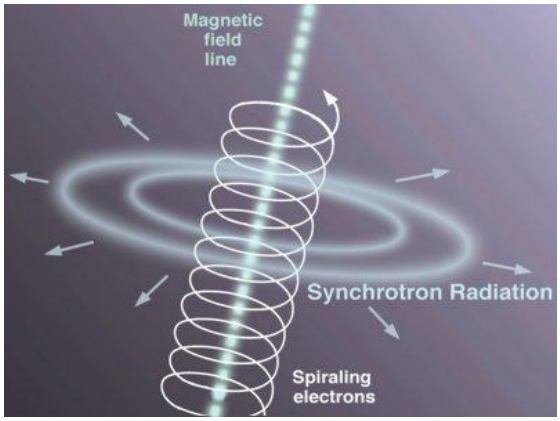

Fig 2.15: Representation of an electron in an intense magnetic field showing the emission direction of Synchrotron radiation. Courtesy of Astronomy online.

2.8.2: Leptonic Gamma Ray Production

Gamma rays may also be produced as the result of a combination of Synchrotron radiation and Compton Scattering. Compton Scattering results when a photon imparts energy to a particle after collision. From the law of conservation of energy,

$$E_\gamma + E_e = E_{\gamma'} + E_{e'}$$

where $E_{e'} > E_e$. Non thermal X-ray emission observed from several Super Nova Remnants including SN 1006 (Koyama et al., 1995), and Cassiopeia A (Allen et al., 1997), has been interpreted as synchrotron radiation of high energy electrons in the ambient magnetic fields (Lessard, 1999) where electrons have reached relativistic energies by Compton scattering. With Compton-Synchrotron emission, the gamma rays increase the energy of electrons (reaching relativistic energies) by imparting their energy to them in collision. These relativistic electrons then enter strong magnetic fields, for example in the vicinity of pulsars, and emit TeV gamma rays.

2.9: Gamma ray sources

Having seen the relative incidence of VHE gamma rays and having examined briefly the physical mechanisms that produce these VHE photons, we look now at the environments that produce them.

2.9.1: Pulsars

Pulsars are remnants of collapsed stars. In a simplified picture they are giant atomic nuclei consisting mostly of neutrons being held together by gravity. They typically have radii of only 10 km while having a mass > 1.4 $M_{\odot}$, where $M_{\odot}$= 1 solar mass (Holliday, 1999), and spin around their axes up to hundreds of times per second. Neutron stars and the surrounding plasma are enveloped in large magnetic fields of up to 10^9 Tesla.

Observed modulation of the gamma ray light curves corresponding to the periods of rotation of these objects indicates that sub-TeV gamma rays are produced near the surface of neutron stars by Synchrotron radiation (Sturrock, 1971). The sub-TeV gamma rays may then increase the energies of electrons to relativistic levels (Compton scattering) and in Inverse Compton scattering these relativistic electrons collides with sub-TeV gamma rays, and in turn are scattered with energies in the gamma ray range. These newly generated VHE photons may encounter a magnetic field so strong, either at the polar cap or in the vacuum gaps at the outer magnetosphere, that an electron-positron pair may be created (Harding, 1997). This pair of particles may then be accelerated to energies sufficient to produce more gamma rays and so on. The electron-positron pair may encounter charge depleted regions or 'gaps' that can cause particles to be accelerated to energies > 1 TeV. One of the principal models for gamma ray production in pulsars is the outer gap model. Here it is assumed that particles are accelerated in the vacuum gaps of the outer magnetosphere (Cheng and Ruderman, 1986). This process can produce a large component of the electric field along the magnetic field lines in these gaps, from where the charged particles may be accelerated and radiate gamma rays tangential to the field.

2.9.2: Super Nova Remnants

As the Crab nebula forms part of the present analysis some time will be given to understanding it. The Crab nebula (M1) was the first detected steady source of TeV photons and remains the standard candle for VHE observations in the northern hemisphere. The distance to the Crab nebula is not universally agreed upon but in 2008 the consensus is that its distance from Earth is 2.0 ± 0.5 kpc (6.5 ± 1.6 kly). The Crab

Nebula is currently expanding outwards at about 1,500 km/s. The Crab is a plerion, a pulsar wind nebula formed from a supernova remnant which 'exploded' or blew off a major part of its mass in 1054 AD, being visible in broad daylight for almost 3 weeks (peak magnitude of -5!). The Crab Pulsar that remains is believed to be about 28–30 km in diameter and it emits pulses of radiation every 33 milliseconds. Like all isolated pulsars its period is slowing very gradually. Occasionally its rotational period shows sharp changes (known as 'glitches') which are believed to be caused by a sudden realignment inside the neutron star. The energy released as the pulsar slows down is enormous and it powers the emission of the synchrotron radiation of the Crab Nebula, which has a total luminosity about 75,000 times greater than that of the Sun (Kaufmann, 1996). The explosion cloud that remains is filled by plasma heated by a high energy wind of electrons. These are emitted from the remainder of the collapsed core of the exploded star. The electrons reveal themselves by the bluish light from the interior of the cloud which can be interpreted as synchrotron radiation. This is evident in Fig 2.16.

Electrons and positrons escape from the magnetosphere along the open magnetic field lines and enter the pulsar wind region. The particles are accelerated by the pulsar wind termination shock (with energies up to 10^{14} eV). After they are accelerated to these high energies, they escape the shock front and enter the nebula, interacting with nebular magnetic and photon fields to produce very bright synchrotron and Inverse Compton gamma ray emission This has been observed over 20 decades of frequency from 10^{7} to 10^{27} Hz. Due to the large magnetic field of the Crab Nebula, $B \cong 2\text{x}10^{-4}$ G, only $\approx 0.1\%$ of the energy of electrons is converted to Inverse Compton gamma rays. The rest being radiated in the form of optical, UV, and X-ray synchrotron photons as can be seen in Fig 2.16. This model is known as the synchrotron self-Compton model**.** Generation of TeV gamma rays in the Crab nebula requires the presence of TeV electrons; these are accelerated in the outer gap as mentioned above. This model is now favoured above the polar cap model.

2.9.3: Multi wavelength observation of the Crab Nebula

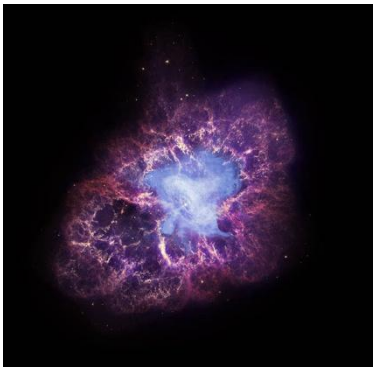

X-ray:

This X-ray image (central blue form) of the Crab Nebula traces the energetic particles being produced by the pulsar. This image reveals an unprecedented level of detail about the highly energetic particle winds. This image superimposes x-ray, optical and infrared, to allow the scales of area to be maintained.

Optical:

As time goes on and the electrons move outward, they lose energy to radiation. The diffuse optical light comes from intermediate energy particles produced by the pulsar. The optical light from the filaments is due to hot gas at temperatures of tens of thousands of degrees.

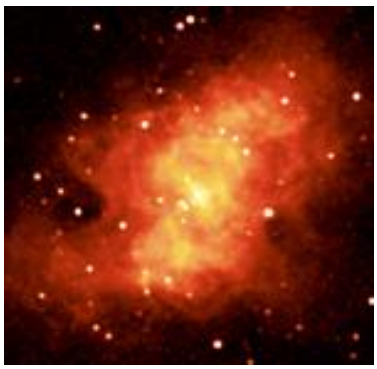

Infra-Red:

The infrared radiation comes from electrons with energies lower than those producing the optical light. Additional infrared radiation comes from dust grains mixed in with the hot gas in the filaments.

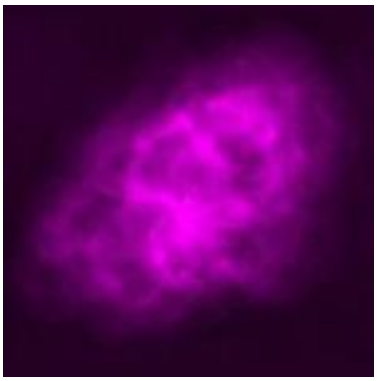

Radio:

Radio waves come from the lowest-energy electrons. They can travel the greatest distance and define the full extent of the nebula. The Crab's central pulsar was discovered in 1968 by radio astronomers. The pulsar was then identified as a source of periodic optical, X-ray and gamma ray radiation. The periodic flashes of radiation are caused by a beam from the rapidly rotating neutron star.

Fig 2.16: Photos courtesy of CHANDRA collaboration, Harvard (http://chandra.harvard.edu/photo/1999/0052/what.html)

2.9.4: Active Galactic Nuclei

Active Galactic Nuclei are the most energetic phenomenon observable in extragalactic astronomy. In the unified model of active galactic nuclei the central engine contains a supermassive black hole of mass $\cong 10^7$ to 10^{10} $M_{\odot}$. There is a thin accretion disk around the black hole, surrounded by a thick torus lying in the equatorial plane of the hole that would feed the accretion disk and replace matter drawn into the local singularity. Radio loud Active Galactic Nuclei have well collimated jets perpendicular to the accretion disk which extends out from the 'poles' as can be seen in Fig 2.17. In this model the central engine is powered by accretion; the change in gravitational potential energy of in falling matter which is a very efficient process that may convert as much as 10% of the rest mass of the accreted matter into radiation.

Active galaxies emit radiation over the entire electromagnetic spectrum, from radio waves to TeV gamma rays and beyond. Thermal emission emanates from the accretion disk (infrared to X-rays) and the torus (infrared). Non thermal emission (radio and gamma rays) emanates from the jets and is highly collimated. Detection of gamma rays from AGN is confined to cases where the direction of these jets lie along the line of sight to the telescope. This would possibly explain the rare nature of TeV sources.

Superluminal motion in the jets, apparent motion that is greater than the speed of light, has been observed in many Active Galactic Nuclei: it is a consequence of relativistic flow viewed at small angles. The relativistic beaming also causes the apparent luminosity to increase dramatically and allows high-energy photons to escape from regions with high radiation fields.

The initial search for Active Galactic Nuclei had its space based component fulfilled by The Energetic Gamma Ray Experiment Telescope (EGRET), one of the four scientific instruments on NASA's Compton Gamma Ray Observatory satellite, now decommissioned. It detected individual gamma rays with energy from 30 MeV to 30 GeV. The huge apparent gamma ray luminosities of some of the EGRET catalogue of Active Galactic Nuclei coupled with their rapid variability hint at a strongly anisotropic character of high energy radiation which can be attributed to the relativistic bulk motion

of plasma jets ejected from a compact source. This hypothesis is supported by the fact that all compact extragalactic EGRET sources are identified with a specific class of Active Galactic Nuclei (blazars) in which the non thermal radiation is produced by relativistic jets directed along angles close to the observer's line of sight.

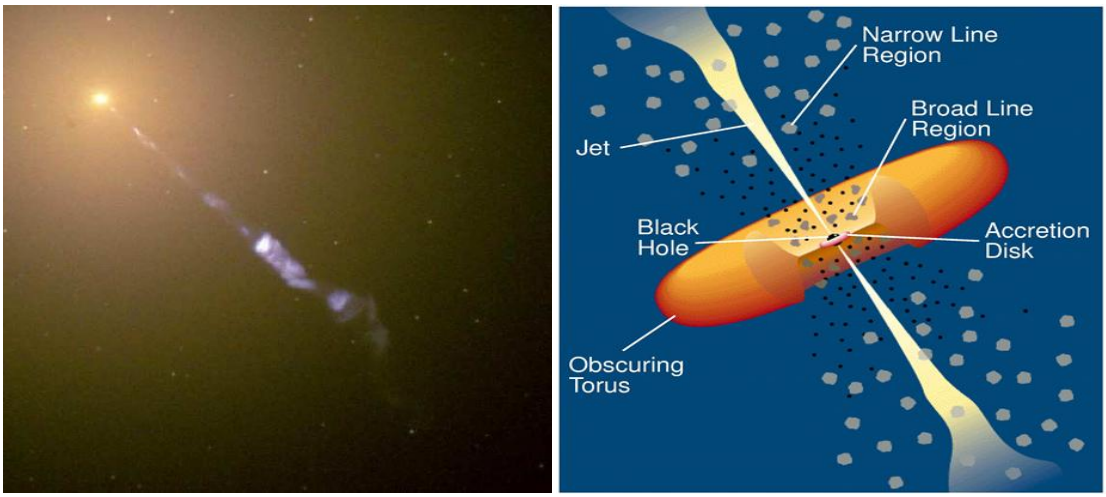

Fig 2.17: LEFT: A Hubble Space Telescope image of the giant radio galaxy M87 clearly showing the plasma jet emanating from its core. RIGHT: Cartoon depicting the canonical model of jets associated with the massive black holes at the center of Active Galactic Nuclei. Figures courtesy of the Hubble Heritage Team (heritage.stsci.edu).

The above AGN in Fig 2.17, M87, is a known TeV source though the direction of the jets are not along the line of sight. Due to its proximity we can detect a weak flux of gamma rays from this galexy but this is an exception.

Since 1992 the Whipple Collaboration has been searching for TeV gamma ray emission from Active Galactic Nuclei. Initially the search was concentrated on blazars detected by EGRET at any redshift; these observations led to the detection of Mrk 421 (Punch et al., 1992) and upper limits on some 30 other blazars (Kerrick et al., 1995). Markarian 421 was first detected as a weak GeV source with a flat spectrum (Lin et al., 1993). Soon long term observations were carried out in search of periodicity (Schubnell et al., 1995) but strong outbursts were instead detected (Kerrick et al., 1995b). In the late 1990's, the search had concentrated on nearby BL Lacs leading to the detection of Mrk 501 (Quinn et al., 1996) and 1ES 2344+514 (Catanese et al., 1998). BL Lacertae (BL Lac)

objects are a subclass of the blazar (hence BL) class of active galactic nucleus. Between 1995 and 1998 the survey included 24 objects ranging in redshift (z) from 0.046 to 0.44.

The first multiwavelength campaign on Markarian 421 coincided with a TeV flare on May 14-15, 1994 and TeV emission did show some correlation with the X-ray band. Another multiwavelength campaign was undertaken in 1995, refer to Fig 2.18, where there is evidence of correlation between gamma ray emission and X-ray emission on modified Julian date 49833. However, no enhanced activity was seen by EGRET (Macomb et al., 1995).

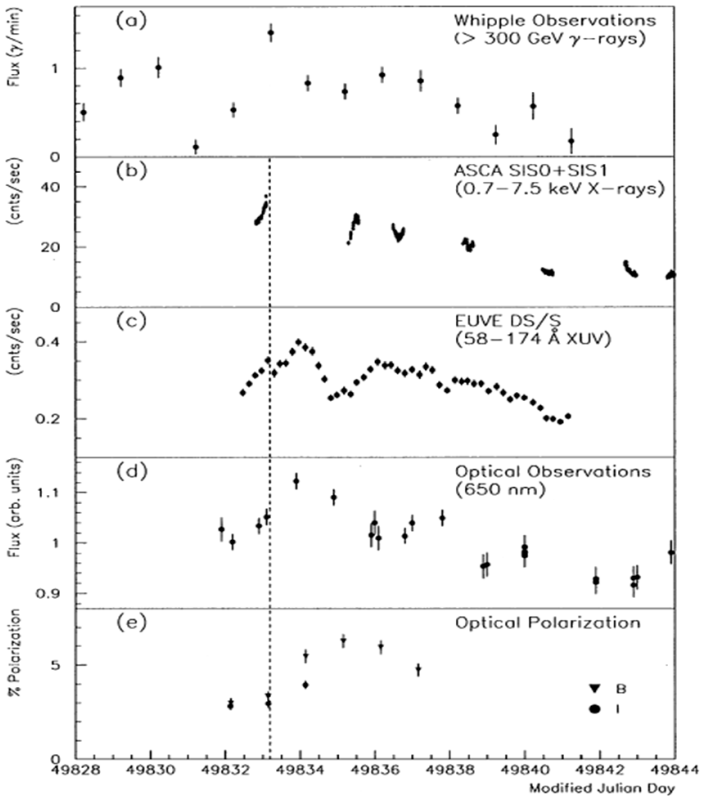

Fig 2.18: Multi wavelength observations of Mrk 421 taken in April and May 1995 (Buckley et al 1996). The light curves from: (a) VHE gamma ray, (b) X-ray, (c) extreme UV, and (d) optical observations are shown. Optical polarization measurements are shown in (e). The error bars are statistical.

Over the next few years there was some correlation between X-ray emission and VHE gamma rays emission though not well correlated. Perhaps the most noteworthy phenomenon of the VHE emission from Markarian 421 is the event rise, the time over which an emission reaches a specific peak level. It is on the order of a day or shorter.

This type of emission is termed “flaring” which has produced emissions as high as 10 times the Crab flux (Gaidos et al., 1996) but flares on the order of half of the Crab flux are more typical (Buckley et al., 1996; Quinn et al., 1996; Quinn et al., 1997; McEnery et al., 1997). The normal baseline emission level for this object can be very low; Markarian 421 has once dropped below the detection limit of the Whipple 10m for as long as a month (Buckley et al., 1996; McEnery et al., 1997).

2.5.5: AE Aquarii

Though not of central concern to this thesis consideration will now be given to AE Aquarii. In the early 1990’s a large amount of observational time was devoted to this binary system, and though it did not produce positive results for VHE gamma ray emission, only the centre of field of view was analysed. The archival data was to be the subject of an analysis that would determine if a VHE gamma ray source may lie in the Field of View.

AE Aquarii is a DQ Her type cataclysmic variable at a distance of ≈ 100 pc (Robinson et al., 1991; Welsh et al., 1993). A DQ Herculis Star (also called an Intermediate Polar) is a type of cataclysmic variable binary star system, refer to Fig 2.19. In most cataclysmic variables matter from a main sequence companion star is gravitationally stripped by a white dwarf star in the form of an accretion disk. X-rays are generated by high velocity particles from the accretion stream forming a shock as they fall onto the surface of the white dwarf star. As particles decelerate and cool before hitting the white dwarf surface, bremsstrahlung X-rays are produced and may subsequently be absorbed by gas surrounding the shock region. The light curve of an intermediate polar may show several types of stable periodic changes in brightness. One periodicity is related to the orbital period of the binary star system. A second periodic signal originates from the rotation of the white dwarf spinning on its axis. A third light curve periodicity, the sideband period between the spin period and the orbital period, is also often present. In addition to the stable oscillations, unstable oscillations called "quasi-periodic oscillations" may appear and then die off after a few cycles.

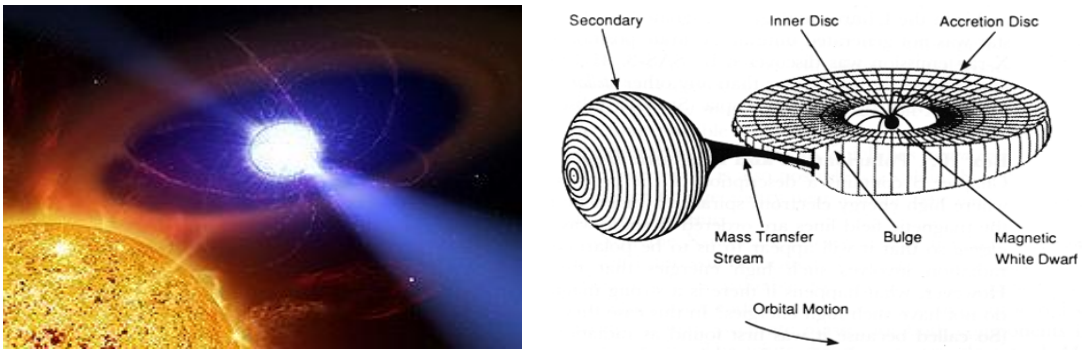

Fig 2.19: LEFT: artists impression of AE Aquarii showing red dwarf and white dwarf with disk visible. RIGHT: schematic showing the lines of force responsible for drawing matter. Courtesy of NASA.

At the time of observation it was noted that the secondary star consists of a K5 late-type red dwarf and a white dwarf with an orbital period of 9.88 hours. The optical behaviour of AE Aquarii exhibits large flares, highly coherent pulsations at F_o = 30.23 mHz and quasi-periodic oscillations (Patterson, 1979). The optical magnitude varies from $\approx$ 12.5 in the quiescent state up to $\approx$ 10.0 during flares which can last from minutes to hours (Lang et al., 1993). AE Aquarii has the highest known rotation frequency of the DQ Her type cataclysmic variables. A detailed analysis of 68.7 hours of data recorded on AE Aquarii has revealed no evidence for any steady, pulsed or episodic TeV emissions (Lang et al., 1993).

Chapter 3

The Imaging Atmospheric Cherenkov Technique

3.1: The Telescope

A remarkable feature of the atmospheric Cherenkov technique is its high detection rate capability, a consequence of the large collection area of air showers ($S_{eff} \approx 3x10^8$ cm^2). The effective radius of the Cherenkov light pool depends only slightly on the energy of the primary gamma rays while the intensity of the lightly is more or less calorimetric.

Operating as a single detector an Imaging Atmospheric Cherenkov Telescope array can reconstruct the arrival direction of gamma ray primaries to an accuracy of $\theta \approx 0.1^o$. For point like gamma ray sources this alone provides suppression of the cosmic ray background by a factor of several hundred. A comparable reduction of the cosmic ray contamination can be gained by discriminating the intrinsic differences between the electromagnetic and hadronic showers, based on the shape and size of the light image. This implies that a 100 GeV threshold Imaging Atmospheric Cherenkov Telescope array covering ≥ 0.1 km^2 area would be able to search for VHE gamma ray sources at an unprecedented energy flux level of 10^{-13} erg cm^{-2} s^{-1}, which is impressive even by the standards of more traditional branches of modern astronomy.

In practice an energy threshold of 100 GeV can be achieved by a stereoscopic system of Imaging Atmospheric Cherenkov Telescopes consisting of moderate size optical mirrors with diameters $\approx$ 10m and equipped with conventional PMT based high resolution imaging cameras. With the development of novel and fast optical radiation detectors with high quantum efficiency ($\approx$ 50%) it would be possible to reduce the detection threshold to 30 GeV or below for an Imaging Atmospheric Cherenkov Telescope installed at high mountain altitudes. The MAGIC collaboration, who operate 2 17m Imaging Atmospheric Cherenkov Telescopes (refer to 2.8), claims a threshold of 25 GeV at the time of writing (Anderhub et al., 2009), (Anderhub et al., 2010). The steady energy threshold at small zenith angle (statistical maximum of accepted energies) $\approx$ 50 GeV (triggered) or $\approx$ 60 GeV (analyzed). This difference is due to pre selection and MAGIC supercuts.

Since the energy region below 30 GeV is being effectively spanned by a new generation of satellite instruments like FERMI, the gap between the spectral coverage of the space based and ground based observations has eventually disappeared.

In the following pages detailed consideration will be given to the 10m Whipple Imaging Atmospheric Cherenkov Telescope, principally as it was the instrument used during the period that the archival data was observed. Starting with the mechanics of the telescope, detail will be given *vis a vis* construction and properties. The camera will then be discussed in great detail as this being central to the success of the Whipple telescope. Following from this, in depth explanation is given to the parameterisation that brought the field of ground based observation to new levels of sensitivity and power. Finally there is discussion in some detail of the theory behind two dimensional analysis. The mathematics and programming involved in two dimensional analysis will appear in chapter 4.

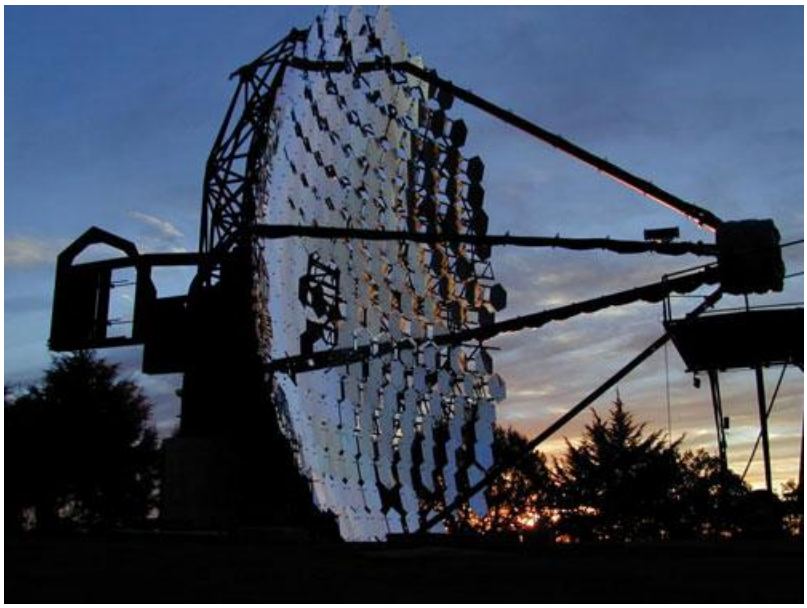

Fig 3.1: The Whipple 10m at sunset.

3.2: THE WHIPPLE 10m IMAGING ATMOSPHERIC CHERENKOV TELESCOPE

Fig 3.2: The 10m Whipple Imaging Atmospheric Cherenkov Telescope, showing clearly the tessellated mirrors based on the Davey-Cotton solar collector. Due to the solid and heavy nature of the optical support structure (OSS), it is slow to move to a new point in the sky (the slew rate).

3.2.1: Introduction

The Whipple 10 m telescope is situated at the Fred Lawrence Whipple Observatory on Mt. Hopkins in Southern Arizona (longitude 110°53.1'W, latitude 31°41.3'N, and 2320 m above sea level). It was built in 1969 and opened the door to a new era in the search for VHE gamma ray sources (Weekes et al., 1972). As the Imaging Atmospheric Cherenkov Telescope is not subject to thermal atmospheric turbulence to the same degree as standard optical telescopes (remembering that the Cherenkov light from extensive air

showers is of 3-5ns duration approx.) and that the intrinsic level of useful detail in Cherenkov showers is $\approx 0.1^{o}$, there is a slightly broader range of environments where it can be situated. Clear skies are essential with a minimum of cloud for as much of the calendar year as possible; hence Southern Arizona was chosen.

Whipple has been in continual use since its imaging systems were installed in 1982 (consisting of a 19 PMT camera). From the late 1980's and practically all of the 1990's it was generally considered to be the most sensitive of the Imaging Atmospheric Cherenkov Telescope's. A more detailed description of the instrument and the Cherenkov light imaging technique which was in use at the time of the observations can be found elsewhere (Cawley et al., 1990, Lewis, 1990, Reynolds et al., 1993).

For a decade and a half the Whipple 10 m telescope was the most sensitive single telescope, providing 7σ detection of the Crab within only 1 hr onaxis observation. This implies that 100 hrs of observation by this instrument could reveal point like gamma ray sources above 250 GeV at the flux level of 0.07 Crab. This corresponds to the energy flux, f_E, $\cong 4\times10^{-12}$ erg cm^2s^{-1}, which sounds impressive even by the standards of the satellite based gamma ray astronomy (Aharonian et al., 1997).

However a series of newer instruments have recently superseded the Whipple 10m in terms of sensitivity and reliability (Hofmann et al., 2000; Weekes et al., 2002). VERITAS is now at the time of writing the most sensitive Imaging Atmospheric Cherenkov Telescope in operation.

The telescope can be looked on as constituting two principle parts: the reflector and the detector or camera. Although the detector has undergone many changes and modifications in varied attempts to increase the sensitivity of the instrument (Fegan et al., 1983; Cawley et al., 1990; Finley et al., 2001) the reflector has remained largely unchanged.

3.2.2: Collection Area data

Opening Diameter	10 m
Focal Length	7.3 m
Radius of curvature of Dish	7.3 m
Radius of curvature of Facet-Mirror	14.6 m
No. of Facet-Mirrors	248
Reflecting Surface Area	75 m^2
Plate-Scale	12.74 cm/deg
Mount	Alt/Azimuth
Alignment Point	14.6 m

Table 3.1: General dimensions and attributes of the Whipple reflector.

3.2.3: Davies-Cotton Reflector Design

The reflector of the Whipple Observatory imaging atmospheric Cherenkov telescope is a tessellated structure, refer to Fig 3.3, which gives much greater ease and considerably lower cost to the manufacture of the reflecting surface. It consists of 248 curved hexagonal shaped mirrors, which are 61 cm from apex to apex, arranged in a hexagonal pattern of nine concentric rings which overall form a large near circular concave mirror of 10m diameter and radius of curvature 7.3 m (Cawley et al., 1990, Finley et al., 2001).

The reflector design is based on the Quartermaster solar collector by Davies & Cotton (1957) and was first used for astronomical purposes by Hanbury-Brown (1966). In the Davies-Cotton design the optical support structure or dish section is spherical in shape as already mentioned, having a radius of curvature exactly half that of the individual mirror facets that make up its tessellated structure. Each mirror facet has a radius of curvature of 14.6 m. The focal plane is located at the centre of curvature of the dish resulting in an f/0.7 system, refer to Fig 3.4. The mirrors can be manually aligned by placing an alignment instrument (a laser) on the optic axis at a position twice the dish radius of curvature from the telescope (the alignment point). Each facet is individually mounted on the optical support structure via a manually adjustable tripod mount to allow for alignment. Though well tried and tested the optical quality of the mirrors can be low compared with that of normal optical telescopes.

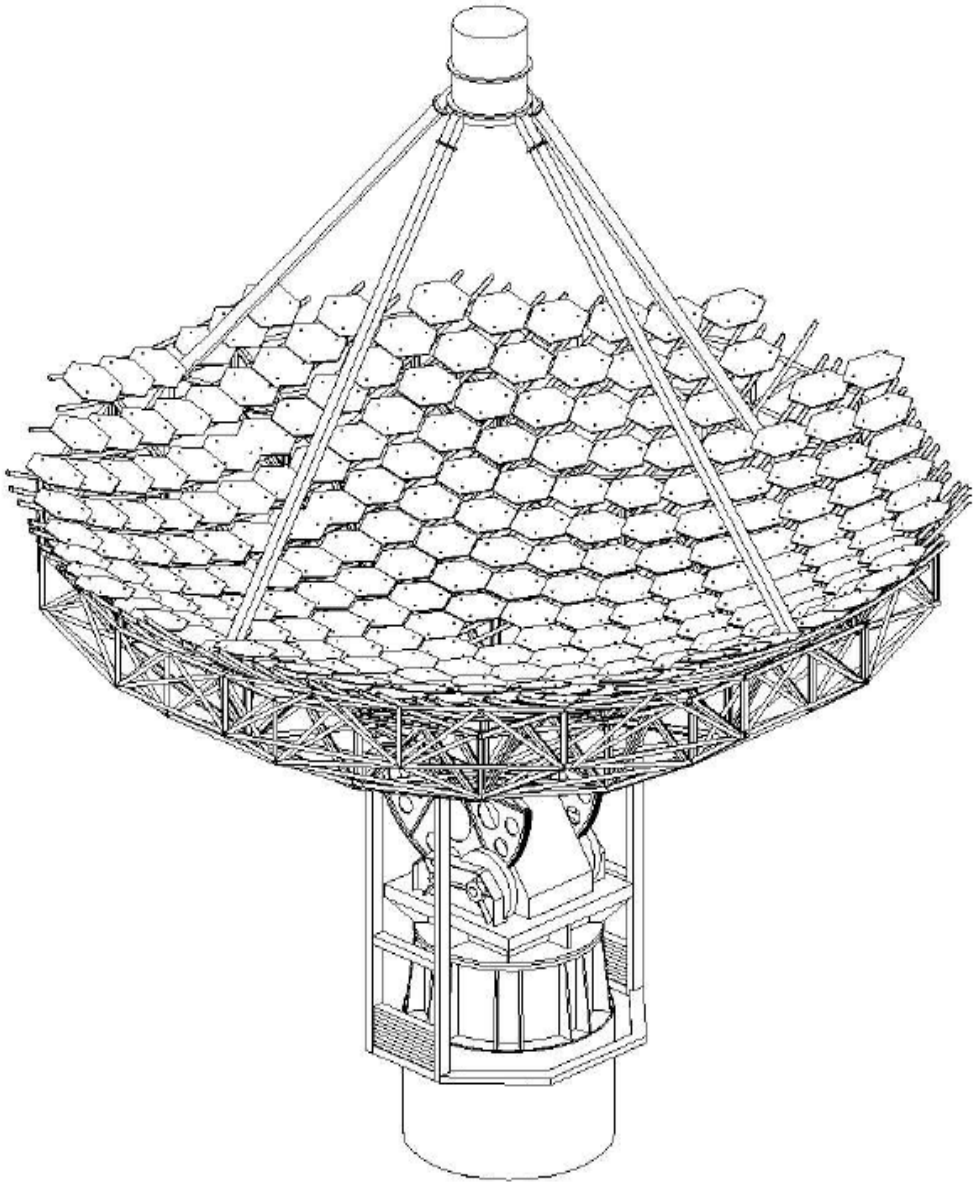

Fig 3.3: A schematic of the Whipple 10 m gamma ray telescope, showing the tessellated mirror facets, camera mounting and optical support structure.

Cherenkov light is collected by the reflecting dish and focused on a detector (an array of photomultiplier tubes) located in the focal point of the reflector. A focus box containing the camera elements is supported by quadrapod arms to hold the instrument steady in this focal plane and can be seen in Figure 3.3. The advantages of this design are many; they include rigid structure, lightweight reflective surface, identical mirrors and flexibility in realignment should the optical support structure change slightly in shape during time. Additionally the following optical properties are to be noted; offaxis aberrations are reduced and the facet alignment procedure is relatively straight

forward. With regard the offaxis properties, the Davies-Cotton design is considered superior to that of a parabolic reflector (Lewis, 1990).

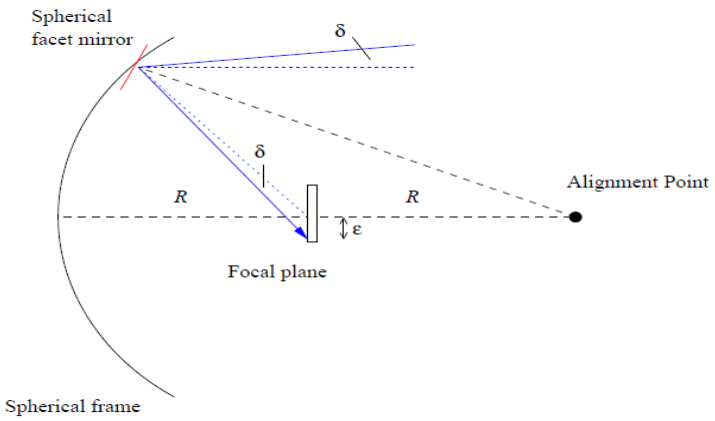

Fig 3.4: A schematic of the collection area. The Davies-Cotton reflector design has a spherical dish with radius of curvature half that of its individual mirror facets. Note the alignment point which is twice the focal length of the reflector.

This design does however have a disadvantage, it is not isochronous. Due to its spherical shape, parallel rays of light from a source reach the outer mirror facets first and, as a result, reach the focal plane before rays reflected from the inner portion of the reflector. This causes a temporal broadening of the optical signal detected by the PMT camera of the order of ≈ 6 ns, requiring a longer integration time. This longer integration time has the effect of reducing the signal to noise ratio. Nevertheless, this reduction is low in comparison to the noise contributions of the electronics when the signal is processed later in the data acquisition systems. With the more modern Cherenkov telescopes the sky brightness noise and electronic noise are about the same. A further downside of this temporal aberration is that the temporal properties of the Cherenkov light pulse cannot be investigated. Even though the isochronous characteristics of the Davies-Cotton design are undesirable, it does not constitute a serious constraint to the detection of VHE gamma rays with the telescope. The point spread function of the Whipple Observatory 10 m telescope has a Full Width Half Max (FWHM) $\approx 0.12^{o}$ onaxis for a point source during the archival epoch (Konopelko et al., 2007).

To increase the reflectivity for frequencies in the blue to ultraviolet section of the spectrum (the principle frequencies of Cherenkov light) the facets are front aluminised. As the telescope is open to the elements a recoating of the mirrors is required every three years. Figure 3.4 illustrates the average reflectivity of a sample batch of 66 mirrors over a range of wavelengths before and after recoating. The results show that it is most beneficial.

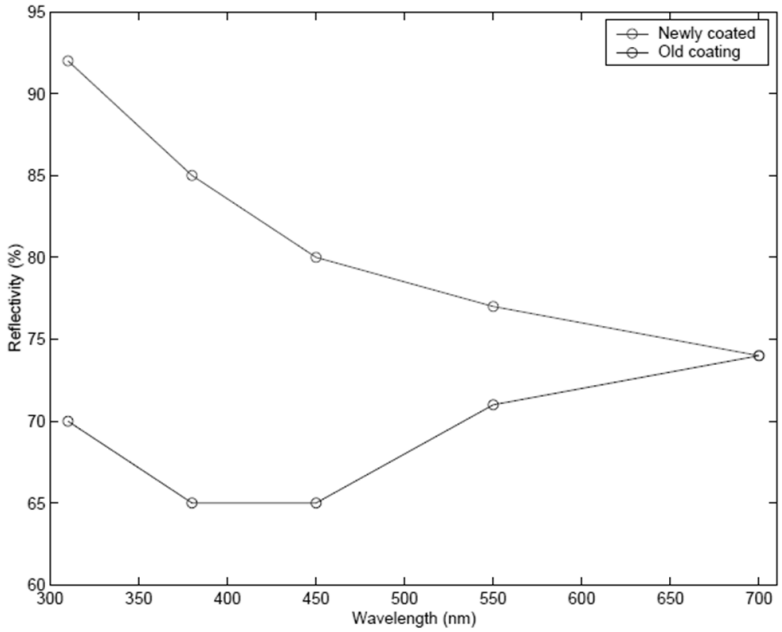

Fig 3.5: A graph of the average reflectivities of the mirrors before and after coating.

3.3: The Camera

Over the 35 years since its construction, the camera on the Whipple telescope has undergone many modifications and changes up to its current configuration. The evolution of the Whipple camera is shown in Figure 3.6.

The older array (used in this archival analysis) consisted of 91 inner PMTs of diameter 29 mm, arranged in five concentric rings around a central tube, which was surrounded by a single ring of 18 tubes of diameter 50 mm, resulting in a total field of view of 3.75°. A detailed description of the 91+18 PMT camera can be found in Cawley et al. (1990). The surrounding outer ring of 18 PMT's was replaced in August 1993 with a partial ring of 18 x 28.6 mm tubes.

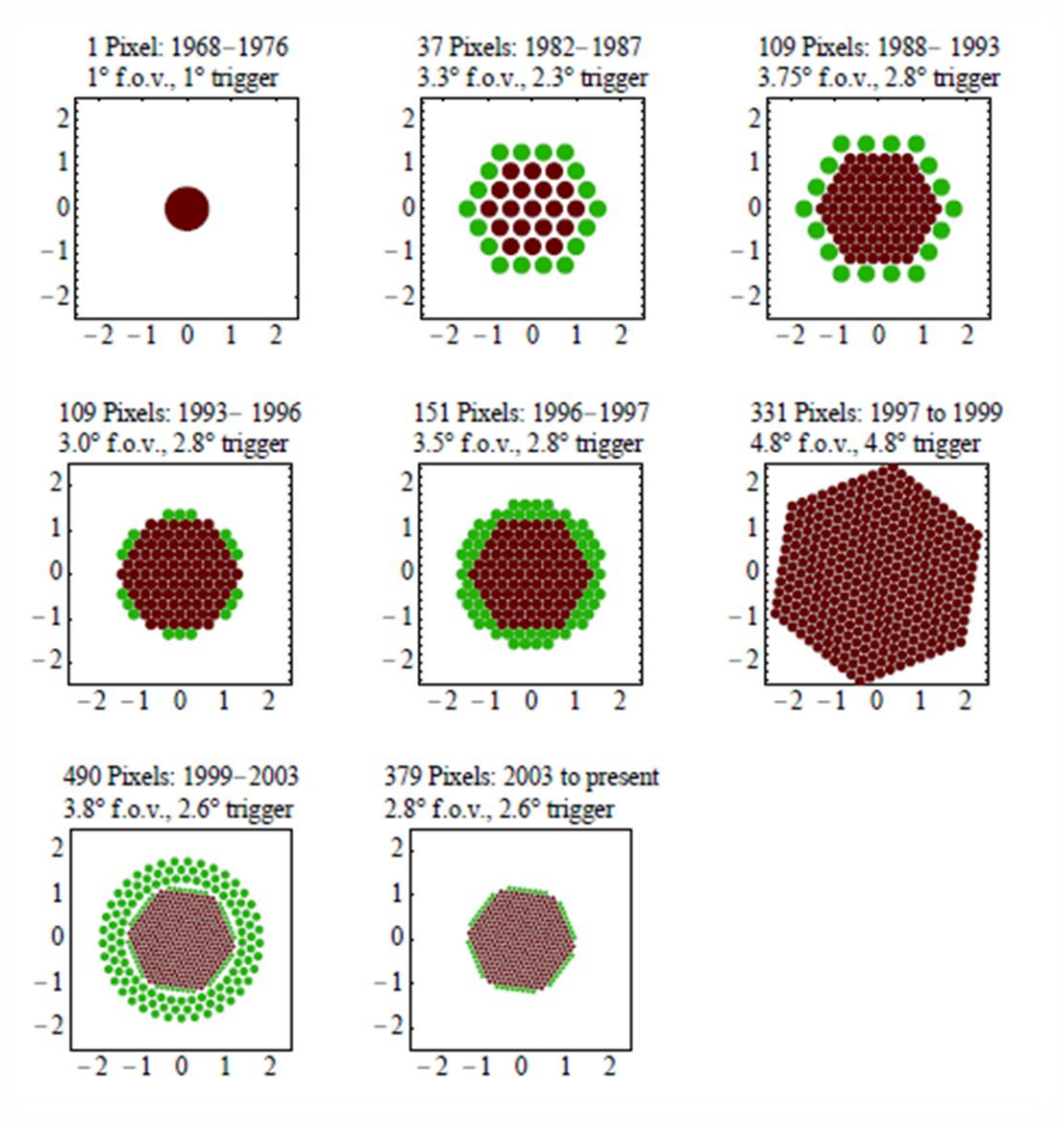

Fig 3.6: The development of the camera at Whipple. The increasing resolution due to smaller tube diameter led to greater discrimination of hadronic showers while increasing sensitivity to photon induced showers. The larger outer tubes, installed as a method of widening the field of view, have never performed satisfactorily and are out of favour with the Whipple telescope.

Fig 3.7 shows the PMT arrangement for the Whipple Imaging Atmospheric Cherenkov Telescope. All the archival data was taken with the 109 PMT camera which was in use from 1988 to 1993. The camera was programmed to triggered when two of the inner 91 tubes exceeded a threshold of approximately 40 digital counts in a 10 ns interval and the recorded analogue signal in each pixel was then amplified and converted to a digital signal (Cawley et al., 1990). The conversion factor for each digital count to photoelectrons was 1 digital count to 1.15 photoelectrons. In the late 1980's and up to

the mid 1990's, due to the expensive cost of solid state memory and other mass storage media, the data was originally recorded to ½ inch reel to reel tape and then archived on digital audio tapes. To further aid in the light collecting efficiency of the PMTs light guides, or light cones, were inserted around the 91 inner tubes. The light cones only permit the light reflected by the telescopes mirrors to enter the PMT's. This naturally reduces noise from other sources and reduces loss of light to the spaces between the PMT's (Hillas, 1997).

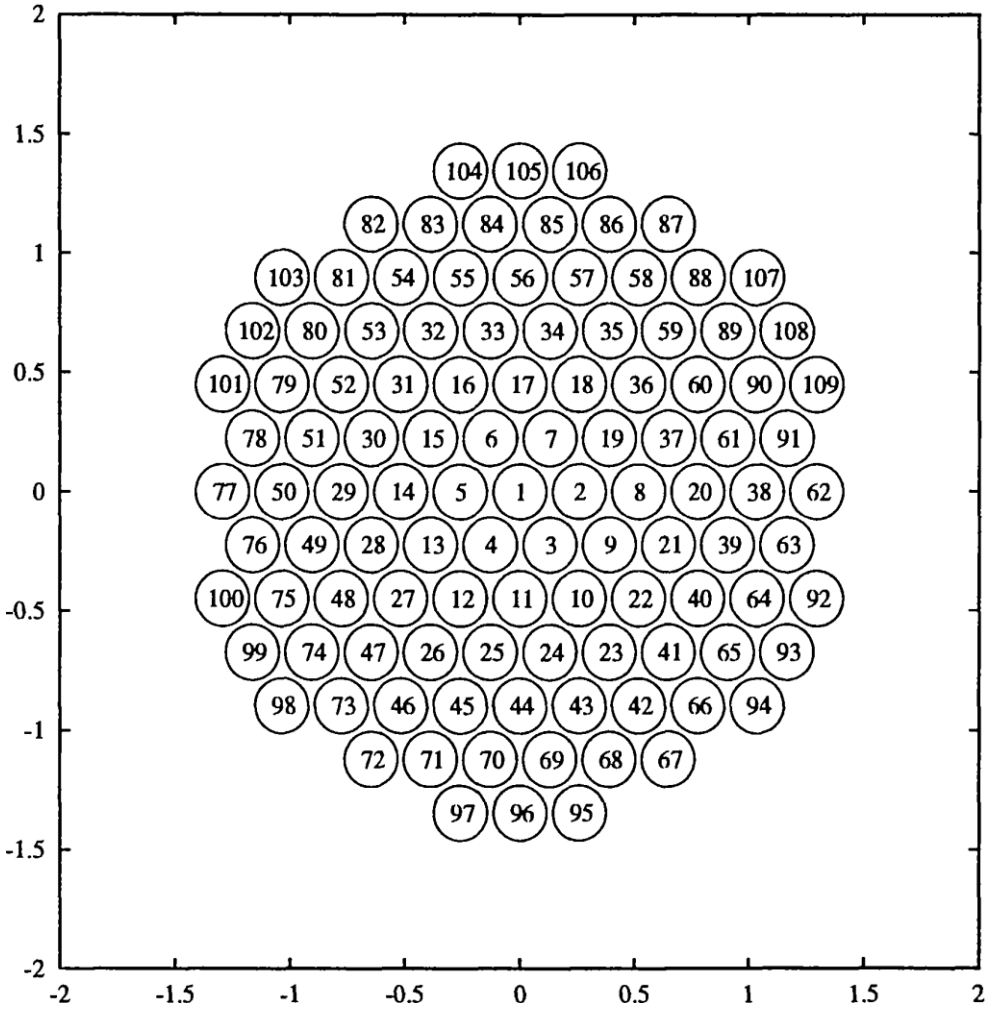

Fig 3.7: The tube numbering system. This is essential information for this analysis as the position of the centroid of the Cherenkov light image is calculated from the three maximum tube locations. The x and y axis are measurements from the centre of field of view in degrees. (Fegan et al., 1993)

The reason for the continued development of the camera can be summarised in the following way. The field of view of the camera should be at least 3^{o} in order to contain the images of showers with core position up to 150-200 m from the telescope. While

the pixels with relatively modest size of about 0.25^{o} provide an adequate quality of imaging of the air showers produced by TeV gamma rays, at low energies (E ≤ 100GeV), especially for telescopes located at high mountain altitudes (≥ 3 km a.s.l.), the pixel size should be close to 0.1^{o}. A small pixel size is preferable also for lowering the energy threshold, as well as for observations in large zenith angles (Aharonian et al., 1997). The energy threshold of the Whipple 10m Imaging Atmospheric Cherenkov Telescope contemporaneous with the archival data was ≈ 400 GeV.

The above history of camera development used in VHE gamma ray astronomy illustrates the endeavor to lower energy threshold and increase the gamma/hadron separation capability among others. This must be coupled with mirror reflectivity, aperture of telescope, stereoscopicity, etc.

3.4: Principle of the Imaging Air Cherenkov Technique

3.4.1: Outline

The data analysis flow consists of two distinct phases. The data are first processed and distributions from the raw, uncut data are then gathered and presented as diagnostics of both the condition of the instrument and the stability of the weather conditions. Each data run is visually inspected for rate stability, timing stability, and tracking consistency and is either accepted or rejected based on this first pass. Once this diagnostic pass is made, acceptable runs are further processed for scientific investigation. The considerable advancements that have been made to the imaging atmospheric Cherenkov technique during the last decade have not ousted one gamma/hadron separation parameter set from prominence. A canonical analysis method known as Supercuts (Punch et al., 1991) still stands as the most effective set of gamma ray image selection criteria for the Whipple 10 m telescope. This method utilizes both the shape and orientation information in the recorded Cherenkov light images (Fegan et al., 1997). The choice of optimal analysis cuts relies heavily on the actual configuration of the imaging camera, e.g. the angular size of PMTs, total field of view, and the level of night sky background light in each pixel (Konopelko, 2007) and various sets of cut values exist such as supercuts95 and smallcuts to name but two. These will not be discussed as they do not affect the present thesis.

The data consists of triggered events that have the decimal count of all PMT's recorded (from here on known as raw data). The decimal count is a digital conversion of the number of photons detected by each PMT. Each image is first subjected to a cleaning procedure (Fegan, 1997) that rejects pixels that are dominated by light from ever present fluctuations of the night sky background. A standard candle point source is needed to validate the cleaning and cutting processes. The Crab Nebula is believed to be a steady source of VHE gamma rays, as has been observed by the Whipple Collaboration over the past two decades (Cawley et al., 1999). To convert a given gamma ray rate to an integral flux, the rate as a fraction of the Crab Nebula rate, the photon count needs to be multiplied by $(1.05 \pm 0.24) \times 10^{-10}$ cm^{-2} s^{-1}, which represents the integral Crab Nebula flux above 350 GeV (Hillas et al., 1998).

3.4.2: Data processing

Data received from the camera is then processed following the standard Whipple analysis procedures (Reynolds et al., 1993) in which the Cherenkov light images are flat fielded, cleaned and characterized by simple image moment parameters (Hillas, 1985) now described in more detail. Before the application of shape and orientation cuts a *software trigger* cut is also applied to eliminate events close to threshold, some of which are induced by noise fluctuations. The software trigger involves cuts on the image *size* (the total number of photoelectrons recorded) and the counts in each of the brightest two tubes (max_1, max_2). A |*distance*| cut, the distance in degrees from the centre of field of view of the camera to the centroid of the Cherenkov image, is applied to eliminate images which are too close to the centre of the camera and will have poor image reconstruction and also those events which have occurred too close to the edge of the field of view and may be truncated. The parameter |*distance*| is presented as such with || for its value varies along with |*miss*| in 2 dimensional analysis, while all other parameters bar α remain constant.

For an event at the camera to be well defined and to be analysable by moment analysis, the following procedures need to be carried out on the data in its raw form; Pedestal Subtraction, Flat Fielding, Noise padding and Image cleaning. Each is examined now in detail.

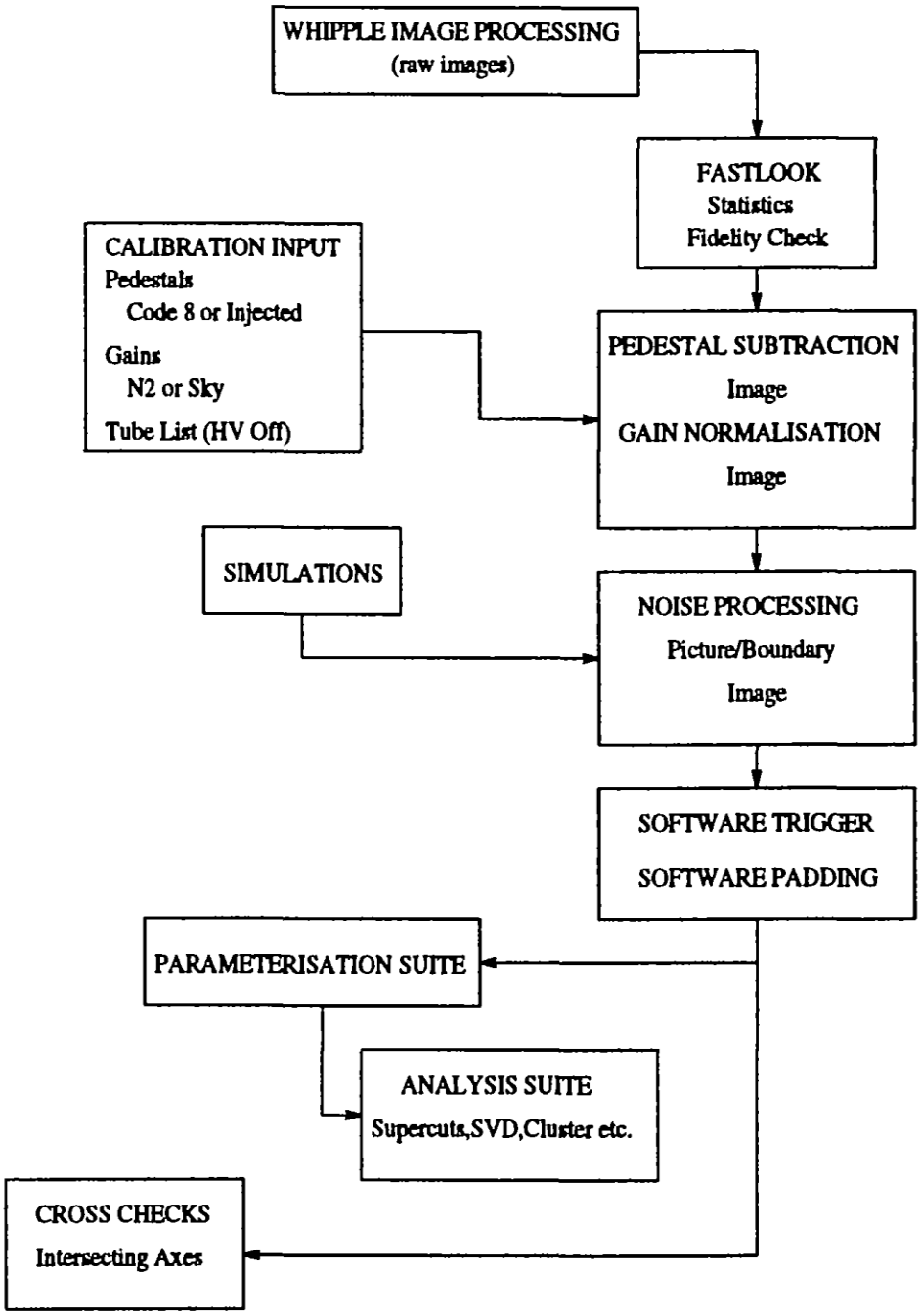

Fig 3.8: Data analysis flow diagram in use at the time the AE Aquarii archival data was recorded (Fegan, 1993). Every time that this instrument underwent some change or modification, many of the processes mentioned above had to be re optimised.

3.4.2.1: Pedestal Subtraction

The pedestal of an analogue-digital converter (ADC) is the finite value which it outputs for zero input. This is usually set at 20 digital counts so that small negative fluctuations on the signal line, due to night sky noise variations, will not generate negative values in the ADC. The pedestal for each PMT is determined by artificially triggering the camera,

thereby capturing ADC values in the absence of genuine input signals. The PMT pedestal and pedestal variance are calculated from the mean and variance of the pulse height spectrum generated from these injected events (Lessard et al., 2000).

3.4.2.2: Flat Fielding

Since each PMT has a slightly different gain, it is necessary to scale the signals recorded in each tube accordingly so PMTs with larger gains do not distort the final analysed image. This is done using a nitrogen lamp. The relative PMT gains are determined by recording a thousand images using the fast Optitron Nitrogen Arc Lamp illuminating the focal plane through a diffuser. These nitrogen pulser images are used to determine the relative gains by comparing the relative mean signals seen by each PMT.

3.4.2.3: Noise padding

During the course of an observation run the sky brightness of the ON region (the source being observed) or OFF region (the control observation) region can vary significantly. This means pedestal deviations can differ accordingly and can introduce a bias, distorting the results of the analysis procedure. To rectify this problem the noise levels must be equalised in the ON and the OFF runs. To do this artificial noise is added numerically to the data from the darker of the two sky regions. The amount that is 'padded' can be calculated by comparing the noise level for a given tube in the ON and OFF regions and padding to the level of the noise tube.

3.4.2.4: Image cleaning

Finally before parameterisation the images must be cleaned. Once the above processes are complete, what is left is an image of the signal due to the Cherenkov flash and noise due to the night sky background. Hence before analysis the night sky background element of the signal must be removed as best as possible. This is achieved by the following method of applying picture and boundary thresholds. Picture and boundary thresholds are what define the boundaries of the image and are defined as follows,

i. The picture threshold is defined as the multiple of the RMS pedestal deviation which the tube must exceed to be part of the picture.

ii. The boundary threshold is defined as the multiple which tubes adjacent to the picture must exceed to be part of the boundary.

iii. Picture and boundary thresholds are optimised and set at 4.25σ and 2.25σ respectively (Punch et al., 1991) where Nσ is the statistical significance measured in standard deviations.

The resultant images of the Cherenkov light from the air showers are parameterized according to Hillas (1985), as will be described in 3.6, and gamma ray–like images are selected using the supercuts criteria (Reynolds et al., 1993).

Changes to the hardware generally required reoptimisation of the analysis procedure. For example prior to the 1995 observing season the high voltage settings were raised to 1.4 times their previous values and discriminator levels were increased by 20%. In addition the mirror faces were recoated with reflectivity maximizing in the blue to ultraviolet region of spectrum. This reduced the energy threshold of the instrument near the zenith to $\approx$ 200 GeV. The trigger rate increased from approximately 5 events per second to 15 events per second. The reduction in energy threshold introduced two new sources of background into the data. The telescope could now be triggered by fluctuations in the night sky background or by Cherenkov light from single local muons. Therefore Supercuts 95 applies a modified image pre selection. Image sizes must exceed 400 dc and the first and second highest pixel intensities recorded in the image must be 100 dc and 80 dc respectively. The pre selection raises the effective energy threshold near the zenith to $\approx$ 300 GeV (Quinn et al., 1996).

This exemplifies why archival analysis must be preceded by ample research into the optimisations employed at the time of observation along with changes made to mirrors and electronics. Archival data analysis must first be preceded by reading archival papers of work carried out contemporaneously. It is hoped that this thesis may be a source of information regarding observations made with Imaging Atmospheric Cherenkov Telescope's during the early 1990's to some degree.

3.5: Gamma/Hadron separation

Up to this point examination has been made of the physics that produces gamma rays, mentioned in chapter 2. Attention has been given to known TeV sources and the history of gamma ray astronomy which helped unveil them. Further in this present chapter an in depth look at the telescope has been afforded, focusing on its principle characteristics and properties. Next for consideration is examination of what happens when a Cherenkov light flash impinges on the mirror and is detected by the camera. Finally, in detail, the logical process as to how this image is processed and parameterized is explained.

Refer now to Fig 3.9. As mentioned each Cherenkov light image is characterised using a moment analysis (Reynolds et al., 1993). The roughly elliptical shape of the image is described by the *length* and *width* parameters and its location, orientation and major axis asymmetry (or 'egg shape ness') within the field of view are given by the |*distance*|, *alpha* and *asymmetry* parameters, respectively. The program determines the two highest signals recorded by the PMTs (max_1 , max_2) and the amount of light in the image (*size*). Gamma ray events give rise to more compact shower images than background hadronic showers and are naturally oriented towards the putative source position, with the narrower end of the image pointing towards this position in the image plane. By making use of these differences a gamma ray signal can be extracted from the large background of hadronic showers with a background rejection rate of $\approx$ 99.7%. Along with this high hadronic rejection rate approximately half of the gamma rays are also rejected.

In 1988-89 a Crab Nebula dataset containing onaxis data was used to optimise the original gamma ray selection cuts. This resulted in the optimised gamma/hadron separation parameter value set known as supercuts. The flux sensitivity was increased by a factor of 1.75 in one season alone thanks to this new optimization set. A signal could be seen from the Crab nebula in the > 4σ level after 1 hr of observation. These values still held for the archival epoch of the data analysed in this thesis (Punch et al., 1991).

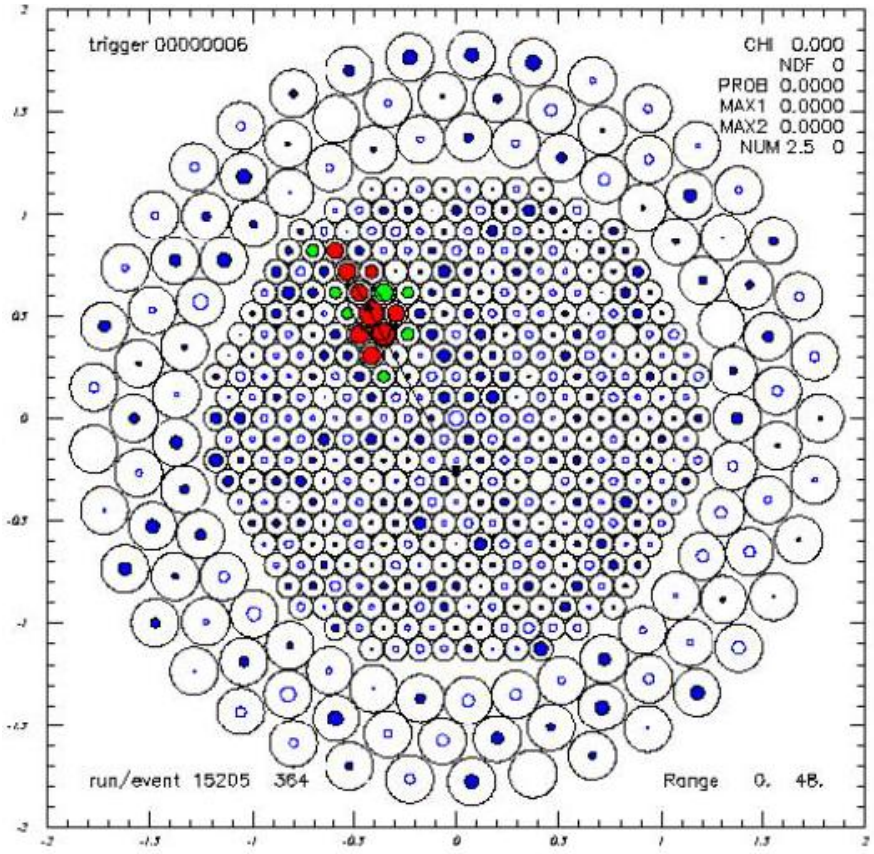

Fig 3.9: The most recent camera presently in use at Whipple

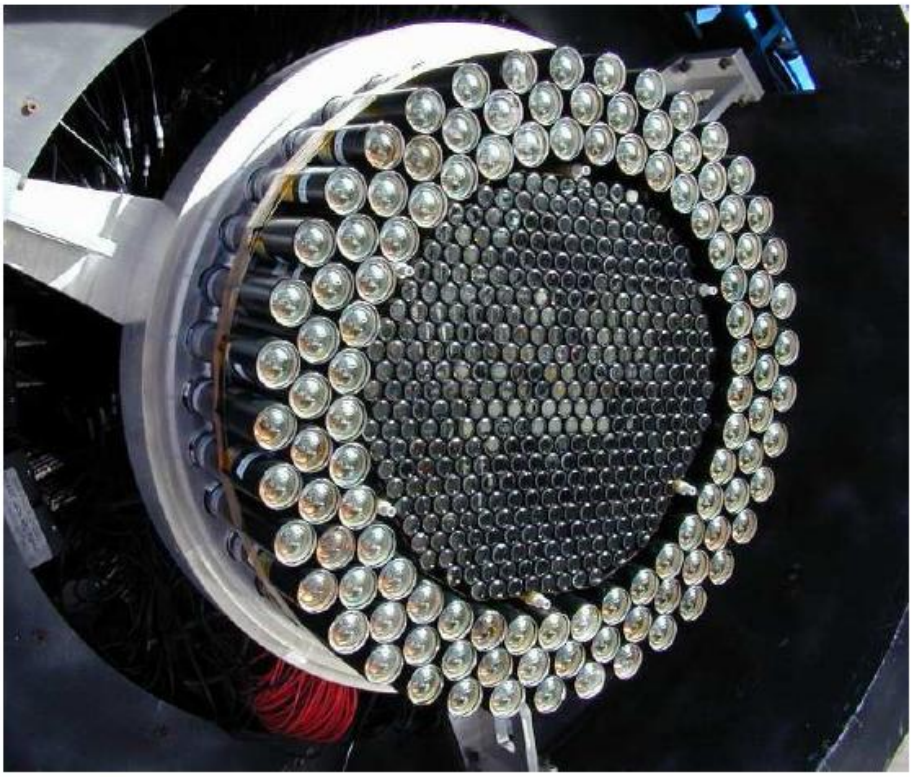

Firstly presented in Fig 3.9 is a schematic representation of all 490 PMT's. The central zone of 379 13mm PMTs is ringed by 111 25mm PMTs; a configuration implemented in 1999 to replace a lower resolution predecessor with 331 25mm PMTs which had operated since 1997. Each 13mm PMT pixel has an angular coverage of 0.12^{o}, while the typical width of a gamma ray induced Cherenkov image is $\approx 0.3^{o}$. The camera trigger condition requires 4 or more adjacent PMTs with a pulse height exceeding that of 4 photoelectrons. In this configuration the telescope is sensitive to showers from gamma rays in the energy range 100 GeV to 10 TeV, though the lower limit is rarely achieved due to zenith angle dependencies.

Obviously the tubes are packed very tightly together; these tubes each have a light cone attached to help cut out random sky noise entering the PMT and causing a spurious reading to be recorded. The photograph of the High Resolution Camera is clearly showing the 379 inner PMT's. The outer rings of the larger PMTs are no longer used.

The 4 schematic representations of triggerable events in Fig 3.10 illustrate well the mass of data that the camera delivers to be processed. With non parameterised data (the raw data) each event that triggers the camera will have 379 tube values in digital counts which are processed as outlined above. It becomes obvious when the duration of the Cherenkov flash is recalled that fast electronics are needed to deal with this large amount of data, in addition to fast memory to store the data in readiness for the next event. This field of observation would be impossible without custom programming to make intelligible all the data generated. For a correct reading of the diagrams in Fig 3.10, the size of the solid circles is proportional to the number of photons detected by each PMT.

It becomes obvious how the image events caused by cosmic rays (b) and local muons (d) can readily be rejected; they are vastly different than an image from a gamma ray (a). However the case of sky noise including low energy muon induced extensive air showers can be harder to differentiate. In fact as well as rejecting 99.7% of hadrons close to 50%

of gamma rays are also rejected. Future increases in gamma/hadron separation can hopefully decrease this later statistic.

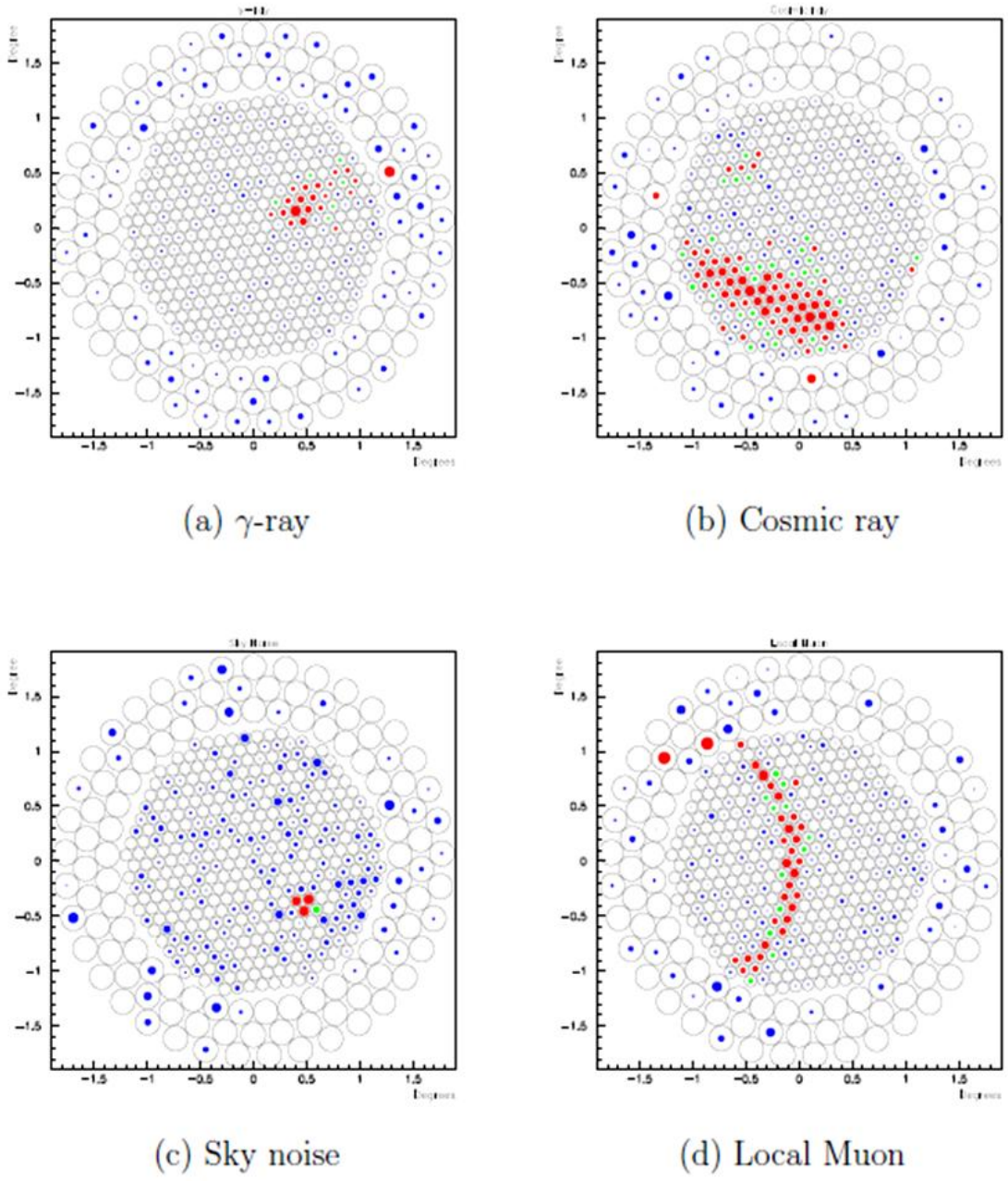

Fig 3.10: Examples of the four main types of events that can trigger the camera during an observation run; (a) a gamma ray image, (b) a cosmic ray image, (c) sky noise trigger, (d) part of a muon ring image (Dunlea, 2001).

3.6: The Image Parameterisation

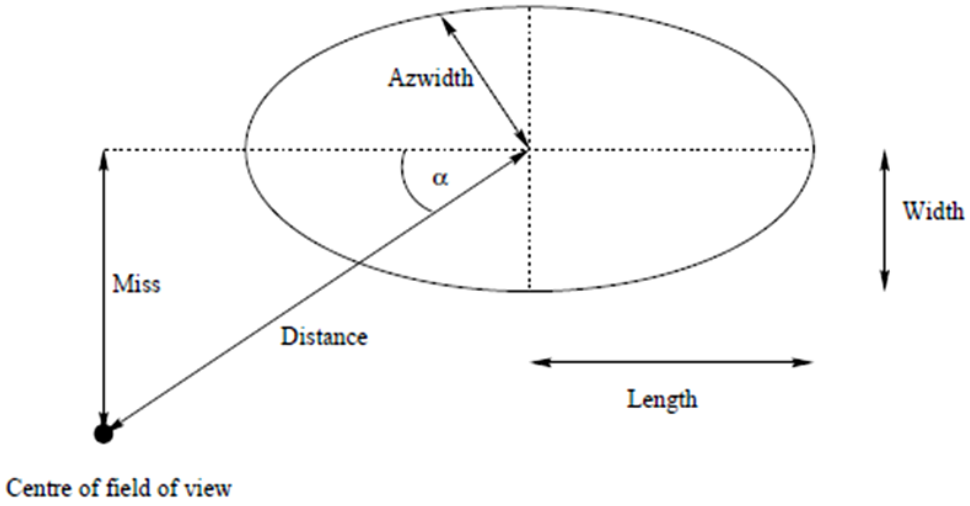

Fig 3.11: Parameters developed by the Whipple Observatory to describe the images in the focal plane of a Cherenkov telescope. The original gamma ray selection criterion was based on the azimuthal width (Azwidth) of the image. Gamma ray showers have small values of Azwidth while proton showers generally have larger values. In recent analyses, such as this one, gamma ray selection was based on the values of length, width, and alpha. Gamma ray showers have small values of alpha. The optimal parameter values for gamma/hadron separation are determined from Monte Carlo simulations (Ong, 1998)

As the shower images are mostly elliptical in nature though highly pixellated due to the camera resolution, it was found best that the parameterization of images was originally performed in terms of a moment analysis based on the recorded PMT signal values. Moments are based on the ADC counts in each PMT together with the particular tube position with respect to the centre of field of view that is given a Cartesian coordinate in degrees. The image parameters are reconstructed from the tube information. With smaller tubes and hence smaller angle of view the shower images will contain more information which could be used for further improvements in gamma/hadron separation.

The ellipse parameters can be classified as *shape parameters* which characterize the size of the image and *orientation parameters* which determine the direction of origin of the putative source.

Size:
The total integrated light content of the shower, measured in digital counts. Sometimes another parameter similar to size is used called *Conc*, that represents the degree of light concentration as determined from the ratio of the five largest pixel signals to the sum of all signals.

Length:
The RMS spread of light along the major axis of the image. This carries information of the longitudinal development of the shower.

Width:
The RMS spread of light along the minor axis of the image. This carries with it information of the lateral development of the shower.

To be sure that an event comes from a candidate source it must pass all shape cuts listed above as well as orientation cuts denoted by the angle α , calculated from below.

Distance:
The distance from the centroid of the image to the centre of the field of view of the camera. This is one of the critical parameters in 2 dimensional analysis and is denoted by |*distance*|.

Miss:
The perpendicular distance between the major axis of the image and the centre of the field of view of the camera. It's a measure of the shower orientation as already mentioned and is denoted by |*miss*| as its value varies with2 dimensional analysis.

Azwidth:
The RMS spread of light perpendicular to the line connecting the centroid of the image to the centre of the field of view. In other words it's the projection of width along a line which is perpendicular to a line joining the centre of the camera and the centre of the image and which contains the centroid. This is a measure of both the shape and orientation of the image.

Alpha:
Is the angle between the major axis of the image and the radius drawn from the centre of the camera to the centre of the image. It is related to the angle between the shower

axis and the axis of the telescope and is THE critical parameter in determining the location of a candidate VHE gamma ray source. $\alpha = \sin^{-1} \frac{|miss|}{|distance|}$.

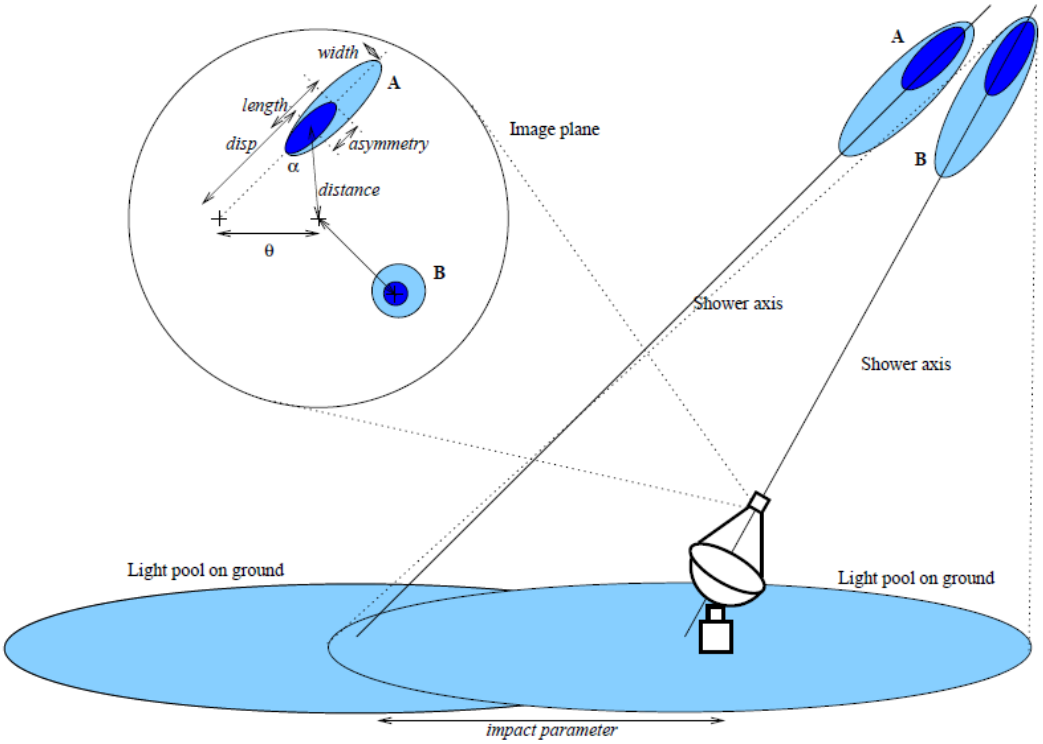

Fig 3.12: Depiction of the light produced by air showers. The image plane shows the definition of the Hillas parameters used to characterize each image and additionally shows how truncation may occur if a candidate source in the 2 dimensional analysis were too close to the edge of the light cone (Lessard et al., 2000).

3.7: Observation methods

There are slightly different analysis methods known as ON-OFF and Tracking observation modes. An ON scan consists of a period of observation (usually of 28 min duration) where the putative source is at the centre of field of view. The OFF scan consists of the region of sky which is 30 min behind in RA which is tracked over the same range of azimuth and elevation. The scan length has been set at 28 min to allow 2 min to slew between the ON and OFF regions; hence each hour of observation will yield one ON-OFF pair. For the ON-OFF observations the background is estimated from the

OFF source run which is assumed to be on a sky region which does not include a gamma ray source (Kerrick et al., 1995; Catanese et al., 1998).

Observations can also be taken in pairs of both ‘‘ON before OFF’’ and ‘‘OFF before ON’’ runs of 28 minutes duration each. This practice provided two independent background fields 30min in Right Ascension before and after the source under observation, to help minimize systematic effects due to sky brightness differences between different sky regions. One may also use padding to overcome this problem.

To further reduce any possible systematic bias in the ON source samples caused by sky brightness differences a fraction of observational data may be taken using 38 minute ‘‘ON before OFF’’ and ‘‘OFF before ON’’ runs. Thus the total data set employs four independent background fields to minimize sky brightness systematic errors (Konopelko, 2007).

Data may also be analysed using Tracking analysis. The original Tracking analysis differs from that applied to the present data in this thesis for 1 dimensional analysis of the Crab Nebula and AE Aquarii. A statistical error of 10% on the tracking ratio is now not included in the calculation of the statistical significance as a careful study showed that the results of the ON-OFF and Tracking analysis methods are in close agreement (Quinn et al., 1999).

All of the gamma ray selection criteria apart from orientation (α) are applied to the data. The background is then estimated from events that are not oriented toward the source (orientation towards the source means that is $\alpha < 15^{o}$). In this analysis background events with values of α between 20° and 65° are used. Images having values of α between 65° and 90° are discarded because of possible systematic effects due to truncation at the camera's edge. Once the number of events with orientations in the 20° to 65° range is known then the number of background events in the *signal* domain (α = 0° to 15°) can be calculated when the Tracking ratio is factored in (Quinn et al., 1999). The tracking ratio is defined as $\rho = \frac{total\ passes\ 0<\alpha<15}{total\ passes\ 20<\alpha<65}$. The Tracking ratio is determined

by using data recorded on sky fields of similar elevation which do not contain any gamma ray source.

3.7.1: Introduction of new cuts

As mentioned the standard gamma ray selection method utilized by the Whipple Collaboration is the supercuts criteria (Reynolds et al., 1993; Catanese et al., 1996); these criteria were optimized on Crab Nebula data more or less contemporaneous with AE Aquarii to give the best sensitivity for the telescope to point sources.

In an effort to remove the background of events triggered by single muons and night sky fluctuations, supercuts incorporates preselection cuts on the size and on max_1 and max_2. While the introduction of a preselection is desirable from the point of view of optimizing overall sensitivity it automatically rejects many showers below $\approx$ 400 GeV. In the context of a search for pulsed emission from the Crab pulsar, which must have a low energy cutoff to accommodate existing upper limits, this is clearly undesirable. Accordingly a modified set of cuts (Moriarty et al., 1997) developed to provide optimal sensitivity in the $\approx$ 200 GeV to $\approx$ 400 GeV regions and referred to hereafter as Smallcuts. This was used for the events that failed the Supercuts preselection criteria. The most notable difference between smallcuts and supercuts is the introduction of a cut on the length/size of an image. Such a cut is effective at discriminating partial arcs of Cherenkov light rings arising from single muons, which become the predominant background at lower energies.

When the position of the putative source is not at the centre of the field of view, or is not precisely known a different strategy must be employed in analysis. A detailed description of the technique can be found in Lessard et al. (1997). In the 1980's and 1990's 2 dimensional analysis was not routinely carried out as mentioned. VHE gamma ray sources were quite rare and the possibilities of serendipitous discovery were thought to be remote. When the raw data is present the method could use additional features of the images to provide a unique arrival direction on an event by event basis. This was not possible in the present analysis and has introduced an inaccuracy called the 'front-back ambiguity' where an event passes an orientation cut but the source may

be 180^{o} from the assumed point of origin. Firstly in trying to determine the arrival direction events are selected as gamma ray like based on their compactness. The determination of the arrival direction of the candidate gamma ray events is determined making use of the orientation, elongation and asymmetry of the image. Monte Carlo studies have shown that gamma ray images are,

i) aligned towards their source position on the sky

ii) elongated in proportion to their impact parameter on the ground and

iii) have an asymmetry or 'egg' shapeness, with their image narrower towards their point of origin.

8	0.312966	0.363	0.200	0.906	0.912	0.361	0.274	0.354	1438	57	85	56	257.	137.	114.	0 1
8	0.349993	0.419	0.193	0.759	0.804	0.397	0.203	0.289	1349	45	27	26	140.	134.	116.	0 1
8	0.645633	0.520	0.273	1.116	1.172	0.499	0.300	0.408	569	91	62	90	63.	62.	39.	0 1
8	1.134359	0.436	0.294	0.576	0.683	0.393	0.327	0.423	1280	20	37	38	277.	141.	124.	0 1
8	1.300836	0.338	0.249	0.569	1.009	0.279	0.304	0.404	699	81	53	82	135.	77.	70.	0 1
8	1.678791	0.562	0.184	0.370	0.536	0.336	0.215	0.306	728	35	58	34	87.	70.	66.	0 0
8	2.518190	0.387	0.202	0.996	1.067	0.367	0.404	0.534	727	89	90	91	149.	144.	95.	0 1
8	2.738046	0.421	0.196	0.764	0.785	0.411	0.284	0.372	2244	39	20	61	326.	312.	197.	0 1
8	2.956900	0.222	0.119	0.848	1.104	0.186	0.702	0.811	102	84	85	57	38.	33.	10.	0 1
8	3.391321	0.321	0.179	0.913	0.914	0.321	0.280	0.373	932	40	41	65	140.	120.	87.	0 1
8	3.455770	0.373	0.186	0.295	1.038	0.205	0.346	0.451	319	88	59	35	45.	33.	33.	0 1
8	3.490346	0.387	0.293	0.172	0.209	0.329	0.329	0.419	1034	13	4	14	211.	129.	93.	0 0
8	4.694411	0.420	0.305	0.619	0.621	0.419	0.316	0.387	604	25	27	24	144.	47.	43.	0 1
8	5.066766	0.245	0.233	0.716	0.787	0.243	0.307	0.419	700	28	27	49	122.	93.	79.	0 1
8	5.464752	0.606	0.246	1.020	1.080	0.570	0.294	0.355	1146	65	66	67	86.	70.	68.	0 1
8	5.844302	0.496	0.295	0.023	0.800	0.295	0.274	0.351	3471	80	53	52	649.	301.	258.	0 1
8	6.506352	0.449	0.206	0.179	0.802	0.221	0.171	0.249	534	32	54	16	47.	44.	42.	0 1
8	6.874781	0.267	0.119	0.002	0.107	0.119	0.601	0.856	58	4	19	7	19.	16.	15.	0 0
8	7.107639	0.341	0.174	0.954	0.959	0.339	0.302	0.411	1554	80	81	53	241.	229.	169.	0 1
8	7.402937	0.345	0.211	0.815	1.093	0.292	0.437	0.557	687	90	89	61	181.	82.	74.	0 1
8	8.801861	0.415	0.296	0.114	0.847	0.298	0.247	0.339	348	87	86	56	44.	42.	32.	0 1
8	8.997701	0.367	0.238	0.950	0.950	0.367	0.207	0.298	923	61	90	89	97.	95.	83.	0 1
8	9.434135	0.584	0.216	0.338	0.651	0.312	0.225	0.327	2178	86	35	58	248.	242.	223.	0 1
8	9.662872	0.280	0.188	0.500	0.901	0.220	0.386	0.508	645	81	54	32	135.	114.	79.	0 1
8	10.010997	0.252	0.153	0.531	0.801	0.201	0.405	0.492	813	28	48	47	176.	153.	71.	0 1

Table 3.2: The first 10 seconds worth of parameter values from file ae7155, an ON file from AE Aquarii.

3.7.2: The parameter files

A 10 second sample of one of the parameter files that was analysed in this thesis is presented in table 3.2. The last 2 parameters are unknown and did not become part of the analysis. The first column is a code; 8 signifies that the camera was triggered by an event while a 7 signifies it was triggered automatically with a timing marker which happens every 60 sidereal seconds. Starting from the left we have present the following parameters; code, time of event, length, width, miss, dist, azwidth, frac2 = $\frac{(\max1+\max2)}{\text{size}}$, frac3 = $\frac{(\max1+\max2+\max3)}{\text{size}}$, size, location of first maximum tube count (loc_1), location of

second maximum tube count (loc_2), location of third maximum tube count (loc_3), size of first maximum tube in digital counts (max_1), size of second maximum tube in digital counts (max_2), size of third maximum tube in digital counts (max_3). Unfortunately the raw data, un parameterised, is not available in usable form for AE Aquarii so this incomplete data set was all that was available to work with. Hence this thesis had, as one of its principle objectives development a 2 dimensional analysis based on incomplete parameterised data.

array[0] = code	array[1] = time	array[2] = length	array[3] = width
array[4] = miss	array[5] = dist	array[6] = azwidth	array[7] = frac2
array[8] = frac3	array[9] = size	array[10] = loc1	array[11] = loc2
array[12] = loc3	array[13] = max1	array[14] = max2	array[15] = max3

Table 3.3: The 16 working parameters as they appear in the analysis program for the archival data of AE Aquarii.

3.8: Two Dimensional Analysis

There are three major approaches used to perform a 2 dimensional analysis mentioned by Lessard et al. (1997 & 2001). In particular, one can generate

i. a sky map (Declination vs. Right Ascension) of uncorrelated rectangular bins with an angular size of 0.1^o x 0.1^o. One extends these bins 1^o from the centre of field of view on both axes, creating a square of 2^o x 2^o.
ii. a sky map smoothed with a circular aperture of 0.22^o radius, and
iii. a Gaussian smoothed sky map, in which each candidate gamma ray event receives a statistical weight.

The first possibility (i) was chosen for the present analysis.

The following need be kept in mind should a candidate source be detected in the extreme 'corners' of our 2^o x 2^o square. Due to truncated events (i.e., events that are not contained within the prime operating area of the camera) and the front-back ambiguity of the 2 dimensional analysis (Lessard et al., 2001), we may possibly restrict

the field of view for the analysis to a radius of 1.25^{o} from the telescope pointing direction. Hence if the centroid is more that 1.25^{o} from the centre of field of view it is rejected. This restriction minimizes systematic errors resulting from events with their light distribution close to the edge and external to the camera field of view (Konopelko, 2007). This was achieved by use of the |*distance*| parameter.

Results on the Crab Nebula indicate that the angular resolution function for the telescope using this technique is a Gaussian with a standard deviation of 0.12^{o} (Lessard et al., 1997). The software for the analysis carried out by Lessard was verified by observations in which the centre of the field of view is offset from the Crab Nebula position. A combination of Monte Carlo simulations and results on the Crab Nebula indicate that this analysis results in an energy threshold of $\approx$ 500 GeV and an effective collection area of $3.0\times10^{8}cm^{2}$ for a source at the centre of the field of view. This is reduced for offset sources.

The analysis of data from a point source offset from the centre of the field of view, involves counting the number of events which pass shape and orientation cuts within a square bin centered on the putative source location. Each bin location, representing an area of sky, must have a unique position in the analysis that corresponds with the same position for the corresponding OFF file analysis. Thus a bin with a position of (0^{o}, 1^{o}) in the ON file must have its corresponding bin location of (0^{o}, 1^{o}) in the OFF file. The sky map is produced by generating a 2 dimensional histogram of the event passes with respect to the centre of the camera. Errors in reconstructing both the image axis and point along the axis from which the gamma ray originated may possibly be accounted for by convolving the final 2 dimensional map with a Gaussian smoothing function. This however was not used in the present analysis.

3.9: Energy threshold

Though there was not a general consensus in the field of TeV gamma ray astronomy on a precise definition of the threshold energy in the early 1990's many chose to follow the prescription of Weekes (1976) and define a "traditional energy threshold" as the energy

at which the differential event rate of the telescope would be peaked for a source having a power-law spectrum with an integral index of $\alpha \approx 1.6$. The effective collection area is then defined in terms of an idealized detector with a collection area that is constant above the energy threshold, and zero below it. The effective area is taken to be the area that such an idealized detector would need to have in order to exhibit the same event triggering rate as the real detector for a source with a 1.6 integral power-law index.

For accurate estimation of energy spectrum one need avoid the region below the traditional energy threshold in determining energy spectra because of difficulties in modeling the region close to the hardware trigger. It was estimated that approximately 30% of the total number of observed events from the Crab are from gamma ray showers with primary energy below this traditional threshold. The telescope threshold as defined above is estimated to be about 500 GeV for the 1988/89 detector, while the lowest energy detected was about 200 GeV which is a conservative definition of the telescope threshold (Mohanty et al., 1998, Schubnell, 1996)

The lowest possible energy threshold is desirable in an Imaging Atmospheric Cherenkov Telescope. This is a function of elevation (and background light level) the efficiency of Cherenkov light collection and the trigger efficiency for gamma rays. There is only so much optimisation that can be carried out with a single telescope to improve its sensitivity. The operation of Imaging Atmospheric Cherenkov Telescopes in this low energy threshold (Somers et al., 1987) can partially compensate the (typical) loss in gamma ray statistics at high energies by the significant increase of the collection area when the source is observed at large zenith angles ($\geq 50^{o}$). This referred to as The Zenith Angle Dependency.

Source observations are generally taken when the source zenith angle is less than 35^{o} and are referred to as small zenith angle (SZA) observations. Observations at large zenith angles (LZA, typically 55^{o} - 70^{o}) may also be made. Increasing the zenith angle has the effect of increasing the energy threshold but inversely it is also increasing the collection area. Thus it is an excellent method to increase photon count to facilitate the

approximation of the energy spectrum at higher energies. For a detailed description of the LZA technique, see Krennrich et al., (1997).

For later periods an adjustment due to changes in mirror reflectivity and camera configuration was made by calibrating with the measured cosmic ray rate R_{cr} assuming a scaling behaviour, $R_{cr} \propto E_{th}^{-1.7}$,for the energy threshold E_{th}. An energy threshold of 400 GeV corresponds to an average event rate of about 270 min^{-1}.

Chapter 4

The Analysis Software

4.1: Analysis

All software for this analysis was developed in an Integrated Development Environment (IDE) provided as freeware by Microsoft, named Visual Studio C++2005, later updated to C++2008. This marks the analysis software developed here as unusual in relation to previous Whipple 10m analysis in two ways; one C++ was decided upon instead of C, and secondly Microsoft was chosen above Linux. The reasons are personal and not professional. C++ is a more modern and hence better supported code to write in. Secondly Microsoft provides a familiar user friendly environment that eased initial progress of this thesis.

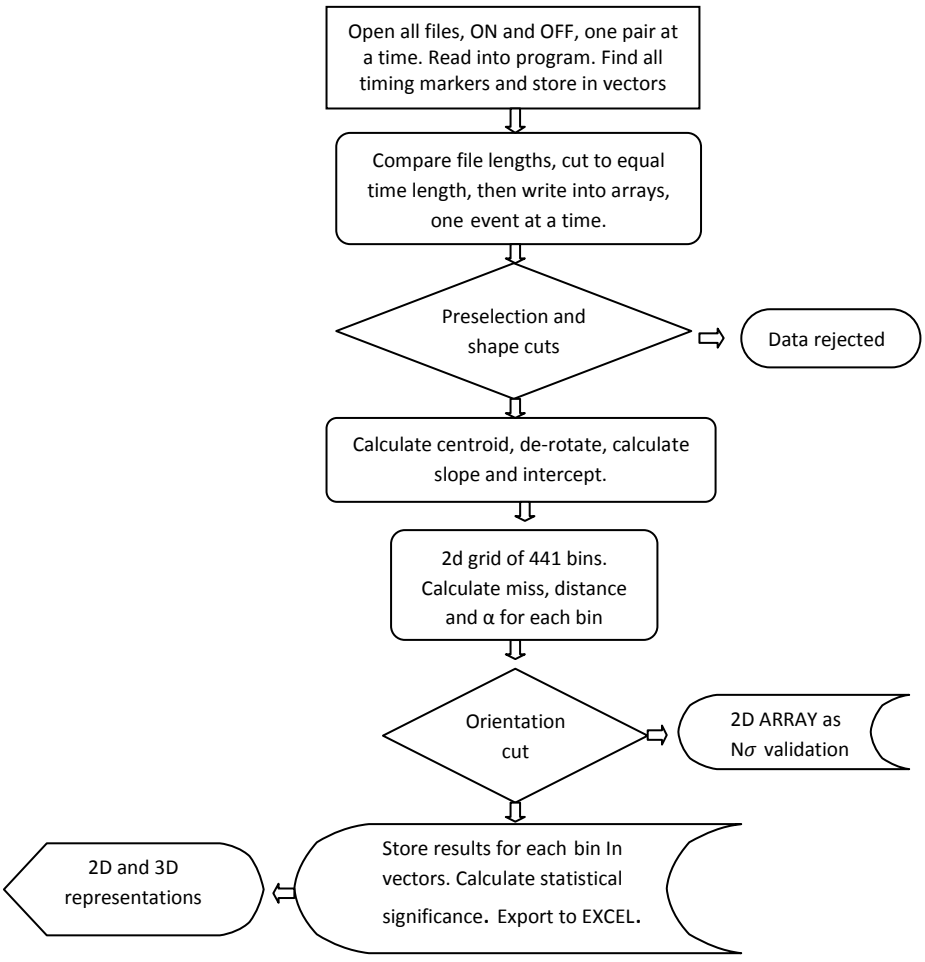

Fig 4.1: A simplified block diagram of the analysis software developed for this present thesis.

The supercuts technique was implemented for the Standard 91 +18 camera system. The pre selection cut set incorporates a software trigger requiring light intensity in at least two PMT's to exceed 40 digital counts. The frac3 filter (frac3 < 0.975) where frac3 = $\frac{(\max 1+\max 2+\max 3)}{\text{size}}$, has the effect of eliminating events which result from cosmic ray muons that sporadically pass through the camera, triggering an electron cascade within the high sensitivity sensor. Refer to Table 4.1 for the table of Supercuts used in the present analysis.

As we examine the data analysis we need recall that the appearance of this image depends upon a number of factors mentioned in the previous chapter. The nature (proton or photon) and energy of the incident progenitor, its arrival direction and it's trajectory's point of impact on the ground all determine the initial shape and orientation of the image. This image is modified by the optical point spread function of the telescope. The always present contribution of instrument noise in the PMTs and the fast switching electronics, the presence of bright stellar images in certain PMTs and by spurious signals from muons physically passing through the tubes are all part of what we term "raw data" that must be analysed (Lessard et al., 2000). The following information, Table 4.1, is required for 1 dimensional and 2 dimensional analysis; 99.7% of cosmic particles are rejected by use of these supercut limits.

normal Supercuts - standard 91+18

pre-selection cuts

$\max_1 > 40$ d.c.

$\max_2 > 40$ d.c.

$\text{frac}_3 < 0.975$

shapecuts

$0.51 < \text{distance} < 1.1$

$0.16 < \text{length} < 0.3$

$0.073 < \text{width} < 0.15$

Orientation cut

$0^o < \alpha < 15^o$

Table 4.1: The supercut limit values used in this analysis. The energy threshold for the Whipple 10m at the archival epoch was estimated to be $E_{th} \geq 500$GeV.

Next it will suffice to define some variables used in a statistical analysis of the data. For an event to register as an ON event it must satisfy all the above cut conditions in Table 4.1. All values are present in the complete parameter files bar the orientation angle, α, which is given by,

$$\alpha = sin^{-1} \frac{|miss|}{|distance|} ; \quad (4.1)$$

When an event passes all the Supercuts in addition to the orientation angle it is called an 'on event' (N_{on}) if it was observed in an ON file and an 'off event' (N_{off}) if it was observed in an OFF file. Recall that the present analysis was carried out in ON-OFF mode where ON indicates that the centre of field of view is placed 'on' the source under question and OFF indicates a background comparison region. We can thus calculate the difference for a given point in the sky as,

$$difference = (N_{on} - N_{off}) ; \quad (4.2)$$

defining a statistical quantity, σ, known as the standard deviation,

$$\sigma = \sqrt{N_{on} + N_{off}} ; \quad (4.3)$$

Finally we define the Statistical Significance, N_σ, the statistical abundance of gamma ray events at a given point in the sky measured in standard deviations, as,

$$N_\sigma = \frac{difference}{\sigma} ; \quad (4.4)$$

4.2: One Dimensional Analysis

One dimensional analysis carries out the orientation cut, $0^o < \alpha < 15^o$, at the centre of field of view only. This was by and large the sole analysis carried out during the archival epoch which consequently has left the door open for this present analysis. Firstly the

analysis will focus on reproducing the original 1 dimensional results of the Crab nebula at the centre of field of view with new software which will form part of the overall analysis package.

4.2.1: 1 dimensional ON-OFF analysis of Crab Nebula at centre of field of view

Beginning with our standard candle, the Crab nebula, an analysis program was written in C++ to detect a signal with a statistical significance of >16σ (N_σ >16) at the centre of field of view for 38 ON-OFF pairs of total duration 1083 sidereal minutes. This data was again archival and taken from the 1991-1992 season with the 109 PMT array, hence the standard supercuts were used throughout the analysis.

The coordinates of the Crab Nebula as observed in the Julian Date 1990 epoch are as follows;

Crab Nebula → RA = 5hr33min54sec; DEC = 22°00'28'' (J1990)

The table of results for all 38 ON-OFF pairs analysed using standard supercuts;

	N_{on}	N_{off}	*difference*	σ	N_σ
Raw data	189116	186338	2778	612.7	4.5
shape	5410	4739	671	100.7	6.7
orientation	15300	14117	1183	171.5	6.9
Supercuts	1471	707	764	46.7	16.37

Table 4.2: The sum of values from the 1 dimensional analysis of the Crab Nebula. This tabulation form has been found to be the most concise means of representing the data. Total file time = 61022.8 seconds.

Thus the preliminary analysis of the Crab nebula yields a signal N_σ > 16σ. In this supercut analysis all shapecut and orientation cut parameters are derived directly from the archival data, no approximations being required due to incomplete data. The alt-azimuth mounting of the Whipple 10m telescope which causes the field of view to

rotate will not be of consequence as objects at the centre of field of view do not have to be derotated to compensate for the Earths rotation.

4.2.2: 1 dimensional Tracking analysis of Crab Nebula at centre of field of view

Most gamma rays from an object at the centre of field of view will have small values of the α parameter. Hence the α distribution beyond a value (determined by optimizing the signal in a subset of the data) can be assumed to be independent of the gamma ray source and thus representative of the background level of gamma ray like events in the field of view. This α limit has been set at 20^o. Using the darkfield data, a ratio is calculated to scale the number of events between 20^o and 65^o to the number that pass the α cut which is from 0^o to 15^o. This ratio, the tracking ratio or ρ, is used to scale the 20^o to 65^o region of the alpha plot for the tracking scan so to estimate the background level of events passing all cuts. N_α is defined as the number of events in the data that pass all the gamma ray selection criteria for $0^o < \alpha < 15^o$, while $N_{control}$ is the number of such events that pass all the gamma ray selection criteria for $20^o < \alpha < 65^o$.

A Tracking analysis was carried out using the 38 ON files only for the Crab nebula centre of field of view. The 38 OFF files were utilised to calculate a value for ρ = 0.30 and $\Delta\rho$ = 0.01, described in (4.8). Subsequently we will use these ratios determined using the Crab OFF region darkfield to tracking data recorded on AE Aquarii. There follows, after the Tracking results table for the Crab nebula, the formulae used to calculate these statistical quantities.

The table of results for 38 ON files analysed in Tracking mode using standard supercuts;

	N_α	$N_{control}$	*difference*	σ	N_σ
Supercuts	1471	2198	811.6	49.64	16.35

Table 4.3: Results of Tracking analysis for Crab centre of field of view. A total of 5591 events passed the shape cuts for the entire data set. Again the total file length for this data set was 61022.8 seconds.

As can be seen from Table 4.3, this is in excellent agreement with the ON-OFF analysis. Though a 2 dimensional analysis will not be carried out on the tracking data for this

present thesis, it will be carried out some time in the future to increase the catalogue of knowledge of VHE gamma ray sources from the archival data available.

The following formulae are used to calculate the statistical significance, N_σ:

$$N_\alpha = \sum_{\alpha=0^o}^{15^o} pass_{supercut} \tag{4.5}$$

$$N_{control} = \sum_{\alpha=20^o}^{65^o} pass_{supercut} \tag{4.6}$$

$$\rho = \frac{\sum_{\alpha=0^o}^{15^o} pass_{supercut}}{\sum_{\alpha=20^o}^{65^o} pass_{supercut}} = \frac{N_\alpha}{N_{control}} \tag{4.7}$$

$$\Delta\rho = \sqrt{\frac{N_\alpha}{N_{control}^2} + \frac{N_\alpha^2}{N_{control}^3}} \tag{4.8}$$

$$difference = N_\alpha - \rho\, N_{control} \tag{4.9}$$

$$\sigma = \sqrt{N_\alpha + \rho^2 N_{control} + \Delta\rho^2 N_{control}^2} \tag{4.10}$$

$$N_\sigma = \frac{difference}{\sigma} \tag{4.11}$$

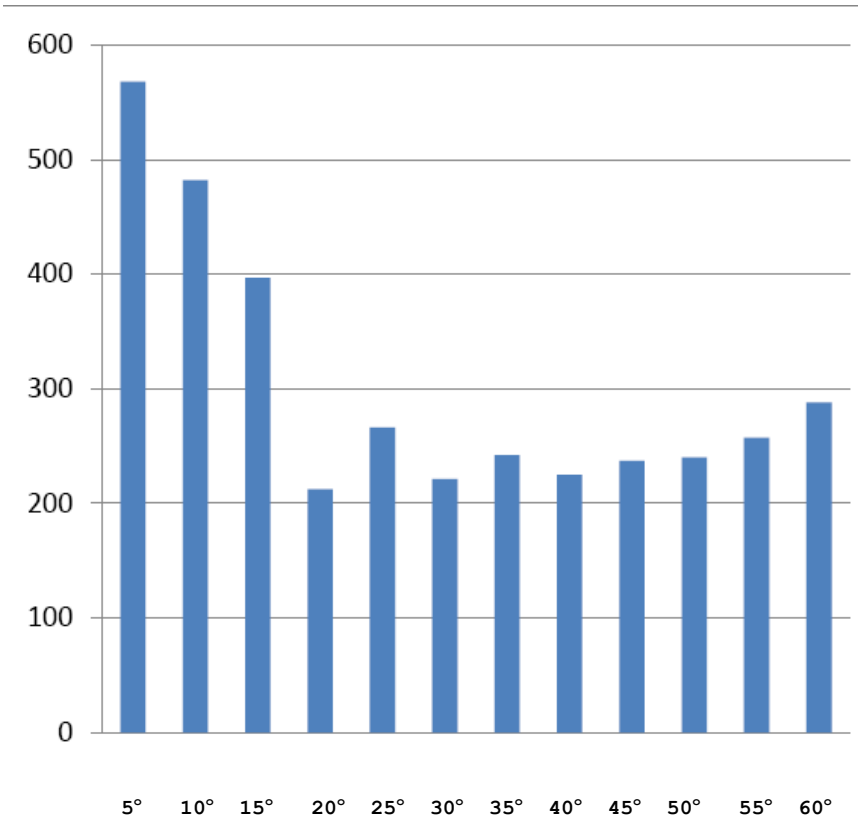

In the chart across the analysis program determines what number of orientation cuts there are in intervals of 5°, starting from 0°-5°, 5°-10°,...60°-65°. We then plot these to reveal the α plot. The actual data generated from the analysis program is listed below.

pass0_5tot = 586
pass5_10tot = 482
pass10_15tot = 397
pass20_25tot = 212
pass25_30tot = 266
pass30_35tot = 221
pass35_40tot = 242
pass40_45tot = 225
pass45_50tot = 237
pass50_55tot = 240
pass55_60tot = 257
pass60_65tot = 288

Fig 4.2: An α plot from the Tracking analysis on the Crab nebula. This was generated from the present analysis and shows the number of events which passed the shape cut and then the orientation cut at various angles of α, from 0°-5°, 5°-10° etc. A 1 dimensional analysis of a point source at the centre of field of view will yield a high α pass up to 15°.

4.2.3: AE Aquarii

Below is a table surmising all the observations taken of this cataclysmic variable (Lang et al., 1993).

Summary of TeV observations

Epoch	Hardware mode	Image analysis technique	Observation mode	Number of scans	Duration (hours)
Oct 1991	*Standard 91 + 18*	*Supercuts* *Extended Supercuts*	ON-OFF	29	13.8
Sep–Oct 1992	*Standard 91 + 18*	*Supercuts* *Extended Supercuts*	Tracking	31	22.9
Oct 1993	*Standard 109*	*Supercuts* *Extended Supercuts*	Tracking	7	4.5
July–Sep 1995	*Standard 109*	*Supercuts 95* *Extended Supercuts* *Small Events*	Tracking	26	11.9
Oct 1995	*Hybrid-UV 109*	*UV Analysis*	Tracking	34	15.6
Total				127	68.7

Table 4.4: Summary of TeV observations of AE Aquarii, part of which were examined in this thesis.

For the principle 2 dimensional analysis of this thesis only the 29 ON-OFF runs were utilised, from October 1991. However, the 38 pairs of Tracking data from September-October 1992 and October 1993 were analysed below using the same 1 dimensional analysis developed for the Crab nebula.

4.2.4: 1 dimensional ON-OFF analysis of AE Aquarii at the centre of field of view

Using this same analysis program developed for the Crab nebula the data for AE Aquarii was analysed in ON-OFF mode and the following table of values resulted from a 1 dimensional analysis;

The table of results for all 29 ON-OFF pairs analysed using standard supercuts;

	N_{on}	N_{off}	*difference*	σ	N_σ
Raw data	99881	100023	-142	447.1	-0.3
shape	5782	5956	-174	108.3	-1.6
orientation	8476	8457	19	130.1	0.15
Supercuts	897	928	-31	42.7	-0.73

Table 4.5: The sum of all supercut data from the 1 dimensional analysis of the cataclysmic variable, AE Aquarii. Total file time = 52920.04 siderial seconds.

4.2.5: 1 dimensional Tracking analysis of AE Aquarii at the centre of field of view

This analysis differed from the above tracking analysis of the Crab nebula in that there is considerable more tracking data for AE Aquarii than for the Crab nebula; 1396.06 siderial minutes (83760 siderial seconds) from 38 files recorded in 1992 and 1993. Using the following values calculated using the Crab darkfield, $\rho = 0.30$ and $\Delta\rho = 0.01$,

The table of results for 29 ON files analysed in Tracking mode using standard supercuts;

	N_{on}	N_{off}	*difference*	σ	N_σ
Supercuts	1804	5227	173.176	68.8435	2.5155

Table 4.6: The sum of data for AE Aquarii in tracking mode as calculated in this present analysis. Total time = 83760 siderial seconds.

Though seemingly large, this statistical significance is not indicative of a possible source. It is now accepted that the minimum statistical significance to define a putative source is in excess of 5 standard deviations (N_σ>5). Note that there is much more data in this run, an increase of 58% over the ON-OFF pairs. One would expect that the centre of field of view would yield a statistical significance $N_\sigma \approx 0$. This result can be interpreted as a statistical fluctuation and is unlikely to be an episodic emission, though it may warrant further investigation should the opportunity arise. One could add the ON files with the tracking files to yield a total observation time of 2278 minutes or 38 hours!

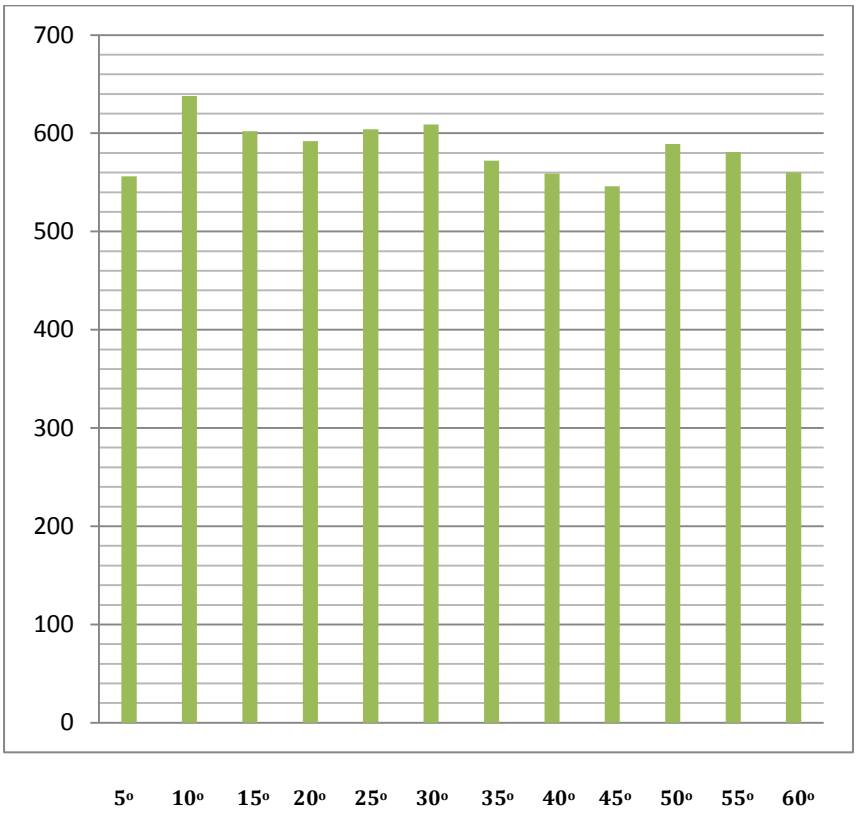

The analysis program determines what number of orientation cuts there are in intervals of 5°, starting from 0°-5°, 5°-10°,...60°-65°. We then plot these to reveal the α plot. The actual data generated from the analysis program is listed below.

```
pass0_5tot   = 556
pass5_10tot  = 638
pass10_15tot = 602
pass20_25tot = 592
pass25_30tot = 604
pass30_35tot = 609
pass35_40tot = 568
pass40_45tot = 559
pass45_50tot = 546
pass50_55tot = 589
pass55_60tot = 580
pass60_65tot = 559
```

Fig 4.3: The α plot, as seen in fig 4.2 for Ae Aquarii. This data was generated by the present analysis. Note that there is no increase in the number of orientation passes in the range 0° to 15°. This confirms the lack of a steady source at the centre of field of view.

It has been deemed useful to enter these preliminary results here as this same data set will be used in the 2 dimensional analysis to follow, for validation of the coordinate geometry element of programmimg. Additionally this data yields a visualisation of what a strong and steady TeV gamma ray point source will look like, should one be detected, in the AE Aquarii analysis. Though not of use in the present work the Tracking method of

point source detection has been validated in 1 dimensional analysis and may come into use in future analysis of archival data.

4.3: 2 dimensional analysis

So far we have searched for a signal at the centre of field of view only. Now we extend our search for possible signals in a 2^o x 2^o grid centred on the camera field of view. In 2 dimensional analysis of images recorded by the Whipple 10 m telescope during the archival epoch, all calibrated, cleaned and parameterized events in the ON and OFF data sets are analysed first with supercuts (see Table 4.1) where the shapecut was carried out. From this point all events which passed the above cut were binned in a 2 dimensional grid, mapping the sky field around the position tracked by the telescope. From these bins the orientation cut was carried out, each of the 441 bins in turn.

There are three major approaches used to perform a 2 dimensional analysis as mentioned in the previous chapter. It has been decided at the outset to employ the method of a sky map of rectangular bins with an angular size of $0.1^o \times 0.1^o$. By subtracting the number of counts in the OFF run from the corresponding number of counts in the ON run, one can calculate the excess in recorded events for each position within the camera field of view covered by the grid. A 2 dimensional plot of the statistical significance of the ON-OFF excess will give a gamma ray sky map of the 2^o x 2^o sky region. The Whipple Imaging Atmospheric Cherenkov Telescope presently has a field of view of 3.5^o, though it was 3^o at time of observations in early 1990's (Lessard et al., 2000). Thus the possibility of truncation of events, where some of the Cherenkov images fall outside the field of view for a putative source location that lies within the field of view, is somewhat lessened.

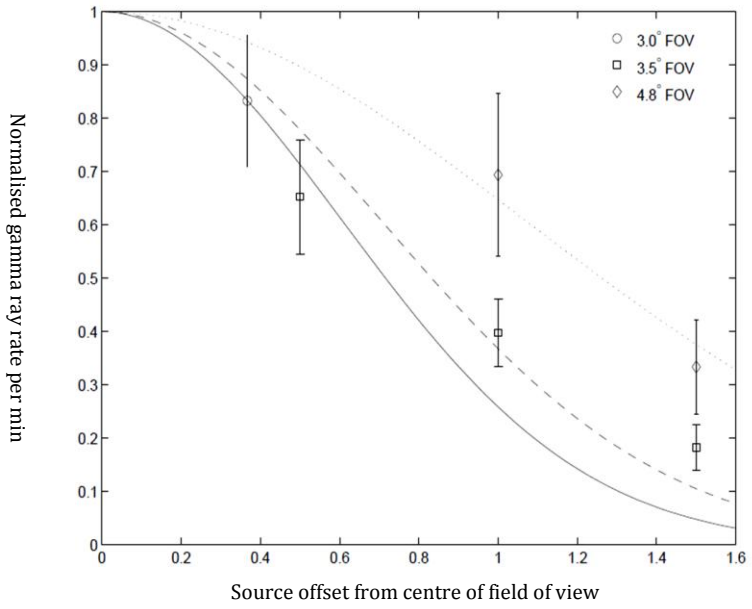

Fig 4.4: The measured gamma ray rate from the Crab Nebula normalized to the rate at the centre of the Field of View. The curves indicate the general trend of the data as the recorded statistical significance tails off significantly towards the edge of the camera (Lessard et al., 2000).

There are a number of factors which complicate and/or hinder a 2 dimensional analysis. Firstly the sensitivity of the imaging technique decreases as the putative source is displaced from the centre of field of view, along the order shown in fig 4.4. This is due to poorer optics of the reflector at the extremities and of course truncation of events. This is not necessarily a problem, but a greater number of ON-OFF pairs would be required to distinguish a source from the background noise.

As the image is not assumed to be at the centre of field of view, a parallactic correction needs to be made for all events. This takes account of the rotation of the field of view due to the alt-azimuth mounting of the telescope.

This angle, φ, is calculated by the following equation,

$$\varphi = tan^{-1}\left(\frac{-\cos(\phi)\sin(\xi)}{-\cos(\delta)\sin(\phi)+\sin(\delta)\cos(\phi)\cos(\xi)}\right) \qquad (4.12)$$

where,

$$\phi = Whipple\ Latitude,\ \ \xi = Hour\ Angle,\ \ \delta = Source\ Declination\ .$$

The hour angle, ξ, is defined as

$$\xi = RA - \mathrm{LST}_{\mathrm{event}} \; ; \tag{4.13}$$

where;

RA = Right Ascension in Julian Date 1990 (or 2010 for todays measurements),

$\mathrm{LST}_{\mathrm{event}}$ = Local Siderial Time of the event in question.

The program needs to calculate the centroid of the parameter defining ellipse for the gamma/hadron separation process utilising Hillas parameterization, listed in Table 3.3. This was not recorded in the archival data file. This is approximated by estimating the 'centre of gravity' of the maximum 3 PMT's named $\mathrm{max_i}$ at PMT number $\mathrm{loc_i}$, where i = 1 to 3. The coordinate location of each tube is known; hence the preliminary approximation of the centroid can be calculated as,

$$\mathrm{X_{cen}} = \sum_{i=1}^{3} \frac{Xmax_i Xloc_i}{Xmax_i} \tag{4.14}$$

$$\mathrm{Y_{cen}} = \sum_{i=1}^{3} \frac{\mathrm{Ymax_i Yloc_i}}{Ymax_i} \tag{4.15}$$

Knowing these coordinates one can easily estimate the slope which the radial makes with the x axis and hence the radial angle, θ. As the $|distance|$ parameter is stored from the original processed data file, a new better approximation of the centre of the ellipse can be achieved. This is the first of two approximations that need be made in our 2 dimensional analysis. Before parallactic de rotation we may calculate the following;

$$\theta = tan^{-1}\left(\frac{X_{cen}}{Y_{cen}}\right) \tag{4.16}$$

$$X'_{cen} = |distance| \cos\theta \tag{4.17}$$

$$Y'_{cen} = |distance| \sin\theta \tag{4.18}$$

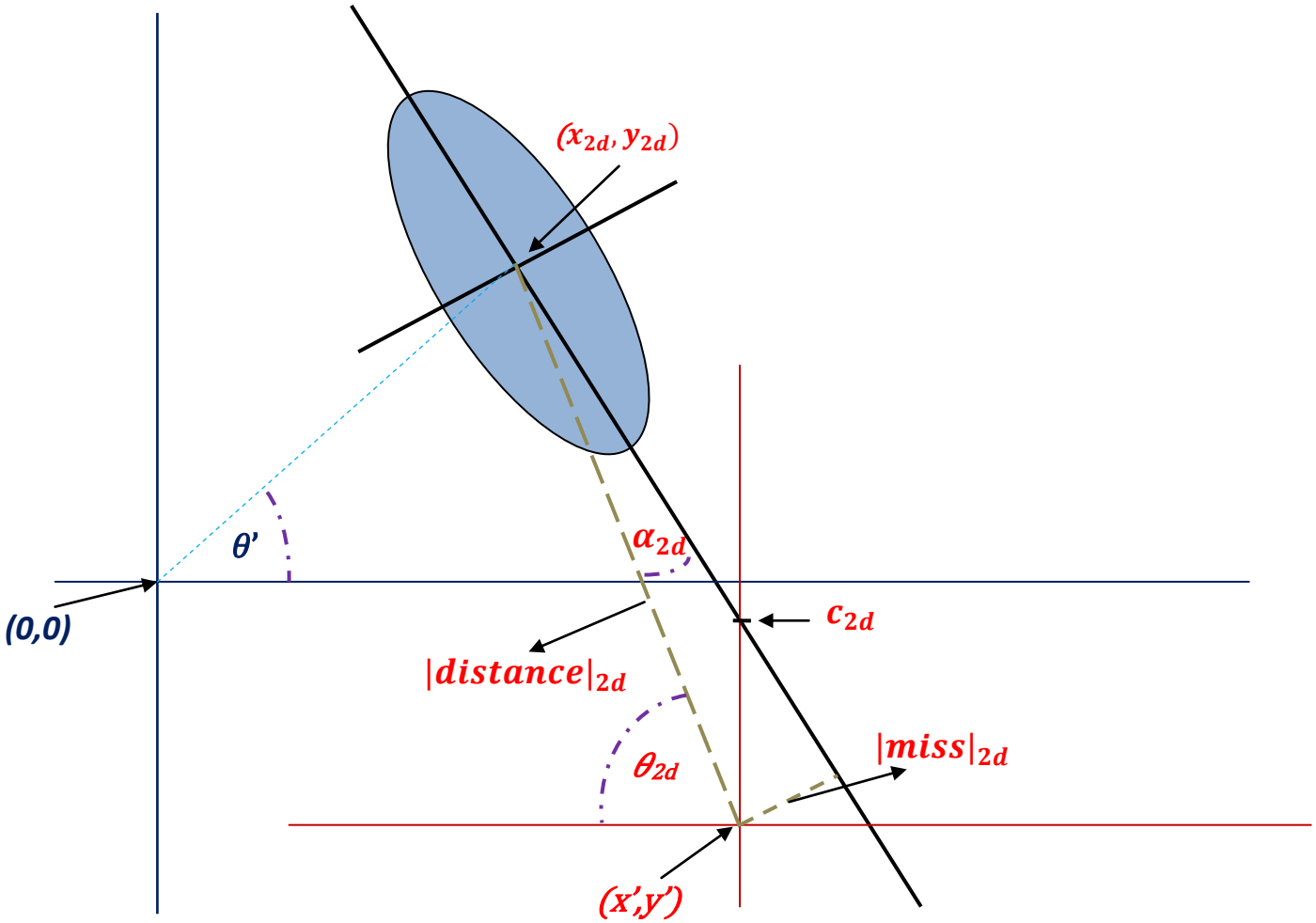

Fig 4.5: Schematic of image subjected to 2 dimensional analysis. The ellipse has already undergone parallactic de rotation. The red parameters are belonging to the 2 dimensional analysis, while the blue belong to the original centre of field of view.

Thus when an event passes the pre selection cuts and shapecuts, its centroid position is calculated with respect to the camera centre of field of view. This centroid is then de rotated by the following formulae,

$$x''_{cen} = (\cos(\varphi)\, x'_{cen} + \sin(\varphi) y'_{cen})$$
$$y''_{cen} = (\cos(\varphi)\, y'_{cen} - \sin(\varphi)\, x'_{cen}) \text{... for clockwise de rotation} \quad (4.19)$$

$$x''_{cen} = (\cos(\varphi)\, x'_{cen} - \sin(\varphi) y'_{cen})$$
$$y''_{cen} = (\sin(\varphi)\, x'_{cen} + \cos(\varphi) y'_{cen}) \text{ ... for anti clockwise de rotation} \quad (4.20)$$

$$\theta' = +/- \varphi \text{ ... clockwise or anti clockwise de rotation.} \quad (4.21)$$

Referring to Fig 4.5 the image has a centroid with respect to the centre of field of view (0,0) of (X''_{cen}, Y''_{cen}). As 2 dimensional analysis requires 441 new centre of fields of view, (x',y'), this gives us the image centroid (x_{2d}, y_{2d}) with respect to the new centre of field of view as,

$$(x_{2d}, y_{2d}) = ((x' - x''_{cen}),(y' - y''_{cen})) \quad (4.22)$$

The slope of the radial from the new axis to the centre of the image is,

$$\theta_{2d} = tan^{-1}\left(\frac{(y' - y''_{cen})}{(x' - x''_{cen})}\right) \quad (4.23)$$

The distance from the new centre of field of view (*x',y'*) to the centroid is given by,

$$|distance|_{2d} = \sqrt{(x' - x''_{cen})^2 + (y' - y''_{cen})^2} \quad (4.24)$$

The most crucial calculation is to estimate the slope of the ellipses' major axis, m_{2d}. From this one can calculate it's intercept with the y' axis, denoted by c_{2d}. This follows the standard line equation $y = mx + c$. Remember that the centre of field of view is the centre of a Cartesian coordinate grid, (0,0); all coordinates are in relation to the centre of field of view. It is in the calculation of slope and intercept that we run into a difficulty. The parameter values for |*miss*| and |*distance*| are always given as positive; they are the given lengths of particular line segments. If these parameters were given an arbitrary sign it would have facilitated the accuracy of this analysis. This is because all 4 quadrants of the Cartesian grid are used, hence some intercepts will lie below the (0,0) point. It was found necessary to approximate the slope of the major axis by fitting a line to the 3 maximum tubes by a similar process as described to calculate the centroid.

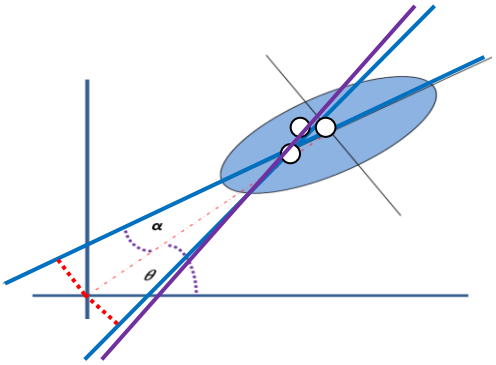

Fig 4.6: Simple graph showing how the slope of the semi major axis is calculated. The red dotted lines represents the |miss|, which are of equal length. The 3 white circles are the 3 max tubes. The purple line represents the approximation of slope from the 3 max tubes.

4.3.1: Original work in 2 dimensional analysis for this thesis

Our calculation is dependent on which of the 4 quadrants the centroid falls in. Unfortunately the estimation of slope from the 3 max tubes, $m_{max,}$ was not always an accurate estimation of the 'sign' of the $|miss|$ value. This was our second unavoidable approximation. There follows a table of calculated values for slope approximation using the 3 max tubes, Table 4.7, from the partial parameter set denoted by subscript 'ap' (for approximation). The known values are given for the full parameter set denoted by subscript 'cp' (for complete parameter set).

Refering to Table 4.7, a selection of events was taken from the beginning, middle and end of a Crab offset file, Co5461, to allow for varying degrees of parallactic correction. Two separate programs were used to calculate the mentioned parameters. Notice the discrepancy in slope, m_{cp} vs. m_{ap}, at the following times; 807, 830, 865, 869, 1326, 1334, 1347. The calculation of slope approximation is roughly 90% accurate in determining if the major axis intersects the y' axis above or below the (x',y') origin, refer to Fig 4.6. From the estimation of slope from the max tubes, m_{max}, we can determine to some accuracy which of the following formulae to use,

$$m_{2d} = \theta_{2d} + \alpha_{2d} \qquad (4.28)$$

-or-

$$m_{2d} = \theta_{2d} - \alpha_{2d} \qquad (4.29)$$

time	x_{cp}	x_{ap}	y_{cp}	y_{ap}	m_{cp}	m_{ap}	c_{cp}	c_{ap}
42.302	-0.3815	-0.3595	0.4657	-0.48287	-1.3223	-0.42936	-0.95822	0.6295
53.325	1.0368	1.0458	-0.2442	-0.2012	-1.0987	-1.1936	0.94784	0.9933
53.846	0.596	0.62878	1.034	1.0138	9.8348	14.363	-5.1701	-7.5263
58.018	0.7068	0.73538	0.8403	0.81536	-4.3615	-3.7499	4.0228	3.4907
65.99	0.0637	0.051306	-0.2533	-0.25591	1.4082	1.5714	-0.32816	-0.3534
70.18	0.4688	0.48272	0.9691	0.96276	0.4383	0.4552	0.75118	0.7557
77.811	-0.4199	-0.41094	0.8724	0.87644	-0.19061	-0.1798	0.79812	0.7969
79.875	0.7547	0.7328	0.4099	0.4482	-2.4922	-1.2805	2.2745	1.3763
801.46	-0.693	-0.70616	0.5066	0.48734	3.5425	3.2128	2.9889	2.7331
807.36	0.779	0.77741	0.3887	0.39278	-0.091523	1.6384	0.46393	-0.8876
816.39	0.5131	0.53474	0.8974	0.88499	-0.18358	-0.15942	0.98316	0.9792
824.72	0.6728	0.64565	0.9353	0.95406	-0.88917	-0.53136	1.5282	1.2928
829.54	0.8126	0.81298	-0.0092	-0.005636	0.18056	0.17672	-0.15243	-0.1528
830.7	0.2276	0.22548	0.2661	0.26769	0.26128	10.938	0.20878	-2.2233
860.28	-0.0186	-0.01716	0.8032	0.80282	1.8364	1.8495	0.83433	0.8376
865.04	-0.4737	-0.49185	0.1693	0.10531	-3.341	0.89044	-1.538	0.5911
869.5	0.7249	0.76179	0.852	0.81965	-6.9332	-0.026486	6.1013	0.8712
874.03	0.6399	0.64571	-0.6899	-0.6845	-0.94502	-0.96062	-0.0743	-0.0752
885.6	0.5858	0.60682	0.501	0.47561	0.22923	2.2154	0.33651	-0.7968
1295.1	0.5795	0.56626	0.9077	0.91612	-0.76023	-0.7767	1.3466	1.3578
1326.2	-1.0186	-1.0181	-0.0735	0.076586	-2.7168	2.6863	-2.6894	2.6628
1327.7	0.1853	0.19371	-0.0576	-0.010555	-0.008025	-0.35942	-0.009	0.009
1334.4	0.6214	0.61767	0.1032	0.12404	-0.71097	1.4965	0.56318	-0.8267
1340.8	0.0307	-0.02463	0.033	-0.037661	0.9217	1.8013	-0.01496	-0.0223
1347	0.445	0.42374	0.9851	0.99449	-1.0976	0.0058427	1.4596	0.9825
1350	0.3646	0.39513	0.9717	0.95985	2.9308	3.2611	-0.19819	-0.2173
1351.2	-0.3689	-0.3589	0.7443	0.7495	0.71951	0.29032	1.0077	0.8514
1363.6	-0.5087	-0.4265	0.9775	1.0161	-0.19111	1.8119	0.93461	1.8992
1372.5	0.8546	0.85541	0.5504	0.55006	-1.9672	-1.8968	2.2328	2.1714
1388.4	-0.3582	-0.33702	0.5681	0.58138	0.79196	0.44891	0.84829	0.7289
1392.8	0.4333	0.49215	-0.9166	-0.88656	-1.0739	-1.2257	-0.35804	-0.3855

Table 4.7: A cross section of events from co5461 showing the centroid (x,y) and slope (m) and intercept (c) calculated from the 'cp' complete parameter set and the centroid (x,y) and slope (m) and intercept (c) calculated from the 'ap' approximate parameter set.

This slope must then be de rotated by the parallactic angle before it can be incorporated into the 2 dimensional analysis, a simple process of adding the paralactic angle to the slope angle.

The intercept, c_{2d}, can easily be determined by solving the equation of the line (major axis) seen in formula (4.25). With these parameters we are ready to begin the analysis on a bin by bin basis in our 2^o x 2^o grid. Thus intercept of the major axis of the image may now be calculated in relation to the new y' axis through the new centre of field of view of (x',y') by,

$$c_{2d} = (y' - y''_{cen}) - m_{2d}(x' - x''_{cen}) \quad (4.25)$$

The shortest distance from the major axis to the new centre of field of view is given by the following formula,

$$|miss|_{2d} = \frac{m_{2d}x' - y' + c_{2d}}{\sqrt{m_{2d}{}^2 + 1}} \quad (4.26)$$

Thus the new orientation angle for the 2 dimensional supercut is,

$$\alpha_{2d} = sin^{-1}\left(\frac{|miss|_{2d}}{|distance|_{2d}}\right) \quad (4.27)$$

4.4: Validation of the software

Due to the many steps involved in producing an image from the parameter files given, a validation run is necessary before carrying out our analysis. Some archival data has been retrieved from digital audio tape of observations made in 1988-1989 of the Crab Nebula offset by 1^{o}. Only 5hrs of data was retrieved yet it was sufficient to verify the software. The raw data was used to generate a parameter file of the same type as the AE Aquarii parameter files, with $loc_{1\text{-}3}$ and $max_{1\text{-}3}$ in addition to a second set of data where the centroid, slope and intercept were given in parameter form.

The Software had to ensure each ON-OFF pair had both files of equal length, then check each event for shapecuts. If the event passes shapecuts the program then determines the centroid, derotates it by the parallactic angle and the new slope and intercept are then determined. With these parameters the 2 dimensional analysis is carried out as stated previously.

As stated 2 types of parameter files were run; one where the centroid and slope are given and the other where they are approximated. Both results are displayed in Fig 4.7 and Fig 4.8. This approximation run was necessary as a complete set of raw data does not exist for AE Aquarii from the archival epoch.

On the following pages, Fig 4.7 and Fig 4.8, we see 2D (b) and 3D (a) representations of 2 sets of Crab data, calculated with the 2 dimensional analysis software written for this thesis. Microsoft EXCEL was used to graphically represent the data and to calculate the FWHM value (c). For visualisation we treat 3 dimensional space as 2 dimensional, that is Right Ascension and Declination are the x-axis and y-axis respectivly. The z-axis is the statistical significance of gamma ray events with an energy threshold, E_{th}, $>$ 500 GeV.

First the 2 dimensional analysis of the Crab centre of field of view data was carried out with the complete parameter set, refer to Fig 4.7. Compare this to the 2 dimensional analysis of the Crab centre of field of view data carried out with the partial parameter set, $loc_{1\text{-}3}$ and $max_{1\text{-}3}$, refer to Fig 4.8 It is to be noted how the PSF differs.

(a)

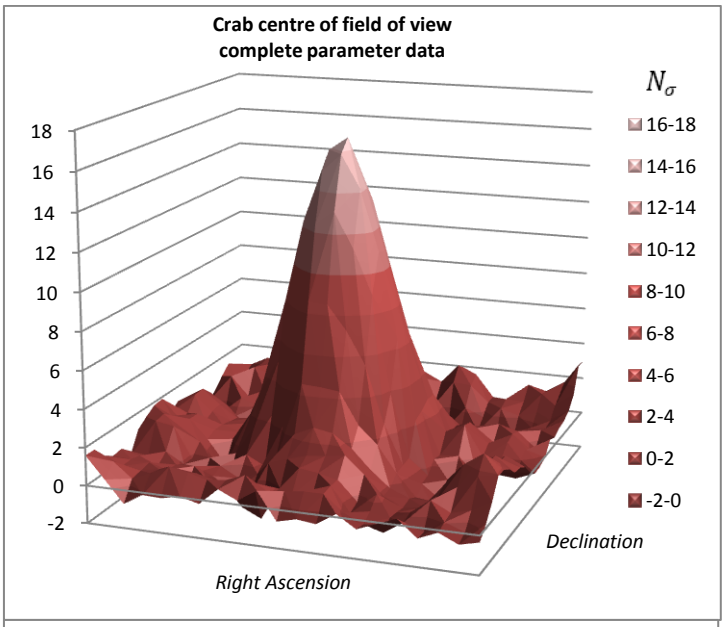

(b)

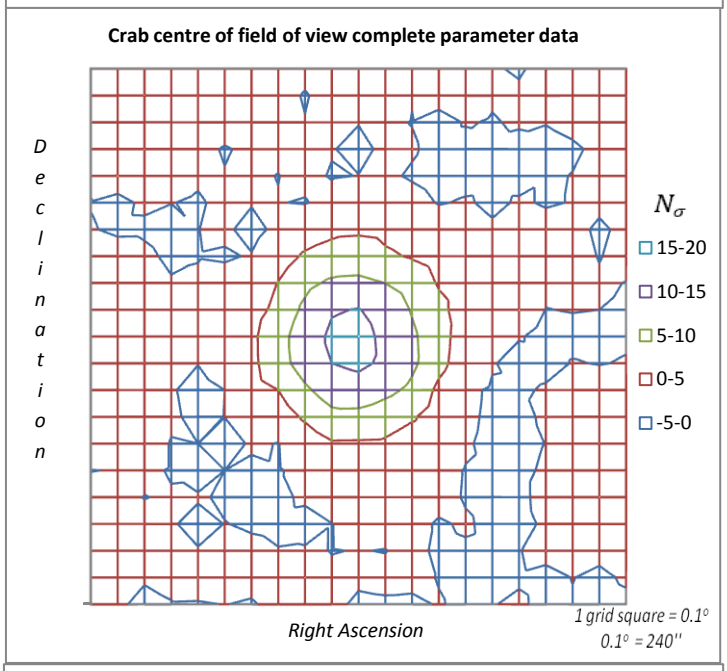

(c)

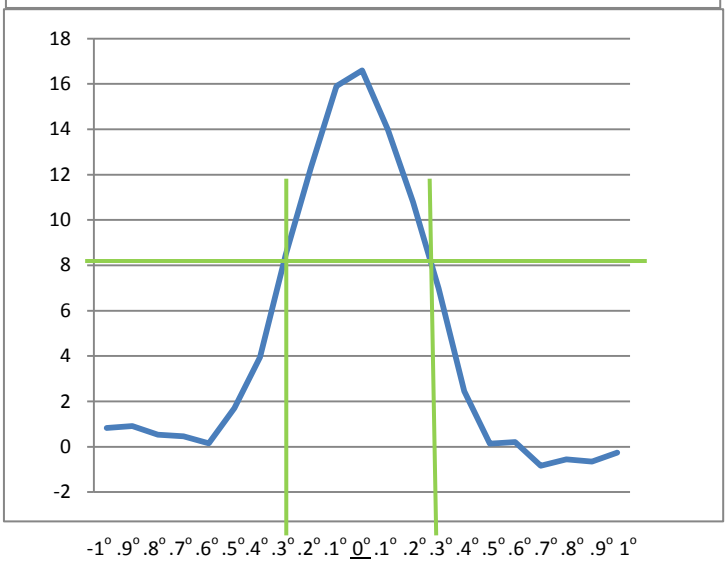

Fig 4.7: 2 dimensional analysis of the on-axis Crab complete parameter data set.

(a)

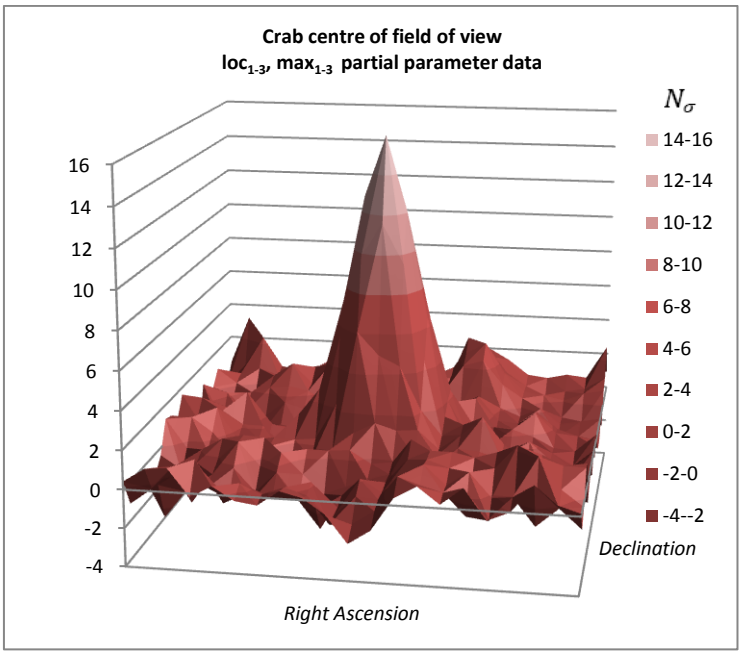

(b)

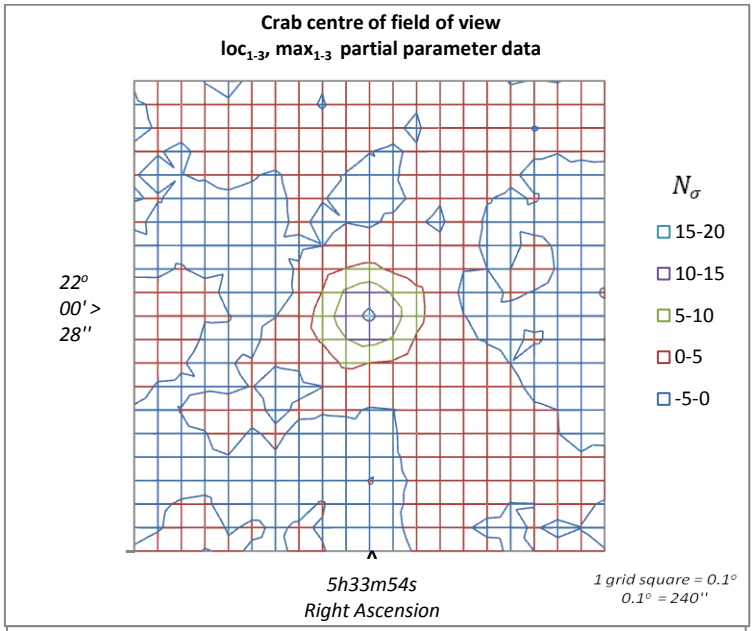

(c)

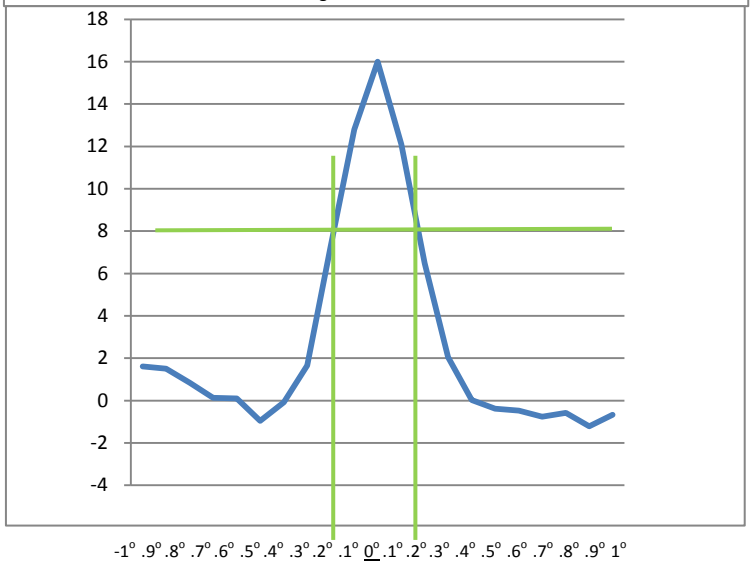

Fig 4.8: 2 dimensional analysis of the on-axis Crab partial parameter data set.

The peak statistical significance for the 2 dimensional analysis of the complete parameter set, comprising the image centroid, slope and intercept all calculated from all tube values (the raw data set) is 16.6σ. The corresponding peak statistical significance for the 2 dimensional analysis of the partial parameter set (denoted by 'ap' in Table 4.7), comprising the image centroid, slope and intercept all approximated from the 3 maximum tube values is 16.0σ. Though all analysis was caried out at the centre of field of view there was still a minimal difference in statistical significance of 3.6% due to the approximations made.

From the graphs a number of features may be noted. Firstly the point spread function of the image (PSF) is clearly symmetrical about the point source; should there be an irregular PSF about the centre that might indicate an extended source rather than a point. We are observing the gamma ray point spread function as opposed to the optical point spread function. From Fig 4.7 and Fig 4.8, we can calculate the FWHM directly from EXCEL and seen visually with the EXEL plot (c). For the Crab complete parameter set, the FWHM = 0.55^{o} while for the Crab partial data set the FWHM = 0.35^{o}.

4.5: Offaxis validation

Next the offset data is analysed in our validation run. This is the critical test for the present analysis for here each event must be de rotated by the parallactic angle before the 2 dimensional analysis is carried out. Firstly the Crab complete parameter files with the centroid, slope and intercept given are analysed and plotted. Then the Crab partial parameter files with $loc_{1\text{-}3}$ and $max_{1\text{-}3}$ are analysed, as can be seen in Fig 4.9 and Fig 4.10.

From various runs of the analysis program the following becomes evident; we notice a shift in the source position estimation; the parameter files with $loc_{1\text{-}3}$ and $max_{1\text{-}3}$ are shifted -0.2^{o} along the horizontal (RA) axis. Additionally we notice that these files are presenting less than 20% of the statistical significance than the files which have the centroid position given. The shift in RA has been noted for some time in 2 dimensional analysis though the nature of the cause remains unknown.

The RA for this validation remained the same as the centre of field of view. The DEC is increased by 1^{o}, thus we feed the following coordinates into the parallactic correction formula;

centre of field of view → RA = 5hr33min54sec; DEC = 23^{o}00'28'' (J1990)

The contour map for the complete parameter data analysis showing the point source to be at (-0.12, -1) corresponds to a Right Ascension = 5h29m06s, refer to Fig 4.9(b). The statistical significance for 5 ½ hrs of observation yields 6.12σ and the FWHM = 0.52^{o}. The corresponding contour map for the partial parameter data analysis showing the point source to be at (-0.28, -1) corresponds to a Right Ascension = 5h22m42s, refer to Fig 4.10(b). The statistical significance yields 4.93σ and the FWHM = 0.56^{o}.

(a)

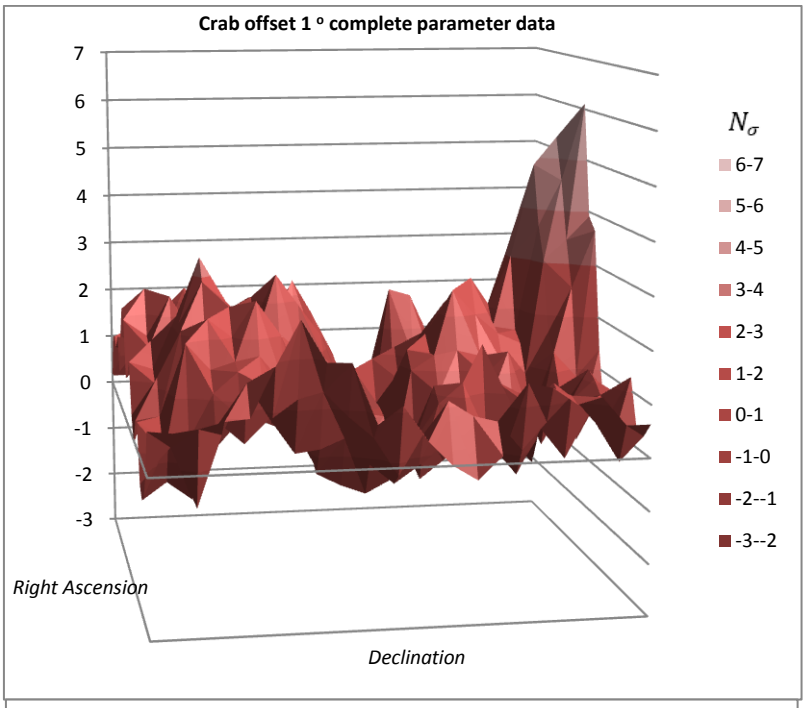

(b)

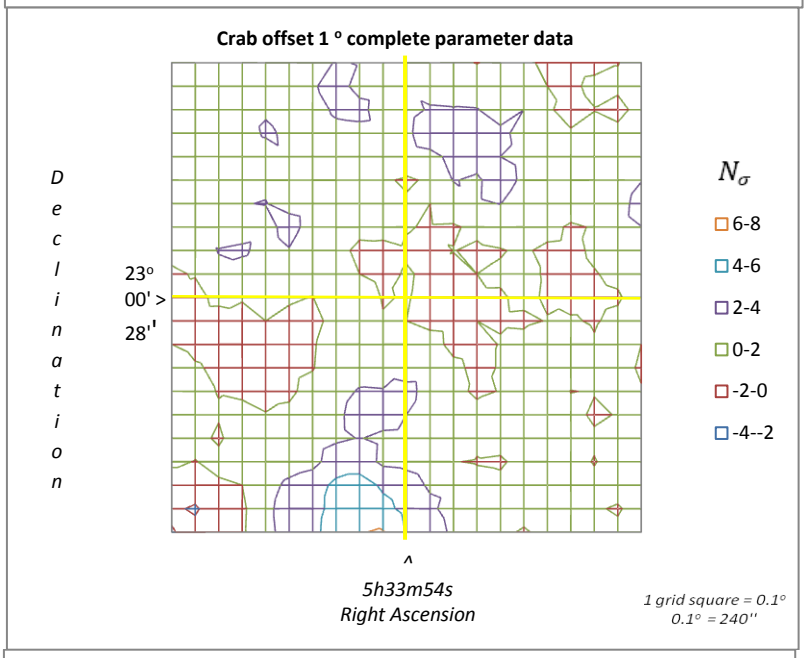

(c)

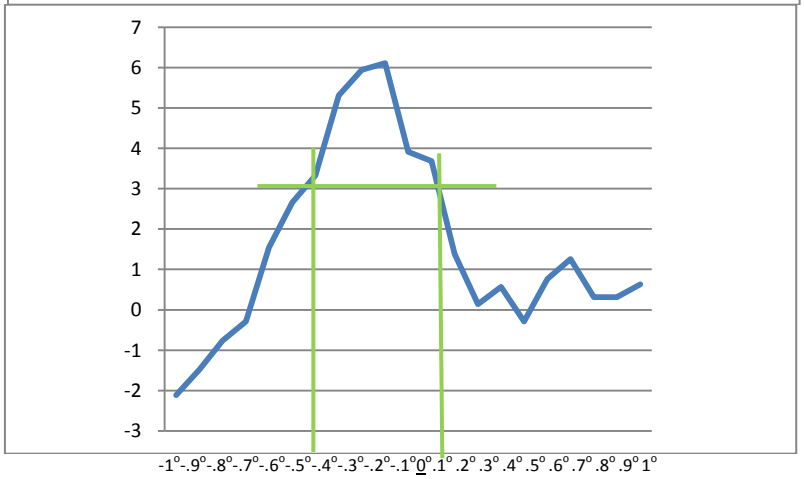

Fig 4.9: 2 dimensional analysis of the 1° offset complete Crab parameter data set.

(a)

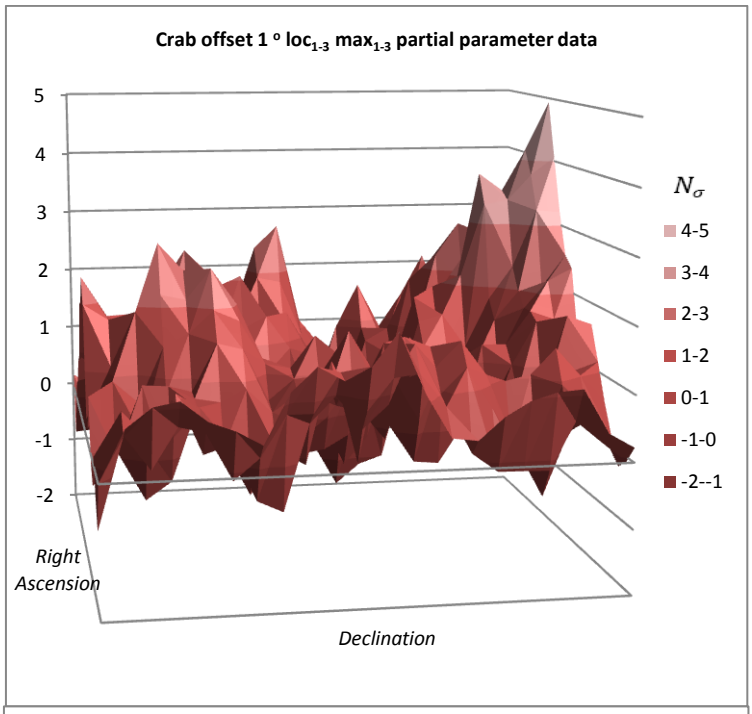

(b)

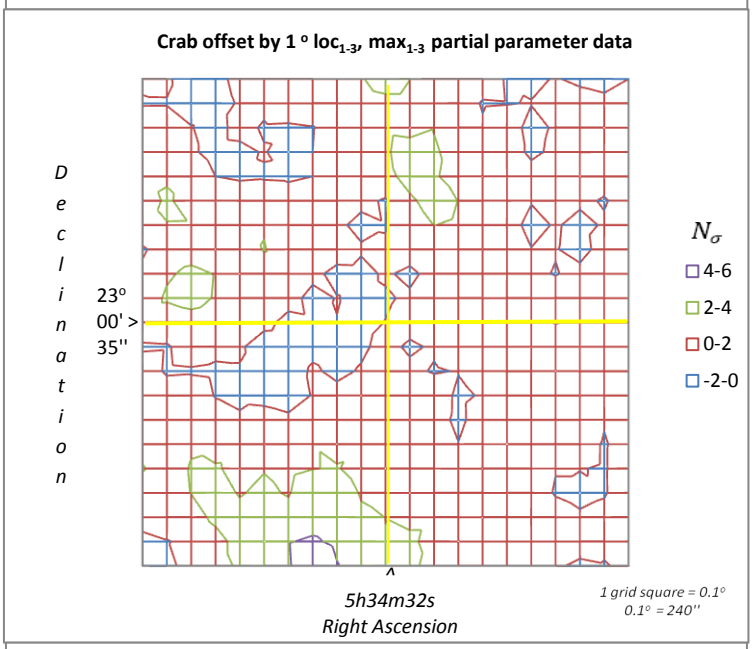

(c)

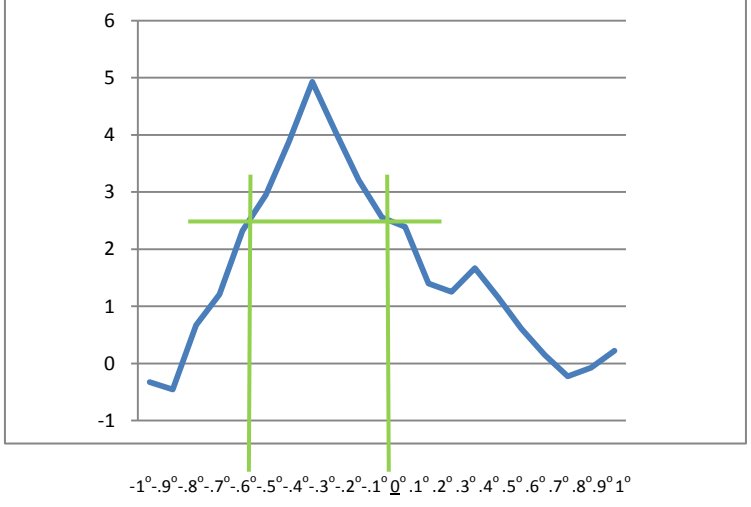

Fig 4.10: 2 dimensional analysis of the 1° offset Crab partial parameter data set.

In these validation runs we notice that the peak statistical significance from the Crab partial parameter run is more than 20% lower than that found with the complete parameter data set. Additionally the accuracy of the source position is shifted a further 0.16^{o} to the left. Even with these approximations we can clearly see the Crab Nebula in its off axis position. The contour map (b) and in particular the cross section plot (c) reveal the Point Spread Function in more detail.

4.6: Data storage

One must add a note on how data storage was managed in the calculations. As can be imagined a complicated analysis program of this magnitude has the potential to generate Gigabytes of data. One could easily lose track of what was analysed and overlook a possible successful search result, i.e. seeing a new source. We have created a 2^{o} x 2^{o} grid centred on the centre of field of view with 441 elements or 'bins' in total, from the sub division of each degree into 0.1^{o} increments. This is a 2 dimensional Cartesian coordinate grid which for mathematical simplicity was made into a one dimensional vector of 441 elements. Hence starting the 2 dimensional analysis of the first ON file on point (-1,1) we assigned vectorON(0), remembering that the centre of field of view is (0,0). Thenbin position (-0.9,1) was assigned vectorON(1) and so on until we reached (1,-1) which was assigned vectorON(440). If an event passed all supercut conditions and the orientation cut at a particular bin position the value in this vector was incremented by one, otherwise it remained the same value. When the second ON file was opened for analysis the same process followed. Events passing supercuts at a particular grid position had the value in the vector corresponding to that position incremented by one if all cuts passed, otherwise it remained the same. The same process followed suite for all the OFF files, which was assigned an identical vectorOFF(i), where i = 0 to 440. At the end of the analysis the statistical significance could easily be calculated by,

$$N_{\sigma}(i) = \frac{\text{vectorON(i)} - \text{vectorOFF(i)}}{\sqrt{\text{vectorON(i)} + \text{vectorOFF(i)}}};\ \text{i} = 1 \text{ to } 440 \qquad (4.28)$$

This calculation is near instantaneous and uses only a few kilobytes of memory. There is a danger that the vectors may become 'out of sync' which would nullify their validity hence a piece of validation code was entered into the program which is now described.

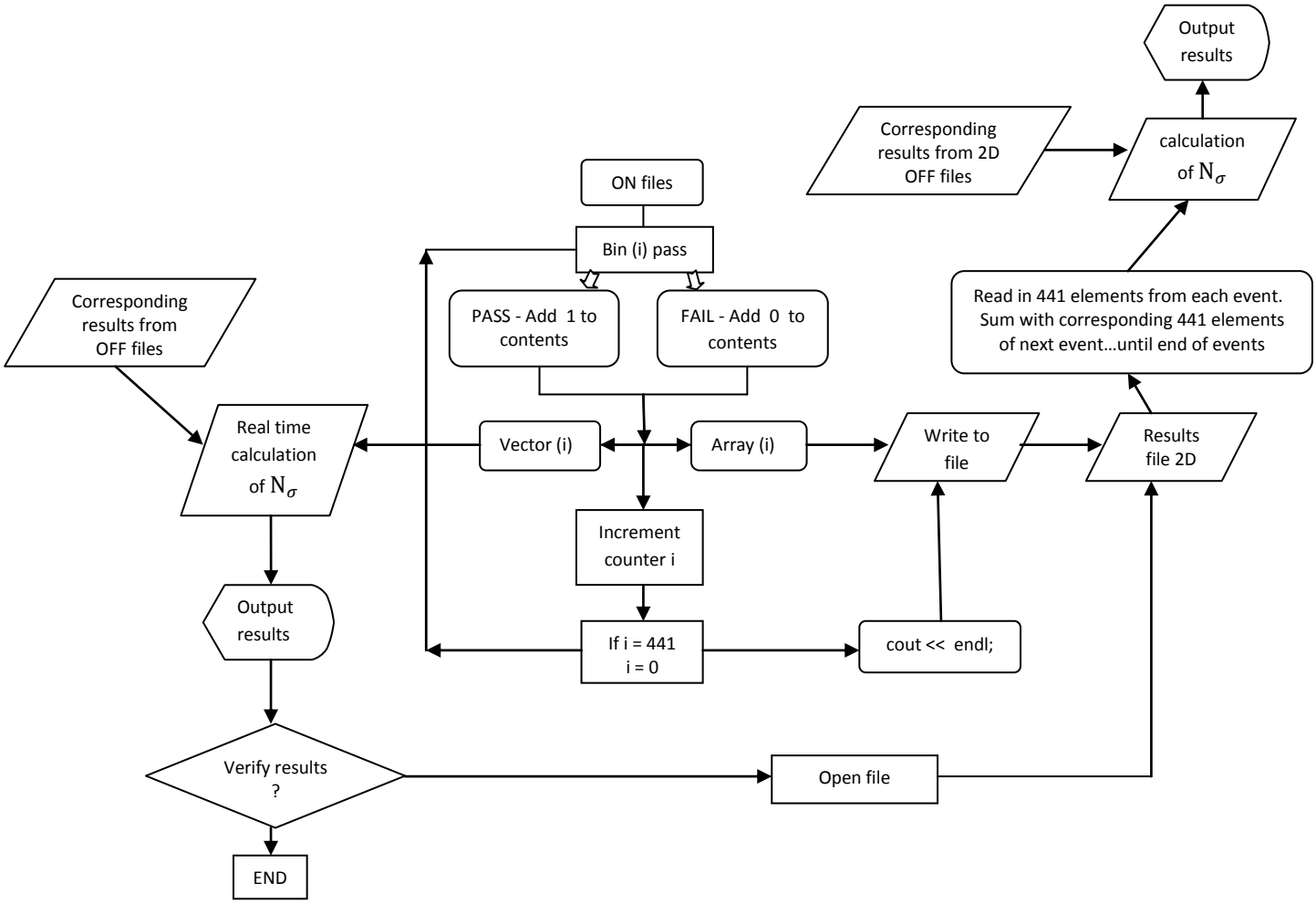

Fig 4.11: Schematic of statistical significance calculation incorporating verification. The amount of data being processed warrants this complexity to ensure accurate calculations.

Before an event has its centroid calculated and undergoes parallactic rotation, it must first pass shapecuts. This happens immediately after the pre selection criterion outlined previously in section 4.1. There is no point in taking up the computers running time with events that are caused almost exclusively by cosmic particles and various muons as our search is solely for gamma rays. Hence each event that passes the pre selection and shapecuts is worked on by the 2 dimensional analysis and all 441 bin calculation results are written to a pre-results file, all on the same line of a standard text editor. The next

event that is worked on by the analysis is also written to file, all 441 points on the next line of the text editor and so on. What the program leaves is an enormous 2 dimensional array for each of the ON and OFF files whose columns correspond to each individual bin positions. These can be added together and the statistical significance can be calculated. The OFF files for AE Aquarii have a total of 5927 shapecut passes which means we have a two dimensional array of (441x5927) elements which is greater than $2.6x10^6$ data bytes. Reading these into the program for both the ON and OFF files is time consuming but it has two major advantages. One it validates the vector calculation when needed and secondly it keeps a record of individual events which can be read into a separate program and reconstructed in a 2 dimensional grid and graphed etc.

4.6.1: Validation conclusion

The offaxis validation technique has been validated on Crab data. This allows it application to the AE Aquarii data analysis. In particular this validates that the derotation is carried out in the correct direction.

4.7: AE Aquarii data analysis

The validated program was then given the archival data of AE Aquarii to analyse. This data was taken from the 1991-1992 observing season and consisted of both ON-OFF pairs and Tracking runs. Analysis will be carried out on the ON-OFF pairs for this thesis only. 29 ON-OFF pairs were cut to length, making use of the timing markers present in all parameter files which are separated by 60 siderial seconds. Local Siderial Time (LST) values for each ON and OFF file were entered into arrays as was done for the Crab nebula data so as to be incorporated in the parallactic de rotation of each individual event. The RA and DEC of the runs were also noted; it was found that 27 of the 29 ON-OFF pairs had OFF runs centred on the same point of the sky (RA = *21hr09min45sec*) that was obviously 30min ahead of the RA of AE Aquarii. This opened the possibility of searching two independent areas of the sky for hereto unknown sources of TeV gamma rays.

As the OFF region is tracked over the same range of Azimuth and elevation as the corresponding ON region the range of the parallactic angle will be the same. We could with more complication have de rotated each event in the OFF file and then have calculated the excess, though not without a possible chance of error. We must remember that we are examining two different areas of the sky; though highly unlikely a gamma ray source present at ($+0.5^{o}$, 0^{o}) could have a corresponding but completely independent source present at ($+0.5^{o}$, 0^{o}) on the corresponding OFF file. The two hypothetical sources, were they of approximately the same intensity, would cancel each other out in the statistical significance calculation. This scenario is most unlikely but it is to be avoided for the sake of producing a definitive analysis.

The major criticism of the ON-OFF observing technique is that it spends half of its time looking at a 'blank' sky as so many physicists have said. This is an advantage to the present analysis for if sufficient OFF runs are centred at the same RA then a second area of sky may be scanned for potential sources. All that is needed is to enter an array containing the LST values for each of the 27 OFF files, using these values for both ON run and OFF run de rotation. If a gamma ray source was located in the OFF region then

the resulting statistical significance would yield a negative value, unless the formula were changed to the following,

$$N_{\sigma}(i) = \frac{\text{vectorOFF(i)} - \text{vectorON(i)}}{\sqrt{\text{vectorON(i)} + \text{vectorOFF(i)}}};\ \text{i} = 1 \text{ to } 440 \qquad (4.29)$$

As mentioned before there are two approximations in this analysis that have a significant bearing on the analysis outcome. The centroid must be calculated from the max_1, max_2 and max_3 parameters together with loc_1, loc_2 and loc_3. This is further corrected by use of the |*distance*| parameter.

Secondly and most critically the "sign" of the |*miss*| parameter needs to be ascertained. I say critically for the intercept, c_{2d}, is calculated from,

$$c_{2d} = (y' - y''_{cen}) - m_{2d}(x' - x''_{cen})$$

where *(x', y')* is the new centre of field of view and (x''_{cen}, y''_{cen}) is the image centroid. Thus the greater the distance the centroid is from the new centre of field of view under question the greater the error for a given error in calculation of slope.

4.7.1: AE Aquarii archival data

As stated with regard to the AE Aquarii OFF files, it was found that all but two of the OFF files were of RA = 21hrs 9min 45sec. All the 27 LST values from these files were entered into the program and a new ON-OFF pair list was created that would read these values in to analysis the 27 OFF files, using the corresponding ON files as the background. The RA from the OFF run is used for both files as is the LST from the OFF file used for parallactic derotation of both files, refer to (4.12). When run the program will display a negative excess for a candidate source. The ON files and the OFF files have been analysed for clockwise and anti clockwise de rotation.

The question that needs to be asked legitimately is, “if the header file says that the RA is 21hrs 9min 45sec for 27 OFF files were these 27 files actually centred on 21hrs 9min 45sec?” At this epoch in history, about 20 years since the original data was taken, it will be impossible to determine. It is assumed that the header information was recorded correctly.

As an addition to the total 29 ON-OFF pair examination and the 27 OFF-ON pair examination, a 2 dimensional analysis to each individual pair has been carried out in both analysis runs. The analysis prints a results chart identical to the master results for the summation of all files. These have not been included in this thesis as it will overwhelm the available space to deal with adequately. In brief, if an excess of $N_\sigma > 5\sigma$ was found in a single ON-OFF pair or OFF-ON pair the program would note this and display at the end of the complete run. This high statistical significance might point to a episodic gamma ray emission. No such events were recorded.

We will now examine the results obtained with the validated software analysis developed specifically for this thesis.

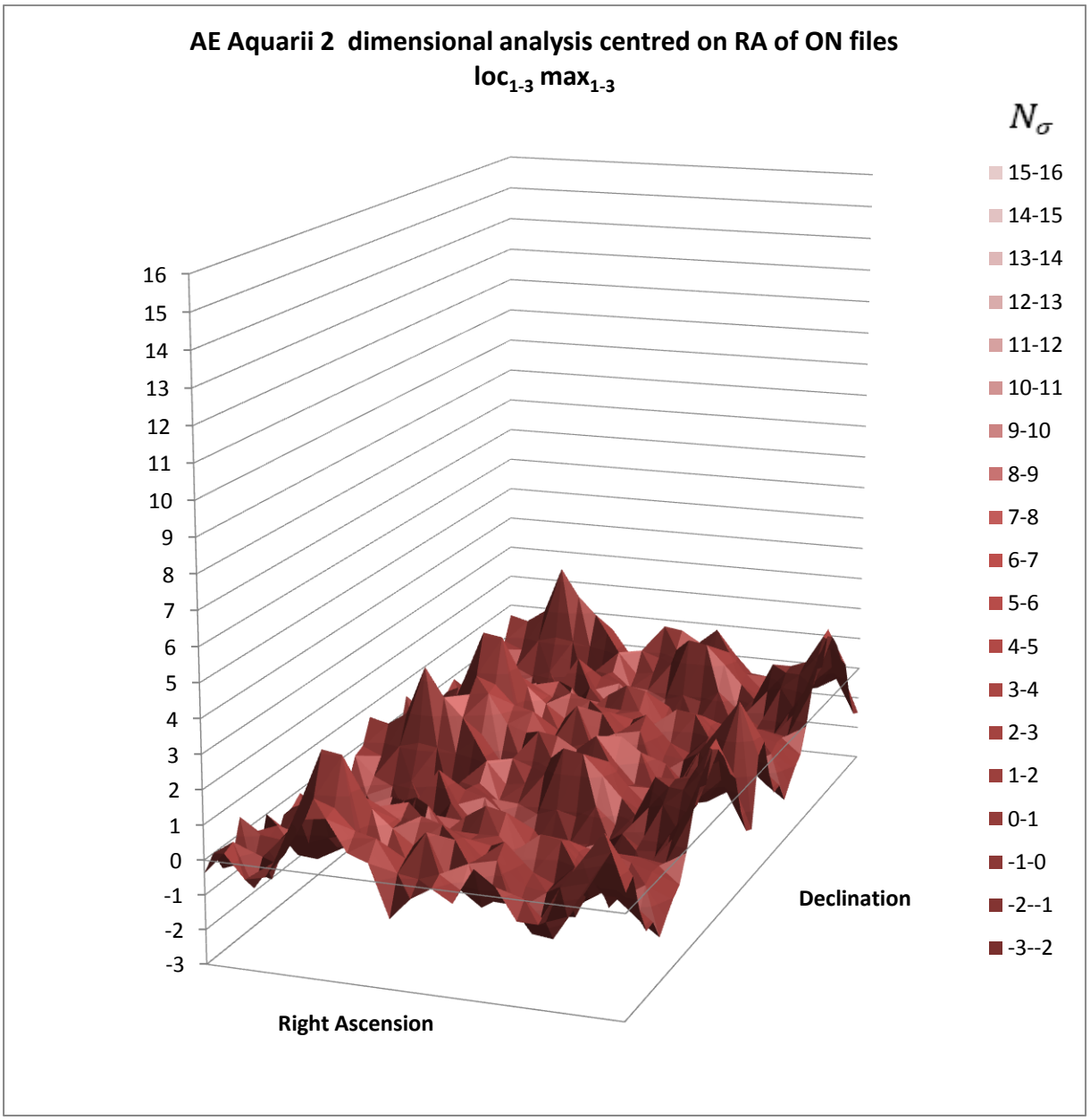

Fig 4.12: In this analysis run the LST's for each event of the 29 ON-OFF pairs were taken from the ON header files. The RA is centred on the caclysmic variable AE Aquarii. The scaling of this 3D plot has been changed to allow comparison with the Crab Nebula at centre of field of view which had 38 ON-OFF pairs, and whose results appear in Fig 4.8.

(AE Aquarii) → RA = -53° 50' 00''; DEC = 20hr39min45sec (J1990)

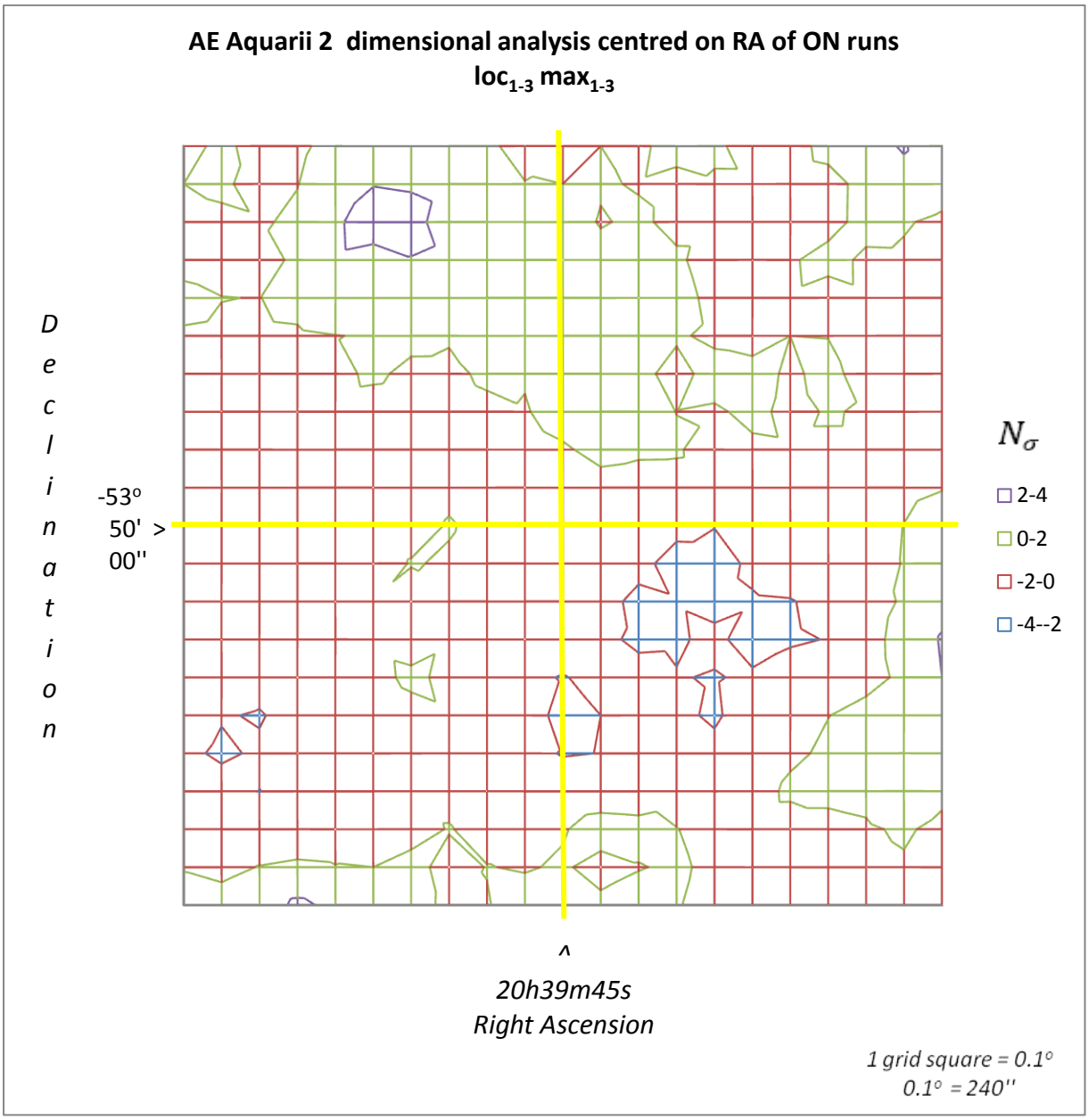

Fig 4.13: The resulting contour map from the 3 dimensional graph of Fig 4.12. It shows a minor statistical significance, N$\sigma = 3.12\sigma$ at (0.5, 0.8) with regard to the centre of field of view. This can be explained by normal fluctuations in gamma ray background. Refer to Chapter 5.

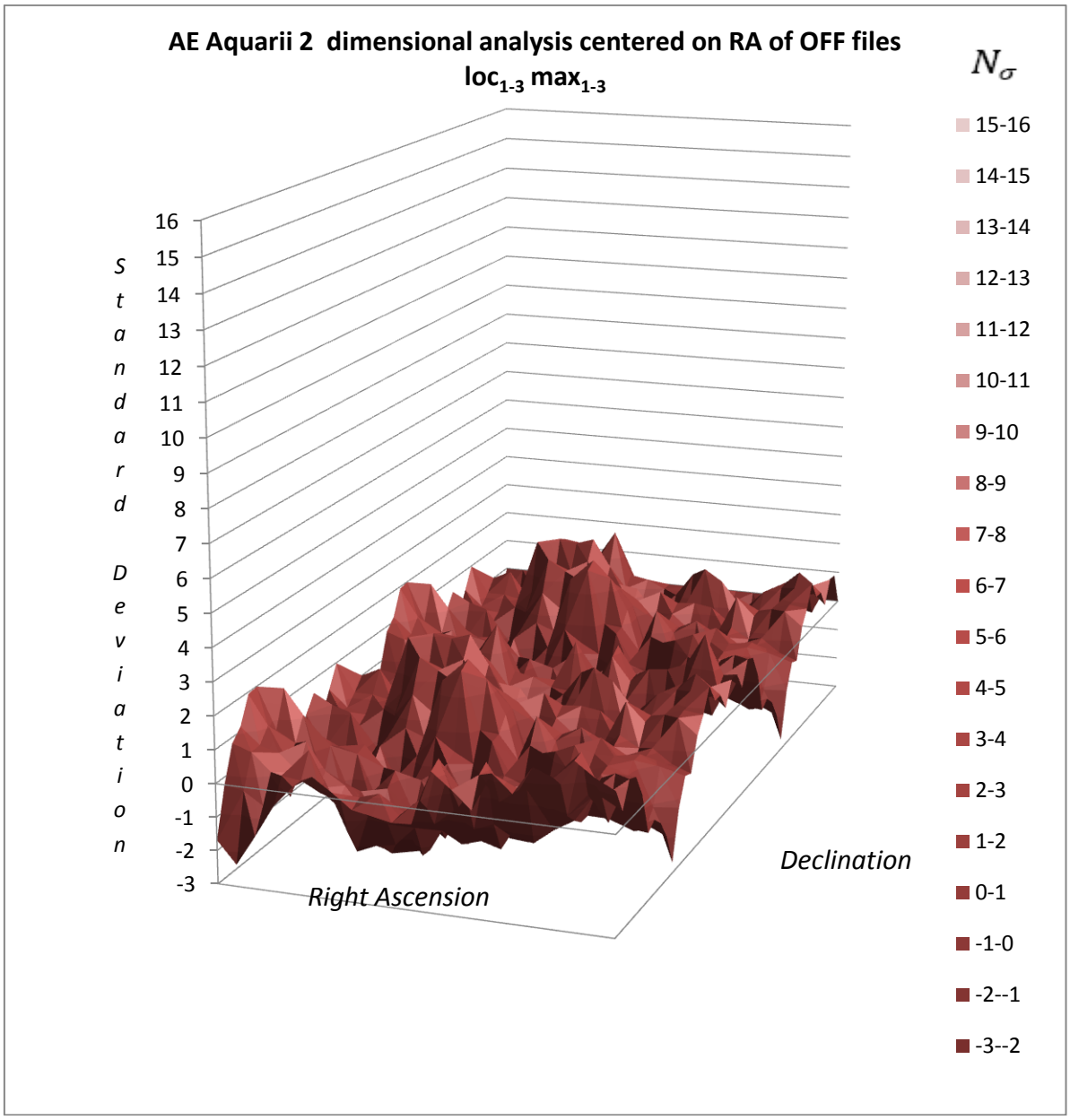

Fig 4.14: This analysis run consisted of 27 ON-OFF pairs where the LST's were taken from the OFF files and applied to both ON and OFF files for parallactic de rotation. The scaling of this 3D plot has been changed to allow comparison with the Crab Nebula at centre of field of view.

centre of field of view → RA = 21hr09min45sec; DEC = -53°50'00''

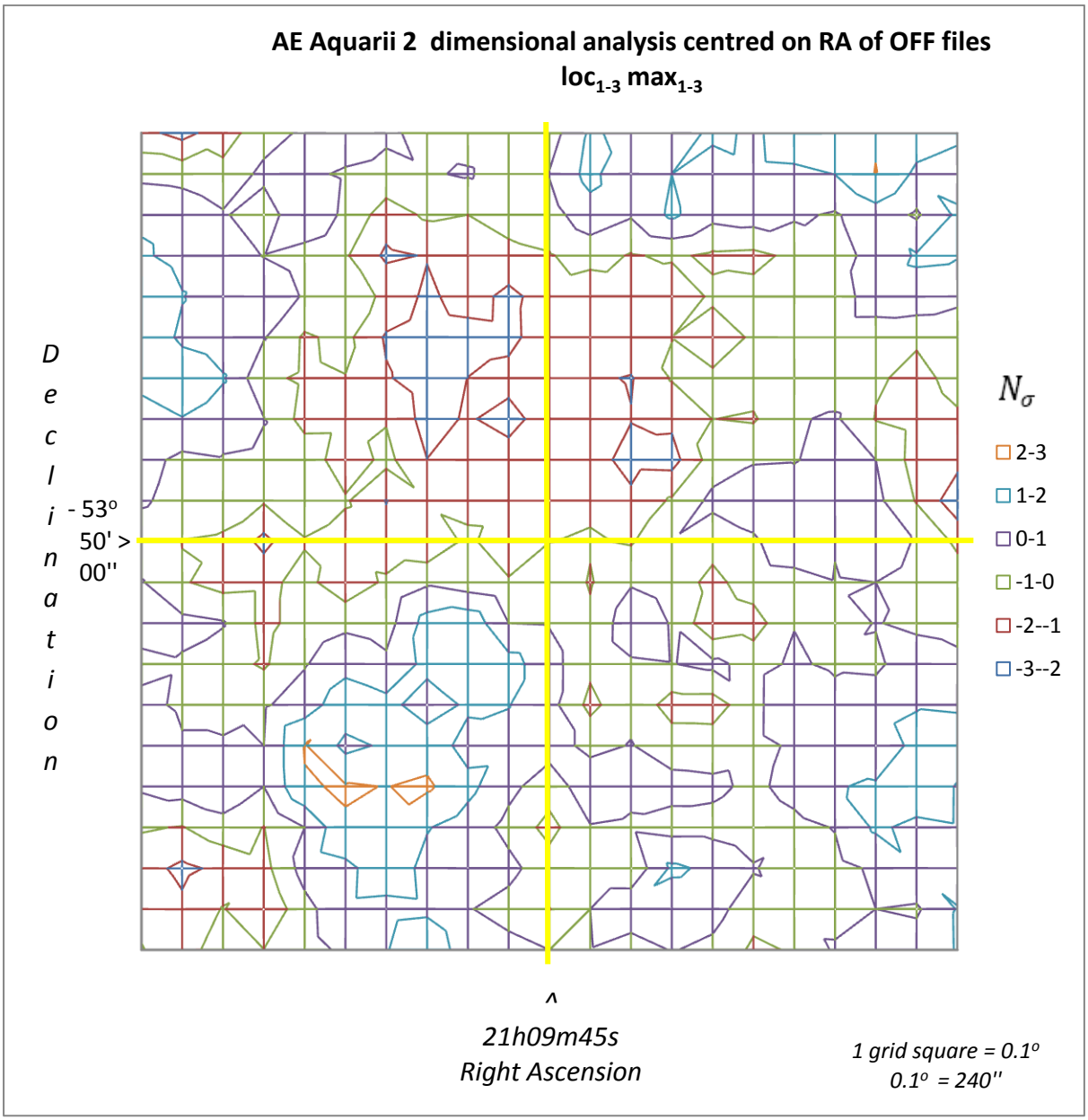

Fig 4.15: The resulting 2 dimensional representation of the 3 dimensional plot of Fig 4.14.

In this OFF run of the AE Aquarii data the formula to calculate the statistical significance has not been changed to take account of the OFF files. Hence a statistical significance detected in this OFF run would appear as negative, as

$$N_\sigma = \frac{(on\ event\ - off\ event)}{\sqrt{on\ event + off\ event}}; \qquad (4.21)$$

thus a source detected in the OFF files will yield a negative result.

Chapter 5

Conclusion

5.1: In summation

In this final chapter effort is now made to summarise the present analysis and comment on the results. As can be seen from the extensive set of graphs displayed in the previous chapter there is ample evidence to support the efficacy of this analysis' ability to identify TeV sources in the effective field of view of the Imaging Atmospheric Cherenkov Telescope. Thanks to archival data of the Crab Nebula, verification runs were carried out prior to analysis of the sky region around AE Aquarii. These specific code lines for the verification run were incorporated into the final analysis program which was able to analyse all the archival data available changing just the minimum of variables. In short with the minimum of adaptability this program will be able to analyse all parameter files from Whipple regardless of the observation epoch, provided the PMT coordinates are known.

Firstly looking at a one dimensional analysis of the Crab Nebula at the centre of field of view for parameter files derived from raw data and archival parameter files, both techniques yield a consistent statistical significance of $N_\sigma \approx 16\sigma$. This tallies well with a 2 dimensional analysis of the centre of field of view of the same source yielding a statistical significance of $N_\sigma \approx 16\sigma$. Thus at the centre of field of view the calculations were most consistent, despite the inherent approximations made in 2 dimensional analysis as mentioned in chapter 4. For the verification runs the 5 ½ hours of data from the Crab Nebula offset by 1^o showed a consistent characteristic of 2 dimensional analysis; the putative source is shifted from its true position by a small fraction of 1^o. Fig 1.1, displaying a possible TeV source, displays a maximum statistical significance away from the known true position of the emitter. This was found to be the case with the raw data analysis of the Crab off set and the parameterised analysis. Further for the verification run of the parameterised data, the resultant statistical significance was of the order of 20% below the recorded level for the raw data. All in all these discrepancies are small; when weighed with the possible gains involved in searching for new TeV sources in the night sky the 2 dimensional analysis of archival data is worth the effort.

All modern telescopes are operating in a 2 dimensional mode as standard so a small error in candidate source position will be within the field of view.

The AE Aquarii runs however did yield a statistical significance of +3.1σ and -2.5σ respectively for the ON and OFF analysis runs. It remains now to determine if this is to be expected or if it is a noteworthy result. Below we see a cross section through the 3 dimensional plot at the maximum statistical significance. If the peak were due to a point source, the curve on display would be bell shaped in nature, emerging from the natural background fluctuations.

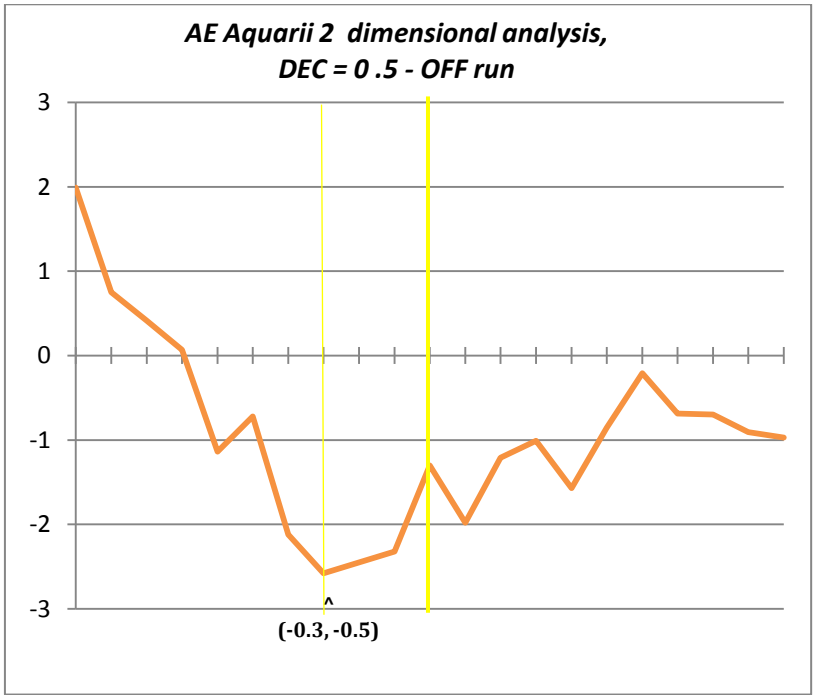

Fig 5.1: The OFF run for AE Aquarii. This plot cuts through the maximum statistical significance found, keeping Declination constant. By the rough contour compared to figures 4.13 and 4.14 and the rapid swing in Standard Deviation from (-) to (+) to the left of the centre of field of view, it would be unlikely that this point is of significance. However a calculation will be carried out to determine the probability of finding such a statistical significance.

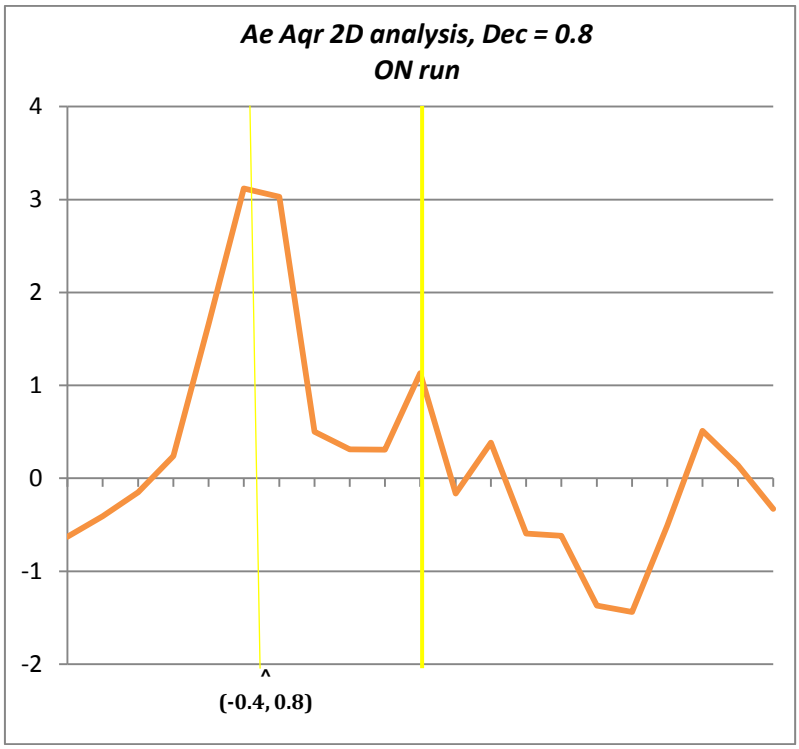

Fig 5.2: The ON run for AE Aquarii. As mentioned in Fig 5.1 above, the contours do not point to a likely PSF, though this plot of statistical significance does look more promising.

5.2: Probability of a 3σ event

There follows the calculations to determine the probability of finding a Statistical significance of 3σ in the analysis output. Firstly we will examine a known point source (the Crab Nebula) and calculate its FWHM for its PSF. refering Fig 4.11 the plot of Standard Deviation vs. Right Ascension, the parameterised files yielded a FWHM of 0.35^{o}, thus half of this is HWHM = 0.175^{o}. Now the field of view in the 2 dimensional analysis is 2^{o} x 2^{o}, so with these figures we can calculate the total number of trials in the Field of View;

$$\mathrm{N}_{\mathrm{trials}} = number\ of\ trials = \frac{area\ of\ Field\ of\ view}{FWHM\ area\ of\ point\ source\ PSF}; \qquad (5.1)$$

$$\mathrm{N}_{\mathrm{trials}} = \frac{2^{o\,2}}{\pi(0.175^{o})^{2}} \approx 42$$

The peak excess in the ON run is $N_\sigma = 3.12$, found at coordinate (-0.4, 0.8). The statistical function in EXCEL, NORMDIST, was employed to help determine the likelihood of seeing a statistical significance, N_σ, at a given point. NORMDIST is used to sum the area under the normal distribution between -∞ and x. Thus 1 - NORMDIST(x) is the probability of obtaining an excess signal of x standard deviations or greater. NORMDIST gives a value of 0.999096 for $N_\sigma = 3.12$ and (1 – NORMDIST) for $N_\sigma = 3.12$ gives a value of 0.000904, which is equivalent to 1 : 1106. To determine the probability finding an excess of $N_\sigma = 3.12$ in the 2 dimensional Field of View;

$$probability\ of\ 3.12\sigma = \frac{(1 - \mathrm{NORMDIST})}{\mathrm{Ntrials}} = 1{:}1106/_{42} = 1 : 26; \qquad (5.2)$$

Thus there is a 1 in 26 chance of finding an excess of 3.12 σ at a particular point.

We can carry out the same calculations for the OFF run which is plotted in Fig 5.2; (1 – NORMDIST) for $N_\sigma = 2.58$ gives a value of 0.00494, which is equivalent to 1 : 202. As the True Trials Factor, N_{trials}, remains the same at 42. Thus;

$$probability\ of\ 2.58\sigma = \frac{(1 - \mathrm{NORMDIST})}{\mathrm{Ntrials}} = 1{:}202/_{42} \approx 1 : 5; \qquad (5.3)$$

Thus there is a 1 in 5 chance of an excess of $N_\sigma = 2.58$ at a particular point. Recall that the OFF run will yield a negative value for a positive statistical significance, due to the programming alone. Thus the negative value is taken as an absolute value, while the positive maximum is ignored. We can say with a good deal of confidence that there is not a significant signal in either field of view.

5.3: What of the future?

The VERITAS collaboration, operating the successor to the 10m Whipple, is presently the world's most sensitive Imaging Atmospheric Cherenkov Telescope. Recent results have been given worldwide attention by publication in prominent journals. It is an excellent time to be involved in VHE gamma ray astronomy. Though this thesis did not yield a positive result in the sky region of AE Aquarii the 2 dimensional technique has been well validated and the present work is available for further analysis of archival data.

Increased sensitivity means not only that faint VHE gamma ray sources may be detected, but that less observation time is needed for stronger emitters, thereby increasing the number of sky regions that may be analysed over the course of a night. The point source sensitivity for detection of a 1% Crab signal takes less than 50hrs; for detection of a 10% Crab, 45 min suffices. It goes without saying that all observations are now 2 dimensional and data is stored directly to HDD.

There are a number of interesting objects presently under observation. Thanks to a multiwavelength collaborative effort high resolution radio and gamma ray observations have revealed the site of relativistic particle acceleration in the galaxy M87. This source was mentioned briefly in chapter2. LS I +61 303 is one of only a handful of binary star systems which are known TeV emitters. It is known to be a pairing of a massive main sequence star and a compact object of unknown nature most likely a neutron star. VERITAS detected VHE gamma ray emission from the intermediate frequency peaked BL Lacertae object W Comae (redshirt z=0.102). The source was observed between January and April 2008. Closer collaboration with other Imaging Atmospheric Cherenkov Telescopes and multiwavelength observations of objects as just mentioned are sure to provide rich discoveries of the non thermal universe in what may be a golden age in VHE gamma ray observation.

Fr Michael Connolly,
Galway, 2010.

Appendix A

TeV Gamma ray Source Catalog

Name	RA	Decl	GL	GB	Claim	Comment	No.
NGC 253	11.888	-25.2882	97.369	-87.964	C2, ~C3, ~H	Starburst Gal., z=0.00080	*
RGB J0152+017	28.16575	1.7885	152.378	-57.540	H	HBL, z=0.080	1
3C66A	35.66505	43.0355	140.143	-16.767	Cr,~HC,~W,~S, V	QSO, z=0.444	2
3C66B	35.79755	42.9921	140.254	-16.772	M	Radio galaxy, z=0.021	3
1ES 0229+200	38.2025	20.2880	152.941	-36.607	H	HBL, z=0.14	4
LSI +61 303	40.13194	61.2293	135.675	1.086	M, V	Microquasar, P_orb=26.5d. ~2kpc	5
1ES 0347-121	57.34667	-11.9908	201.927	-45.709	H	HBL, z=0.188	6
Crab	83.63288	22.01446	184.557	-5.785	W, Many	Crab nebula/pulsar (0531+21)	7
PKS 0548-322	87.6692	-32.2712	237.565	-26.147	H	HBL, z=0.069	8
MAGIC J0616+225	94.17917	22.53000	189.035	2.903	M, V	SNR IC443	9
HESS J0632+057	98.24292	5.80556	205.660	-1.441	H	in Monoceros SNR	10
S5 0716+714	110.4727	71.3434	143.981	28.018	M	Blazar, z=0.33+-0.09?	11
1ES 0806+524	122.4550	52.3162	166.245	32.910	V	HBL, z=0.138	12
PSR 0833-45	128.8359	-45.1766	263.552	-2.787	C1, ~H, ~C3	Vela pulsar	*
Vela X	128.3833	-45.7283	263.806	-3.371	H, C3	SNR, G263.9-3.3	13
RX J0852.0-4622	132.2458	-45.6333	265.385	-1.181	C2, C3, H	SNR, G266.6-1.2, Vela Jr.	14
1ES 1011+496	153.7674	49.4335	165.534	52.712	M	HBL, z=0.212	15
HESS J1023-575	155.8250	-57.7639	284.192	-0.386	H	Westerlund 2	16
1ES 1101-232	165.9065	-23.4917	273.189	33.079	H	HBL, z=0.186	17
Mkn 421	166.1138	38.20883	179.832	65.031	W, Many	HBL, z=0.031	18
Cen X-3	170.3132	-60.6233	292.09	0.336	D, ~H	X-ray binary	*
Mkn 180	174.1100	70.1576	131.910	45.641	M	HBL, z=0.045	19
1ES 1218+304	185.3414	30.1770	186.359	82.734	M	HBL, z=0.182	20
W Com	185.3820	28.2329	201.735	83.288	V	IBL, z=0.102	21
M87	187.7059	12.39112	283.778	74.491	HC, H, V	Radio galaxy, z=0.00436	22
3C279	194.0465	-5.7893	305.104	57.062	M	FSRQ, z=0.536	23
PSR 1259-63/SS2883	195.6987	-63.8357	304.184	-0.992	~C2, H	PSR/Be binary	24
HESS J1303-631	195.7642	-63.1986	304.241	-0.356	H	UnID, Cen OB1? PSR J1301-6305 PWN?	25
HESS J1356-645	209.0	-64.5	309.81	-2.49	H	PSR J1357-6429 PWN?	26
HESS J1418-609	214.5167	-60.9753	313.247	0.150	H	Kookabura NE wing?	27
HESS J1420-607	215.0375	-60.7600	313.558	0.268	H	Kookabura SW wing? Rabbit? PSR J1420-6048 PWN?	28

HESS J1427-608	216.97	-60.85	314.409	-0.146	H		29
H 1426+428	217.1354	42.67361	77.49	64.899	W, H, Ca	HBL, z=0.129	30
RCW 86	220.7667	-62.4617	315.440	-2.332	C2, H	SNR, G315.4-2.3 / MSH14-63	31
SN1006	225.5919	-41.8962	327.514	14.642	C1, ~H, H	SNR, G327.6+14.6	32
HESS J1503-582	226.04	-58.18	319.7	0.3	H	Forbidden-Velocity-Wing?	33
MSH 15-52	228.5292	-59.1575	320.330	-1.192	C1, H, C3	SNR, G320.4-1.2, HESS J1514-591	34
PG 1553+113	238.9294	11.1901	21.909	43.964	H, M	HBL, z>0.25?	35
HESS J1614-518	243.5679	-51.8442	331.497	-0.594	H		36
HESS J1616-508	244.1033	-50.8964	332.394	-0.140	H	PSR J1617-5055 PWN?	37
HESS J1626-490	246.52	-49.087	334.772	0.0457	H		38
HESS J1632-478	248.04	-47.82	336.38	0.212	H	PSR J1632-4818?	39
HESS J1634-472	248.74	-47.27	337.11	0.339	H		40
HESS J1640-465	250.1829	-46.5319	338.317	-0.021	H	G338.3-0.0?	41
Mkn 501	253.4672	39.76004	63.6	38.859	W, Many	HBL, z=0.034	42
HESS J1702-420	255.684	-42.016	344.304	-0.184	H	G344.7-0.1? PSR J1702-4128?	43
HESS J1708-410	257.101	-41.090	345.683	-0.469	H		44
PSR 1706-44	257.426	-44.4825	343.1	-2.683	C1, D, ~H	3EGJ1710-4439	*
RX J1713.7-3946	258.425	-39.7667	347.346	-0.498	C1, C2, H	SNR, G347.3-0.5	45
HESS J1713-381	258.475	-38.199	348.639	0.388	H	CTB 37B? 3EG1714-3857?	46
HESS J1714-385	258.5792	-38.5667	348.389	0.107	H	CTB 37A? 3EG1714-3857?	47
HESS J1718-385	259.5292	-38.5500	348.833	-0.488	H	PSR J1718-3825 PWN ?	48
HESS J1731-347	262.98	-34.71	353.565	-0.623	H	G353.6-0.7?	49
HESS J1745-303	266.26	-30.37	358.71	-0.64	H	3EG J1744-3011	50
Sgr A*	266.4169	-29.0078	359.944	-0.046	C2, W, H, M	Gal.C.[Rogers et al.1994 ApJ434L59]	51
Galactic Center ridge	266.4169	-29.0078	359.944	-0.046	H	-0.8< l <0.8deg, |b|<0.3deg	52
G0.9+0.1	266.8467	-28.1517	0.872	0.076	H	PWN (but no PSR found)	53
HESS J1800-240	270.156	-23.996	5.960	-0.380	H	(A,B,C), south of SNR W28/G6.4-0.1	54
HESS J1801-233	270.426	-23.335	6.657	-0.268	H	SNR W28/G6.4-0.1	55
HESS J1804-216	271.1329	-21.6919	8.408	-0.027	H, C3	G8.7-0.1 / W30? PSR J1803-2137 PWN?	56
HESS J1809-193	272.6292	-19.3000	11.180	-0.087	H	G11.0+0.0 / PSR J1809-1917 PWN?	57
HESS J1813-178	273.4079	-17.8428	12.813	-0.034	H, M	SNR AX J1813-178/G12.82-0.02	58
HESS J1825-137	276.5150	-13.7633	17.820	-0.743	H	G18.0-0.7 ? PSR J1823-13 PWN?	59
LS 5039	276.5626	-14.8482	16.882	-1.289	H	XRB, HESS J1826-148	60
HESS J1833-105	278.3854	-10.5553	21.511	-0.875	H	G21.5-0.9? PSR J1833-1036?	61

HESS J1834-087	278.7104	-8.7533	23.258	-0.329	H, M	G23.3-0.3 / W41 ?	62
HESS J1837-069	279.4279	-6.9275	25.206	-0.121	H	G25.5+0.0? A1838.0-0655/PSR J1838-0655?	63
HESS J1841-055	280.229	-5.550	26.795	-0.197	H		64
HESS J1843-033	280.75	-3.3	29.0	0.37	H		65
HESS J1846-029	281.6004	-2.981	29.705	-0.240	H	Kes75? PSR J1846-0258?	66
HESS J1857+026	284.297	2.680	35.972	-0.056	H		67
HESS J1858+020	284.585	2.090	35.579	-0.582	H		68
MGRO J1908+06	287.0183	6.3192	40.45	-0.80	MG, H, V	HESS J1908+063	69
HESS J1912+101	288.23	10.15	44.4	-0.1	H	PSR J1913+1011? GRS 1915+105?	70
Cyg X-1	299.5903	35.2016	71.335	3.067	M	Black hole candidate, variable	71
1ES 1959+650	299.9994	65.14852	98.003	17.67	U, W, HC, M	HBL, z=0.048	72
PKS 2005-489	302.3721	-48.8219	350.386	-32.611	H	HBL, z=0.071	73
MGRO J2019+37	305.0238	36.7191	75.0	0.2	MG	Extended: 1.1deg	74
TeV J2032+4130	308.0292	41.50833	80.254	1.074	HC, W, MG, M	UnID: Cyg OB2? / MGO J2031+41	75
PKS 2155-304	329.7169	-30.2256	17.73	-52.246	D, H, C3, M	HBL, z=0.117	76
Cas A	350.8529	58.8154	111.736	-2.13	HC, M, V	SNR, G111.7-2.1	77
BL Lac	330.6807	42.27779	92.59	-10.441	~W, ~HC, Cr, M	LBL, z=0.0686	78
1ES 2344+514	356.7702	51.70497	112.891	-9.908	W, HC, M	HBL, z=0.044	79
H 2356-309	359.7825	-30.6272	12.843	-78.035	H	HBL, z=0.165	80

Appendix B

Parameterization Formulae

B.1 Moments of the Light Distribution

$$S_{tot} \equiv SIZE = \sum_i S_i$$

$$< x > = \frac{1}{S_{tot}} \sum_i S_i x_i$$

$$< y > = \frac{1}{S_{tot}} \sum_i S_i y_i$$

$$< x^2 > = \frac{1}{S_{tot}} \sum_i S_i x_i^2$$

$$< y^2 > = \frac{1}{S_{tot}} \sum_i S_i y_i^2$$

$$< xy > = \frac{1}{S_{tot}} \sum_i S_i x_i y_i$$

The sums are made over pixels which pass the cleaning threshold only. These moments are calculated about the origin of the camera.

For an offset origin position (o_x, o_y), one can replace $x_i \rightarrow (x_i - o_x)$ and $y_i \rightarrow (y_i - o_y)$.

Useful Quantities

$$\sigma_x^2 \equiv < x^2 > - < x >^2$$

$$\sigma_y^2 \equiv < y^2 > - < y >^2$$

$$\sigma_{xy}^2 \equiv < xy > - < x >< y >$$

$$d \equiv \sigma_y^2 - \sigma_x^2$$

$$z \equiv \sqrt{d^2 + 4(\sigma_{xy}^2)^2}$$

Geometric Parameters

$$LENGTH = \sqrt{\left(\sigma_x^2 + \sigma_y^2 + z\right)/2}$$

$$WIDTH = \sqrt{\left(\sigma_x^2 + \sigma_y^2 - z\right)/2}$$

$$DISTANCE = \sqrt{< x >^2 + < y >^2}$$

$$MISS =$$

$$\left[\left(1 + {}^{d}/_{z}\right) < x >^{2} + \left(1 - {}^{d}/_{z}\right) < y >^{2}\right] / 2 - \left[2 < x >< y > \sigma_{xy}^{2} / z\right]$$

$$ALPHA = \sin^{-1}\left(\frac{MISS}{DISTANCE}\right)$$

BIBLIOGRAPHY

Abdo et al., Fermi *Observations of High-Energy Gamma-Ray Emission from GRB 080916C*; Science, Vol. 323, no. 5922, pp. 1688 (2009)

Abdo et al., *Fermi observations of TeV-selected active galactic nuclei*; Ap. J., 707 1310-1333 (2009)

V.A. Acciari et al., *Observations of extended VHE emission from the SNR IC 443 with VERITAS* (2009)

V.A. Acciari et al., *VERITAS Observations of a Very High Energy Gamma-ray Flare from the Blazar 3C 66A* (2009)

V.A.Acciari et al., *Observation of gamma-ray emission from the galaxy M87 above 250 GeV with VERITAS* (2008)

V.A.Acciari et al., *A connection between star formation activity and cosmic rays in the starburst galaxy M82*; Nature 462, 770-772 (2009)

F. A. Aharonian & C. W. Akerlof, Ann. Rev. Nucl. Part. Sci. 47, p273 (1997)

F.A. Aharonian, *The Very-High-Energy Gamma-Ray Sky*, Science Vol. 315, no. 5808, pp 70 – 72 (2007)

F.A. Aharonian et al., *Spectrum and variability of the Galactic Center VHE gamma-ray source HESS J1745-290*; Astron. Astrophys. 503, 817-825 (2009)

G.E. Allen et al., Ap. J., 487, L97-100 (1997)

H.R. Allen, Proc. 15th ICRC, vol.10, p414 (1977)

H. Anderhub et al., *Search for Very High-Energy Gamma-Ray Emission from Pulsar-PWN Systems with the MAGIC Telescope,* Ap. J., 710, 828 (2010)

H. Anderhub et al., *Correlated X-ray and Very High Energy emission in the gamma-ray binary LS I +61 303,* Astrophys. J. 706, L27 (2009)

E. Aliu et al., *Observation of pulsed gamma rays above 25 GeV from the Crab Pulsar with MAGIC*, Science,Vol. 322. no. 5905, pp. 1221-1224 (2008)

P.M.S. Blackett, Phys. Soc. Gassiot Committee Rep., 34 (1948)

P.M.S. Blackett, Phys. Abst. 52, 4347 (1949)

J. H. Buckley et al., Ap. J., 472, L9 (1996)

J.H. Buckley et al., A. &A. , 329, 639 (1998)

M. Catanese et al., in *Towards a Major Atmospheric Detector-IV*, ed. M. Cresti, 335 (1996)

M. Catanese et al., Ap. J., 487, L143 (1997)

M. Catanese, et al., Ap. J., 501, 616 (1998)

M.F. Cawley et al., Exp. Astron., 1, 173 (1990)

M.F. Cawley et al., *Detection of TeV Gamma Rays from the Crab Nebula using the Atmospheric Cherenkov Imaging Technique*, IAJ, 19(2), 51(1989).

K.S. Cheng, C. Ho & M. Ruderman, *Energetic Radiation From Rapidly Spinning Pulsars. I: Outermagnetosphere Gaps*, Ap. J., 300, pp500-521 (1986)

J.M. Davies & E.S. Cotton, Solar Energy Sci. and Eng, 1:16 (1957)

S. Dunlea et al., in ICRC vol7, p 2939 (2000)

G.G. Fazio et al., Ap. J. lett., 175, L117 (1972)

D.J. Fegan et al., Nucl. Inst and meth., 211, 179 (1983)

D. Fegan, J. Phys. G: Nucl. Part. Phys., 23, 1013 (1997)

J.P. Finley et al., Proc. 27th ICRC, Hamburg, Germany, vol.7, p2827 (2001)

G. D. Hallewell, *The status of Čerenkov detectors in astroparticle physics*, Centre de Physique des Particules de Marseille (CNRS/IN2P3), Université de la Méditeranée, France.

J.A. Gaidos et al., Nature, 383, 319 (1996)

T.K. Gaisser, *Cosmic Rays and Particle Physics*, Cambridge University Press (1990)

R. Hanbury-Brown, *The principles of the intensity interferometer; general description*. Philips Tech. Rev., vol. 27, pp 141-152 (1966)

A.K. Harding, Ap. J., 476, 246 (1997)

D.A. Hill & N.A. Porter, Nature 191, p 690 (1961)

A.M. Hillas, Proc. 19th ICRC, Vol 3, p445, La jolla (1985)

A. M. Hillas, Space Sci. Rev., 75, 17 (1996)

A.M. Hillas, Nucl. Phys. B (Proc. Suppl.) 52B, 29 (1997)

A.M. Hillas et al., Ap. J., 503, 744 (1998)

W. Hofmann, AIP Conf. Proc., *GeV-TeV Gamma-Ray Astrophysics Workshop: Towards a Major Atmospheric Cherenkov Detector*, vol. 515, p. 510 (2000)

W. Hofmann et al., *HESS - Construction and first light*, Proc. 27th ICRC, Hamburg, (2001)

K. Holliday, *Introductory Astronomy*, John Wiley & Sons Inc (1999)

J.D. Jackson, *Classical Electrodynamics*, publ. New York, Wiley (1975)

J.V. Jelley & W. Galbraith, Nature, 171, 349 (1953)

J.V. Jelley, *Cerenkov Radiation and its Applications*, ch. 9, Pergamon Press, Inc. (1958)

W.J. Kaufmann, *Universe,* 4th edition, Freeman press, p. 428 (1996)

A.D. Kerrick, et al., Ap. J., 452, 588 (1995)

A.D. Kerrick et al., Ap. J., 438, L59 (1995b)

D. Kieda et al., *A VERITAS Search for VHE Gamma-Ray Point Sources Near Selected MILAGRO Target Regions*, Proc. 30th ICRC, Merida (2007)

A. Konopelko et al., Ap. J., 658, p1062 (2007)

K. Koyama et al., Nature 378, pp255-258 (1995)

F. Krennrich et al., Ap. J., 481, p758 (1997)

M. J. Lang et al., *Effect of the Geomagnetic Field on TeV Gamma Ray Detection*, Proc. 23rd ICRC, Calgary, Canada, vol.1, p275 (1993)

M. Lang et al., A. & A., 423, 415L (2004)

R.W. Lessard, Ph.D thesis, National University of Ireland (1997)

R.W. Lessard, Proc. 19th Texas Symposium, Paris 1998 (1999)

R.W. Lessard et al., Ap. J., 15, 1 (2001)

D.A. Lewis, Nuc. Phy. B Suppl., 14A, 299 (1990)

Y.C. Lin et al., Ap. J., 401, L61 (1992)

M.S. Longair, *High Energy Astrophysics*, vol.1. Cambridge University Press, New York, 2nd ed. (1992)

M.S. Longair, *High Energy Astrophysics*, Cambridge University Press, Vol.1, 3rd ed. (2004)

D.J. Macomb et al., Ap. J., 449, L99 (1995)

G. Maier et al., *VERITAS: Status and Latest Results, Proc. 30th ICRC, Merida (2007)*

M. Martinez, Proc. 9th Int. Conf., *Topics in Astroparticle and Underground Physics*, TAUP (2005)

M. Merck et al., Proc. of SPIE Vol. 4858, 327 (2003)

J.E. McEnery et al., Proc. 25th ICRC, 3, 267, Durban OG 4.3.4 (1997)

G. Mohanty et al., Astro-Ph., 9, 15 (1988)

P. Moriarty et al., Astro-Ph., 7, 315 (1997)

P. Morrison, il Nuovo Cimento, 7, 858 (1958)

R.A. Ong, Phys. Rep., 305, 93 (1998)

R.A. Ong et al., *Recent Results from VERITAS*, Proc. 31st ICRC, Lodz (2009)

J. Patterson, *Rapid oscillations in cataclysmic variables. III. An oblique rotator in AE Aquarii*, Ap. J., 234, pp. 1–992 (1979)

M. Punch et al., Proc. 22nd ICRC, 1, 464, Dublin (1991)

M. Punch et al., Nature, 358, 477 (1992)

J. Quinn et al., Ap. J., 456, L83 (1996)

J. Quinn, PhD Thesis (unpublished), University College Dublin (1997)

P.T. Reynolds et al., Ap. J., 404, 206 (1993)

G. Rieke & T. Weekes, *Production of Cosmic Gamma Rays by Compton Scattering in Discrete Sources*, Ap. J., 155, 429 (1969)

E.L. Robinson et al., Ap. J., 374, 298 (1991)

M.S. Schubnell et al., Ap. J., 460, 644 (1996)

P. Sommers & J.W. Elbert, Phys. G: Nucl. Phys. 13, p553 (1987)

P.A. Sturrock, Ap. J., 164, 529 (1971)

S. Swordy, The energy spectra and anisotropies of cosmic rays, Space Science Reviews 99, pp85–94 (2001)

O. Tibolla et al., New unidentified H.E.S.S. Galactic sources; Proc. 31st International Cosmic Ray Conference, Lodz, (2009)

R. Wagner et al., J. Phys.: Conf. Ser. Vol. 203, p12121 (2010)

T.C. Weekes et al., Ap. J., 174, 165 (1972)

T.C. Weekes, Nuovo Cimento B 35, p95 (1976)

T.C. Weekes et al., *Observation of TeV gamma rays from the Crab nebula using the atmospheric Cerenkov imaging technique*. Ap. J., 342, pp379–395 (1989)

T.C. Weekes, et al., Proc. 3rd Compton Symp., Munich (1995)

T. C. Weekes, et al., *VERITAS: The Very Energetic Radiation Imaging Telescope Array System*, Astro-Ph., 17(2), pp221-243 (2002)

T.C. Weekes et al., *Proc. "Cherenkov2005",Palaiseau*, 3 *(April, 2005)*,(2006)

W.F. Welsh et al., Ap. J., 410, L39 (1993)